

# UC Riverside

## UC Riverside Electronic Theses and Dissertations

### Title

Studies of Atmospheric Chemistry and Reaction Mechanisms Using Optical Spectroscopy and Mass Spectrometry

### Permalink

<https://escholarship.org/uc/item/9914p817>

### Author

Liu, Yingdi

### Publication Date

2011

Peer reviewed|Thesis/dissertation

UNIVERSITY OF CALIFORNIA  
RIVERSIDE

Studies of Atmospheric Chemistry and Reaction Mechanisms  
Using Optical Spectroscopy and Mass Spectrometry

A Dissertation submitted in partial satisfaction  
of the requirements for the degree of

Doctor of Philosophy

in

Chemistry

by

Yingdi Liu

August 2011

Dissertation Committee:  
Dr. Jingsong Zhang, Chairperson  
Dr. Leonard Mueller  
Dr. Gregory Beran

Copyright by  
Yingdi Liu  
2011

The Dissertation of Yingdi Liu is approved:

---

---

---

Committee Chairperson

University of California, Riverside

## ACKNOWLEDGEMENTS

The Text of this thesis, in part or in full, is a reprint of the material as it appears in:

Environmental Science and Technology

Reproduced in part with permission from:

Environmental Science and Technology

Copyright 2011 American Chemical Society

This thesis could be done successfully due to many people who helped me. First, I am deeply and sincerely grateful to my advisor, Dr. Jingsong Zhang, for his insightful guidance, continuous support, inspiring discussion, constant encouragement and kind understanding throughout my academic program. He is a very considerate person who really thinks from my side. In the past 5 year, he is not only a good advisor but also a great mentor and a real friend. I have learned a lot from him. He is passionate about teaching me and improving my skills in academic life. He is never tired of helping me on all kinds of problems even though some of them are very tiresome. He always encourages me to think on my own and give me a lot of priceless advices about my ideas. He supports some of my ideas if they are reasonable, meanwhile he leads me to figure out why other ideas don't work. He is so knowledgeable and smart that I can

learn a lot by talking with him. He has helped me a lot not only on my research work but also my academic life. I feel so lucky to have him as my academic father.

In addition, I am grateful to Dr Akua Asa-Awuku, Dr. Paul Ziemann, Dr. Roger Atkinson, Dr. William Cater, and particularly my co-advisor Dr. David Cocker for their priceless advices for my research work. It is lucky for me to have these many great scientists to help me when I meet any kinds of difficulties during my research work. I also appreciate my committee members and all the professors in both Chemistry and Chemical Engineering departments who taught me. I have learned the real science at UC Riverside, which builds up my solid background of science.

Thirdly, I would like to thank to all of my labmates and group members, including James Hargrove, David Medina, Yu Song, Jessy Lexmuix, Xiaochen Tang, Ping Tang, Shunsuke Nakao and Gookyoung Heo. This work would not have been possible without the contributions of my fellow researchers and funding agencies, and I gratefully acknowledge their contributions.

Finally, I cannot thank enough for my parents, Qiang Liu and Jixian Liu, for their patience and support as I pursue my degrees and my dream, and for the fact they gave me their love and my life.

## ABSTRACT OF DISSERTATION

### Studies of Atmospheric Chemistry and Reaction Mechanisms Using Optical Spectroscopy and Mass Spectrometry

by

Liu Yingdi

Doctor of Philosophy, Graduate Program in Chemistry  
University of California, Riverside, August 2011  
Dr. Jingsong Zhang, Chairperson

This thesis mainly focuses on (1) development and applications of cavity ringdown spectroscopy (CRDS) to study atmospheric trace gases; (2) reactive intermediates in the alkene ozonolysis reactions using photoionization time-of-flight mass spectrometry (TOFMS); and (3) development of new methods using CRDS for thin film studies.

Specifically, CRDS based instruments are developed to measure and characterize peroxy radicals in atmosphere. By combining the chemical amplification detection of peroxy radicals (PERCA) with CRDS, the peroxy radical detection sensitivity can achieve  $\sim 10$  pptv/60s with a single channel CRDS instrument and  $\sim 1.2$  pptv/10s with a dual channel CRDS instrument. Ambient measurements of the peroxy radicals were carried out. The same dual channel instrument is also used for measurements of optical

extinction of atmospheric aerosols, which is in good agreement with the Mie theory with a sensitivity of  $0.24 \text{ Mm}^{-1}(1\sigma)$ .

To detect the early transient reactive intermediates and investigate the mechanisms of initial steps of ozonolysis of alkenes, the gas-phase ozonolysis reactions are carried out in a fast flow reactor under the conditions of low pressure (7-10 Torr) and room temperature. The alkenes investigated include *cis*-2-butene, tetramethylethylene, cyclohexene, isoprene and  $\alpha$ - and  $\beta$ -pinenes. CO is used as an OH scavenger to minimize the reactions between the OH byproduct and alkenes. After a short reaction time of  $\sim 25$  to  $\sim 200 \mu\text{s}$ , the initial products, both free radical intermediates and stable species, are detected by the 118-nm vacuum ultraviolet (VUV) photoionization TOFMS. Mass peaks corresponding to the Criegee intermediates or their isomers are identified.

This thesis also presents a novel method for determining the thickness of a non-absorbing nanoscale thin film on a nearly transparent substrate through the analysis of the transmittance signal measured using CRDS near the Brewster angle. An optical model is developed and demonstrated for a organic polymer thin film.

This dissertation is a part of my research work. For environmental chamber study of atmospheric chemistry and secondary organic aerosol formation using cavity enhanced absorption spectroscopy please refer to my MS degree thesis in Chemistry and Environmental Engineering department, UC-Riverside.



# Table of content

ACKNOWLEDGEMENTS .....	iv
ABSTRACT OF THESIS .....	vi
Chapter 1 Introduction .....	1
Chapter 2 Experimental techniques .....	9
2.1 Cavity ring-down spectroscopy .....	10
2.1.1 Introduction .....	10
2.1.2 Principle .....	11
2.1.3 Sensitivity .....	14
2.1.4 Features and Applications .....	15
2.2 Faster flow reactor combined with time-of-flight mass spectrometer .....	16
2.2.1 Faster flow reactor .....	17
2.2.2 Molecular Beam Theory[7].....	19
2.2.3 VUV PI TOFMS .....	23
Chapter 3 Measurements of Peroxy Radicals Using Chemical Amplification – Cavity Ringdown Spectroscopy .....	27
3.1 Introduction.....	28
3.2 Experimental .....	33
3.2.1 Chemical reaction system and ambient measurements.....	33

3.2.2 Calibration reaction system.....	38
3.2.3 CRDS instrument setup.....	45
3.3 Results and discussion.....	47
3.3.1 Ambient measurements.....	47
3.3.2 Ozone background .....	50
3.3.3 Ambient measurements of ROx in Riverside, CA.....	51
Chapter 4 An improved dual channel Peroxy radicals Chemical Amplification measurement using diode laser based cavity ring down spectroscopy .....	58
4.1. Introduction.....	59
4.2 Experimental .....	63
4.2.1 NO <sub>2</sub> detection using CRDS.....	63
4.2.2. Determination of NO <sub>2</sub> cross sections and instrument sensitivity.....	66
4.2.3 Chemical reaction system and ambient measurement setup .....	70
4.2.3 Calibration reaction system.....	73
4.3. Results and discussion .....	77
4.3.1. Instrumental characterization.....	77
4.3.2 Interferences.....	85
4.3.3. Ambient measurements.....	88
4.4. Conclusion .....	94

Chapter 5 Study of gas Initial steps of phase ozonolysis of important alkene using VUV photoionization time-of-flight mass spectrometry: cis-2-butene, tetramethylethylene and cyclohexene.....	99
5.1. Introduction.....	100
5.2 Experimental.....	104
5.3 Results.....	106
5.3.1 cis-2-butene + O <sub>3</sub> .....	106
5.3.2 tetramethylethylene (TME) + O <sub>3</sub> .....	117
5.3.3 cyclohexene + O <sub>3</sub> .....	126
5.4 Conclusion.....	133
Chapter 6 Study of gas Initial steps of phase ozonolysis of isoprene using VUV photoionization time-of-flight mass spectrometry.....	140
6.1. Introduction.....	141
6.2 Experimental.....	143
6.3 Results.....	145
6.4 Conclusion.....	156
Chapter 7 Study of gas Initial steps of phase ozonolysis of pinene using VUV photoionization time-of-flight mass spectrometry.....	160
7.1 Introduction.....	161
7.2. Experimental.....	163

7.3. Results.....	165
7.4 Conclusion .....	173
Chapter 8 Measurement of aerosol optical extinction using diode laser cavity ringdown spectroscopy.....	177
8.1. Introduction.....	178
8.2. Experimental .....	183
8.2.1 The CRDS system.....	183
8.2.2 Laboratory aerosol generation and monitoring.....	186
8.2.3 Ambient measurements .....	188
8.2.4 Extinction efficiency calculations .....	188
8.3. Results and discussion .....	189
8.3.1 Comparison between the Mie theory calculations and the CRDS measurements.....	189
8.3.2 Ambient measurements .....	193
8.4. Conclusion .....	197
Chapter 9 A new method of measuring the index of refraction and thickness of transparent thin-films using cavity – ring down spectroscopy.....	204
9.1 Introduction.....	204
9.2 Experimental .....	209
9.2.1. CRDS instrument setup.....	209

9.2.2 Experimental procedures .....	211
9.3 Theory and Modeling.....	214
9.4 Discussion.....	221
9.4.1 Discussion of 3-layer model experiment .....	221
9.4.2 Discussion of 4-layer model experiment .....	227
9.5 Conclusion .....	229
Chapter 10 Conclusion.....	234

# List of Figures

Figure 1-1 Tropospheric oxidation of hydrocarbon .....	3
Figure 2- 1 Schematics of the experimental setup for CRDS .....	13
Figure 2-2 Schematic of the photoionization time-of-flight mass spectrometer.....	17
Figure 3- 1 Schematic diagram of the ROx measurements using.....	33
Figure 3- 2 Example of ambient measurement on March 29, 2007.....	38
Figure 3- 3 Schematic diagram of the HO <sub>2</sub> calibration system. ....	39
Figure 3- 4 Schematics of calibration model .....	43
Figure 3- 5 Experimental calibration data .....	43
Figure 3- 6 A typical ambient air measurement (March 29, 2007) .....	48
Figure 3- 7 Ambient measurements of HO <sub>2</sub> /RO <sub>2</sub> at different time and days in 2007. The error bars (shown only for May 8, 2007) reflect the uncertainty in CL .....	53
Figure 4- 1 Schematic diagram of the ROx measurements using dual channel PERCA-CRDS.....	64
Figure 4- 2 Calibration of NO <sub>2</sub> cross sections from the CRDS and NOx analyzer measurement. ....	68
Figure 4- 3. Diode laser emission spectrum.....	70
Figure 4- 4 Dependence of CL of the calibration system on NO concentration.....	80
Figure 4- 5 Dependence of CL of the calibration system on CO concentration. ....	82

Figure 4- 6 Dependence of the CL of the calibration system and residence time .....	83
Figure 4- 7 Calibration curve of CRDS signal and CH <sub>3</sub> O <sub>2</sub> radical concentration. ....	85
Figure 4- 8 Dependence of CL on the relative humidity of the calibration system. ....	86
Figure 4- 9 Ambient air measurement of the RO <sub>x</sub> radicals on Jan 12, 2011.....	89
Figure 4- 10 Ambient measurements of RO <sub>x</sub> from sunrise to sunset on (a) Jan 13, 2011 and (b) Jan 14, 2011 .....	93
Figure 5- 1 Mass spectrum of ozone cis-2-butene reaction compared .....	109
Figure 5- 2 Mass spectrum of ozone TME reaction compared with blank spectrum ....	119
Figure 5- 3. Mass spectrum of ozone cyclohexene reaction compared with blank spectrum.....	128
Figure 6- 1 Mass spectrum of ozone isoprene reaction compared with blank spectrum.....	146
Figure 7- 1 Mass spectrum of ozone and α- pinene reaction compared with blank spectrum.....	167
Figure 7- 2 Mass spectrum of ozone and β- pinene reaction compared with blank spectrum.....	168
Figure 8- 1 Schematic diagram of the dual channel diode CRDS instrument for laboratory aerosol optical extinction measurements.....	184
Figure 8- 2 Measurements of extinction coefficient at 408.5 nm as a function of particle number density for particles.....	190

Figure 8- 3 Comparison of extinction cross sections at 408.5 nm from the Mie theory and the CRDS measurements for aerosols of sizes from 50 to 500 nm. ...	191
Figure 8- 4 Extinction efficiency $Q_e$ vs. the aerosol size (diameter) at 408.5 nm.....	192
Figure 8- 5 The extinction efficiency $Q_e$ vs. the size parameter $x$ at 408.5 nm. ....	193
Figure 8- 6 Ambient aerosol distribution obtained by SMPS through the sample system. There might be some wall loss.....	195
Figure 8- 7 CRDS measurement for ambient aerosol optical extinction coefficient in both the sample and reference channels. ....	196
Figure 9- 1 CRDS experimental setup for measurement of transparent thin film thickness.....	211
Figure 9- 2 A 0.0150mm BK7 cover glass with 650nm-670nm wavelength laser irradiation at different incident angles. (BA = Brewster Angle).....	214
Figure 9- 3 Illustration of (a) three- and (b)four- media systems encountered in reflection experiments.....	215
Figure 9- 4 3D surface modeling for decay rate with changing wavelength, index of refraction and film thickness. ....	220
Figure 9- 5 Comparison of (a) model and (b) data for one 0.150mm BK7 cover glass irradiated with 650nm-670nm wavelength laser under different incident angles.	225
Figure 9- 6 Experimental data under different conditions. ....	226



## List of Tables

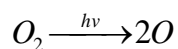
Table 5- 1 Peak assignments for the mass spectrum of ozone plus cis-2-butene .....	109
Table 5- 2 Mass spectrum of ozone plus TME .....	120
Table 5- 3. Mass spectrum of ozone plus cyclohexene.....	129
Table 6- 1. Mass spectrum of ozone plus isoprene .....	147
Table 7- 1. Mass spectrum of ozone plus $\alpha$ - piene peak assignment .....	169
Table 7- 2. Mass spectrum of ozone plus $\beta$ - piene peak assignment .....	170
Table 9- 1 Different conditions of experiment in the first step .....	212
Table 9- 2 Comparison of the film thickness getting by CRDS and Profilemeter .....	229

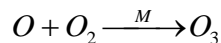
# Chapter 1 Introduction

Air pollution and global climate change are important environmental problems and issues that affect our society. The composition and chemistry of the atmosphere are important for many reasons, primarily because of the interactions between the atmosphere and living organisms. The composition of the Earth's atmosphere has been changed by human activity; some of these changes are harmful to human health, crops and ecosystems. Examples of the problems include acid rain, photochemical smog and global warming. To understand first and to control next these problems require deeper understanding of atmospheric chemistry, which seeks to reveal the causes of these problems and to evaluate the possible solutions and government policies.

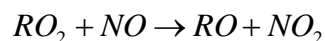
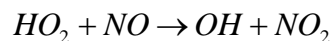
The troposphere is the region of the Earth's atmosphere in which we live and into which chemical compounds are generally emitted as a result of human activities. For example, emissions of oxides of nitrogen ( $\text{NO}_x$ ) and volatile organic compounds (VOCs) lead to a complex series of chemical and physical transformations, which result in such effects as the formation of ozone in urban and regional areas as well as in the global troposphere, acid deposition, and the formation of secondary particulate matter through gas/particle partitioning of both emitted chemical compounds and the atmospheric reaction products [1].

In a typical clean troposphere, ozone is generated from photolysis of  $\text{O}_2$ :

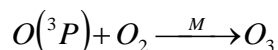
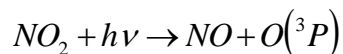




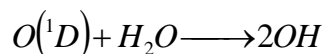
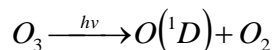
VOCs play an important role in the formation of tropospheric ozone in urban area because of their formation of peroxy radicals ( $RO_2$ ), which convert NO to  $NO_2$ :



$NO_2$  is then photolyzed by sunlight to yield a singlet oxygen, which reacts with molecular oxygen to produce ozone ( $O_3$ ):



An important oxidant that initiates peroxy radical formation from VOCs and drives daytime chemistry in the atmosphere is the hydroxyl radical (OH). A major source of the OH radicals in both clean and polluted air is the photodissociation of  $O_3$  in the upper troposphere by actinic UV radiation in sunlight to produce an electronically excited oxygen atom,  $O(^1D)$ , followed by a very rapid reaction with water.



Free radicals play the key roles as initiators and propagators of the chain reactions in atmospheric chemistry [2]. The complex tropospheric oxidation processes are illustrated in Figure 1-1, which shows that peroxy radicals ( $HO_2$  and

RO<sub>2</sub>) play critical roles in atmospheric chemistry. In the polluted atmosphere loading with hydrocarbon RH, HO<sub>2</sub> and RO<sub>2</sub> radicals are intermediate species generated during the oxidative conversion of RH. HO<sub>2</sub> may also be formed following HCHO photolysis and from the reaction of alkenes with ozone. The reactions of HO<sub>2</sub> with itself and other organic peroxy radicals are important to shape the atmospheric makeup, especially in clean troposphere. It is therefore critical to accurately measure the concentrations of the HO<sub>2</sub>/RO<sub>2</sub> radicals in the ambient atmosphere in order to understand their contribution to the air pollution, since atmospheric modeling requires HO<sub>2</sub>/RO<sub>2</sub> abundance to predict the atmospheric composition and to forecast air quality. Therefore, it is very important to develop very sensitive peroxy detector.

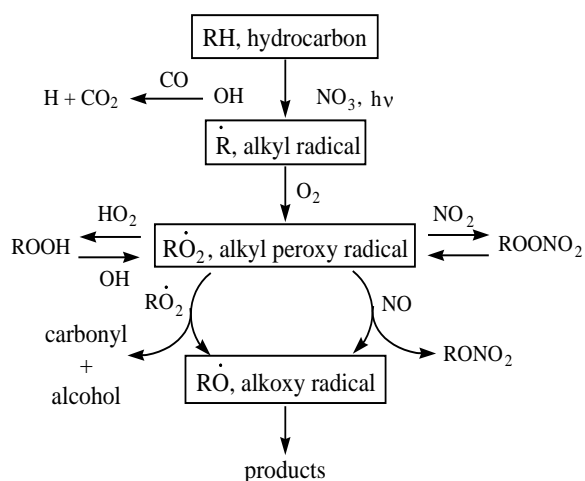


Figure 1-1 Tropospheric oxidation of hydrocarbon

Measurements of trace gas pollutants for ambient measurement require the use of instrumentation capable of measuring the pollutants at levels as low as parts per trillion (ppt) to several parts per billion (ppb) to elucidate the key atmospheric

chemical processes. Trace levels of stable VOCs are commonly measured offline using gas chromatography (GC) and gas chromatography/mass spectrometry (GC/MS) [3]. In addition to organics, many important gases of atmospheric interest ( $O_3$ ,  $NO_2$ ,  $NO_3$ ) possess strong absorption cross sections in the ultraviolet (UV) and visible region. As a result, spectroscopic methods have been developed to measure atmospheric pollutants in real time and continue to be the most commonly used and most reliable techniques for atmospheric measurements. Recently, new spectroscopic methods based on absorption spectroscopy, cavity ring-down spectroscopy (CRDS) [4-6] has been implemented for the measurement of pollutants in the atmosphere and smog chamber study. In this thesis, I focus on develop CRDS instruments for peroxy measurement.

Alkenes are a major class of VOCs emitted from both biogenic and anthropogenic sources. Ozonolysis reactions of alkenes are an important oxidation pathway of atmospheric alkenes, and they are also a significant source of OH radicals [7] (the key species in tropospheric oxidation and photochemical smog). Furthermore, these reactions are important in the production of secondary organic aerosols, which are known to have adverse health effects. A deeper insight into the mechanisms of the ozone-alkene reactions is essential for a comprehensive understanding of tropospheric oxidation of VOCs and air quality. To directly identify and characterize the transient intermediates in atmospheric chemistry reactions, mass spectrometry has been applied in this thesis work to study the reaction mechanisms.

Atmospheric aerosols have been suggested to contribute to climate change [8, 9], adverse human health effects [10, 11], and reduction in visibility [12]. Atmospheric aerosols interact with solar radiation by extinction of light, which includes both scattering and absorption. In general, the atmospheric aerosols absorb weakly that their extinction is mainly due to scattering. The atmospheric aerosols can directly influence the climate in the atmosphere by heating up the atmosphere aloft on one hand, and by reducing surface irradiance on the other hand. They can also alter the properties of clouds and thus indirectly influence the climate in the atmosphere [13].

Accurate measurement of the optical extinction of atmospheric aerosols is important for quantifying the direct climate effects of aerosols. Although the optical extinction of atmospheric aerosols has been measured for decades, a better understanding of the aerosol optical properties is still needed. In particular, in situ measurements of the extinction and other optical parameters of atmospheric aerosols are crucial, and these require real-time, accurate, and sensitive techniques that can detect the ambient aerosols and their rapid temporal and spatial changes.

In this thesis I will be presenting the CRDS instrumental development for measurements of ambient peroxy radical and aerosol extinction. Reaction mechanism studies of ozonolysis of important alkene are also presented using a homemade fast flow reactor coupled with a time of flight mass spectrometry, which provides an experimental dataset to improve model performance by evaluating the model with direct experiments of intermediate products.

In addition to the studies of atmospheric chemistry, for developing new application for CRDS technique, a novel method for transparent nanoscale thin film detection has been developed and demonstrated. In the past decade, there has been growing interest in techniques for depositing of various thin films for applications in many fields of microelectronics, as a result a large number of techniques have been developed for characterizing the properties of thin films and the information on thickness and optical constants of thin films is essential [14]. This method aims at determining the thickness of a non-absorbing thin film upon a nearly transparent substrate using CRDS, which has the advantages of high sensitive, real time, non-destructive and capable of thin film measurements on transparent substrate.

**Reference:**

1. Finlayson-Pitts, B.J. and J.N. Pitts, Chemistry of the upper and lower atmosphere : theory, experiments, and applications. 2000, San Diego.
2. Burkert, J., et al., Peroxy radical and related trace gas measurements in the boundary layer above the Atlantic Ocean. Journal of Geophysical Research-Atmospheres, 2001. **106**(D6): p. 5457-5477.
3. Sipin, M.F., S.A. Guazzotti, and K.A. Prather, Recent advances and some remaining challenges in analytical chemistry of the atmosphere. Anal. Chem., 2003. **75**: p. 2929-2940.
4. Berden, G. and R. Engeln, Cavity ring-down spectroscopy: techniques and applications. 2009: Wiley.

5. Hargrove, J., et al., Cavity ring-down spectroscopy of ambient NO<sub>2</sub> with quantification and elimination of interferences. *Environ. Sci. Technol.*, 2006. **40**(24): p. 7868-7873.
6. Brown, S.S., Absorption spectroscopy in high-finesse cavities for atmospheric studies *Chem. Rev.*, 2003. **103**(12): p. 5219-5239.
7. Atkinson, R., Gas-phase tropospheric chemistry of volatile organic compounds: 1. alkanes and alkenes. *J. Phys. Chem. Ref. Data*, 1997. **26**(2): p. 215-290.
8. IPCC. 2007, Intergovernmental Panel on Climate Change (IPCC).
9. Kanakidou, M., et al., Organic aerosol and global climate modelling: a review. *Atmospheric Chemistry and Physics*, 2005. **5**: p. 1053-1123.
10. Davidson, C.I., R.F. Phalen, and S. Solomon, Airborne particulate matter and human health: A review. *Aerosol Science and Technology*, 2005. **39**: p. 737-749.
11. Pope, C.A. and D.W. Dockery, Health effects of fine particulate air pollution: Lines that connect. *J. Air & Waste Manage. Assoc.*, 2006. **56**: p. 709-742.
12. Eldering, A. and G.R. Cass, Source-oriented model for air pollutant effects on visibility. *Journal of Geophysical Research*, 1996. **101**(D14): p. 19343-19369.
13. Seinfeld, J.H. and S.N. Pandis, *Atmospheric Chemistry and Physics: from Air Pollution to Climate Change*. 1998, New York: John Wiley.



14. Jung, C. and B.K. Rhee, Simultaneous determination of thickness and optical constants of polymer thin film by analyzing transmittance. *Appl. Opt.*, 2002. **41**(19): p. 3861-3865.

## Chapter 2 Experimental techniques

### **Abstract:**

Cavity ring down spectroscopy (CRDS) is direct absorption spectroscopic technique, which has a significantly higher sensitivity than obtainable in conventional absorption spectroscopy. The CRDS technique is based on the measurement of the rate of absorption rather than the magnitude of absorption of a light pulse confined in a closed optical cavity. The advantage over normal absorption spectroscopy results from, firstly, the intrinsic insensitivity to light source intensity fluctuations and, secondly, the extremely long effective path lengths (many kilometers) that can be realized in stable optical cavities. These cavity based optical techniques are employed in detecting different trace gases in the atmosphere in this dissertation.

In addition, gas phase reactions were studied in a fast flow reactor coupled with a VUV photonionization time-of-flight mass spectrometry (TOFMS). The fast flow reactor allows the early-stage reaction intermediates and mechanisms to be probed. The VUV photonionization TOFMS has a soft ionization energy which is 118.2 nm (10.48 eV), which minimizes photoionization fragmentation. This technique combining the fast flow reactor with VUV photonionization TOFMS is employed in experimental studies presented in this dissertation.

This chapter summarizes the principle, experimental setup and applications of those instruments.

## **2.1 Cavity ring-down spectroscopy**

Cavity ring-down spectroscopy (CRDS) is a direct light absorption technique [1]. It can use a pulsed or a continuous light source, and has a significantly higher sensitivity and a simple, straightforward experimental setup over the conventional multi-pass absorption technique. Many studies using CRDS have proven that this technique is especially powerful in gas-phase spectroscopic measurements of either strong absorptions of atmospheric trace species, or weak absorptions of abundant species [2, 3]

### **2.1.1 Introduction**

A conventional absorption technique measures attenuation of the intensity of light that is transmitted through a sample. One of the drawbacks of the conventional absorption techniques is the limited sensitivity. A small attenuation in transmitted light must be measured in the presence of large initial light intensity. In order to improve the sensitivity, one can use modulation schemes and increase the absorption path length, but these are not always feasible. Different from conventional absorption techniques, CRDS is based on the measurement of the rate of absorption rather than the magnitude of the absorption of a light pulse confined in an optical cavity. The analyte is placed inside an optical cavity consisting of two highly reflective mirrors. A pulsed light is directed into the cavity and reflected back and forth between the two mirrors. Each time the light is reflected by the mirrors, there is a small fraction loss due to the mirrors transmission [1]. Instead of monitoring the

light intensity inside the cavity, one can monitor the time dependence of the transmitted light: the more absorption of light by sample, the shorter decay time is measured. In this way, the rate at which the light is absorbed can be obtained, and it can be related to the absorption of the sample in the cavity.

### **2.1.2 Principle**

The essential features of a CRDS are shown in Figure 2-1[3]. The ring-down cavity cell consists of two highly reflective mirrors, with reflectivity (R) normally larger than 0.99. These two mirrors are mounted in adjustable mounts so that they can be adjusted and aligned. The two cavity mirrors also act as entrance and exit windows of the cell. After a laser pulse is injected and trapped inside the cavity, the light is reflected back and forth inside the cavity. Every time the light is reflected by the mirrors, a small fraction leaks out of the cavity because of the transmission throughout the mirrors. Instead of measuring the total intensity of the light exiting the cavity, one determines the ring-down decay time by measuring the time dependence of the light intensity leaking out with photon detector, such as photomultiplier tube (PMT). In this way, the rate of the absorption can be obtained. The intensity of light ( $I_{out}(t)$ ) within the cavity is determined as an exponential function of time:

$$I_{out}(t) = I_{out}^0 \cdot \exp(-t / \tau) \quad (2-1)$$

The ring-down decay time is dependent on the loss of the light intensity within the cavity. In an empty cavity, this ring-down decay time ( $\tau_0$ ) depends on mirror losses and various optical phenomena like scattering and refraction:

$$\tau_0 = \frac{L}{c(1-R+X)} \quad (2-2)$$

where  $c$  is the light velocity in vacuum,  $L$  is the cavity length, and  $X$  takes into account other optical losses such as scattering and refraction. Since the contributions of scattering and refraction to optical losses are generally much smaller than the reflection losses of the cavity mirrors,  $X$  can be omitted in eqn (2-1). With an absorbing species in the cavity, the losses of light will increase according to Beer-Lambert law. The ring-down decay time ( $\tau$ ) depends on both mirror losses and sample absorption:

$$\tau = \frac{L}{c(1-R+\sigma NL)} \quad (2-3)$$

where  $\sigma$  is the absorption cross section of the absorber,  $N$  is the number density of the absorber inside the cavity. The ring-down decay time is on the order of tens of microseconds in the absence of absorbing species but shortens in the presence of an absorbing sample. By measuring the ring-down decay time with and without an absorber, the optical loss due to its absorption can be obtained.

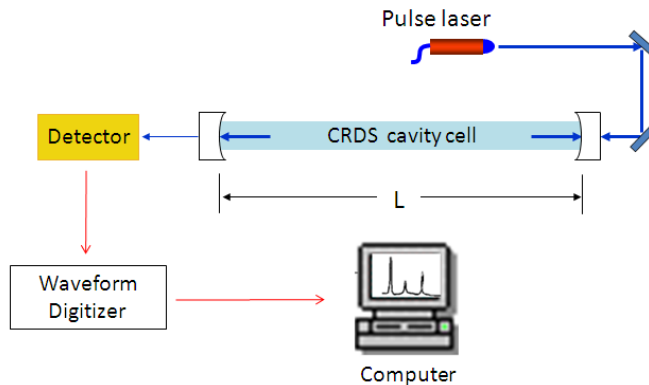


Figure 2- 1 Schematics of the experimental setup for CRDS

CRDS is a quantitative and absolute method. It is capable of measuring species of known absorption cross sections by taking the difference between the ring-down decay rate with sample ( $1/\tau$ ) and the background decay rate without sample ( $1/\tau_0$ ):

$$\alpha = \frac{L}{cl_s} \left( \frac{1}{\tau} - \frac{1}{\tau_0} \right) = \sigma N \quad (2-4)$$

where  $\alpha$  is the absorption coefficient,  $L$  is the cavity length, and  $l_s$  is the sample path length. The resulting absorption coefficient,  $\alpha$ , can then be divided by the cross section ( $\sigma$ ) to yield the concentration or number density ( $N$ ). One advantage of this method is that errors in the measurement of  $1/\tau$  and  $1/\tau_0$  at least partially cancel out during the subtraction. If the intensity of the light drops or there is contamination on the mirrors, the signal to noise ratio will decrease, but the resulting calculation of the concentration remains unchanged. If the absorbing species can be selectively removed from the sample stream, this method does not need any calibration gasses.

Therefore, CRDS is a high sensitive method with the ability for trace measurements without calibration gasses and free of interferences.

### 2.1.3 Sensitivity

The minimum detectable absorption in CRDS depends on the reflectivity of the mirrors and the accuracy in the determination of decay time ( $\tau$ )[4]. The accuracy of decay time ( $\Delta\tau/\tau$ ) is determined by many factors like laser modes, cavity modes, detector, data acquisition and data analysis, and it is reported to be on the order of percent by most of the CRDS experiments. The sensitivity of the CRDS is generally between  $10^{-6}$  and  $10^{-9}$   $\text{cm}^{-1}$  based on previous measurements [2]. Assume the absorber crosssection is  $1 \times 10^{-18}$   $\text{cm}^{-2}$ , the calculated number density of the absorber is between  $10^9$  to  $10^{13}$  molecules  $\text{cm}^{-3}$ .

In addition to the rate changes from transmittance through mirrors and absorption, another prominent cause of light intensity loss inside the cavity during the ambient measurements is Rayleigh scattering by air. The cross-section for Rayleigh scattering can be approximated as [5]:

$$\sigma_{\text{Rayleigh}}(\lambda) = \frac{8\pi^3}{3} \left[ \frac{(n^2 - 1)^2}{N^2 \lambda^4} \right]$$

where  $n$  is the refractivity of air ( $n - 1 =$  tens - hundreds ppm),  $N$  is the number density of gas, and both  $n$  and  $N$  are dependent on the temperature and pressure.[6, 7] Changes in temperature and pressure on the order of 10 °C and 50 mbar, respectively,

can have a significant effect on Rayleigh scattering. Thus, CRDS detection could be difficult in an environment of rapidly-changing temperature and/or pressure. In most cases, however, the ambient drift of temperature and pressure is slow, and can be compensated by regular monitoring of  $1/\tau_0$  with the same sample air without the interested absorber. Or alternately, there is a better solution to use a second CRDS detector as a reference channel for monitoring the background.

#### **2.1.4 Features and Applications**

CRDS has several advantages over conventional absorption spectroscopy. Since the absorption determination is based on the time behavior of the signal, it is independent of the pulse-to-pulse fluctuations of the laser. Second, the sample absorption path length, which depends on the reflectivity  $R$  of the cavity mirrors, can be as long as several kilometers, while the sample volume is still kept very small. Compared to other sensitive absorption techniques which use internal standards and references, CRDS has the additional advantage of making direct measurements. Furthermore, it is rather simple to construct a system since it only needs a few components. The disadvantage of CRDS is that it requires highly reflective mirrors which are quite expensive and has limited bandwidth within ( $\pm 15\%$  of the central wavelength), a suitable light source, and a detector with fast response.

CRDS has been performed in quite a large spectral region, from the ultraviolet (200 nm) to the infrared (10  $\mu\text{m}$ ). CRDS could be used to obtain spectroscopic



information on atoms, molecules, ions, clusters and even molecules in the solid phase. CRDS has been applied in many environments, such as open air, static gas cell, supersonic jets, flames and discharges. In the current study, CRDS is explored either to measure the absorption of target gas molecules, or to probe for possible transient products from the photolysis of their precursors.

## **2.2 Faster flow reactor combined with time-of-flight mass spectrometer**

The gas phase reactions have been studied in a fast flow reactor coupled with a VUV photoionization time-of-flight mass spectrometry (VUV PI TOFMS) through a 0.26 mm diameter sampling orifice. The experimental system is consisted of a fast flow reactor, in which radicals and products are generated, and a linear TOFMS, in which radicals and products are detected. This configuration is shown in Figure 2-2.

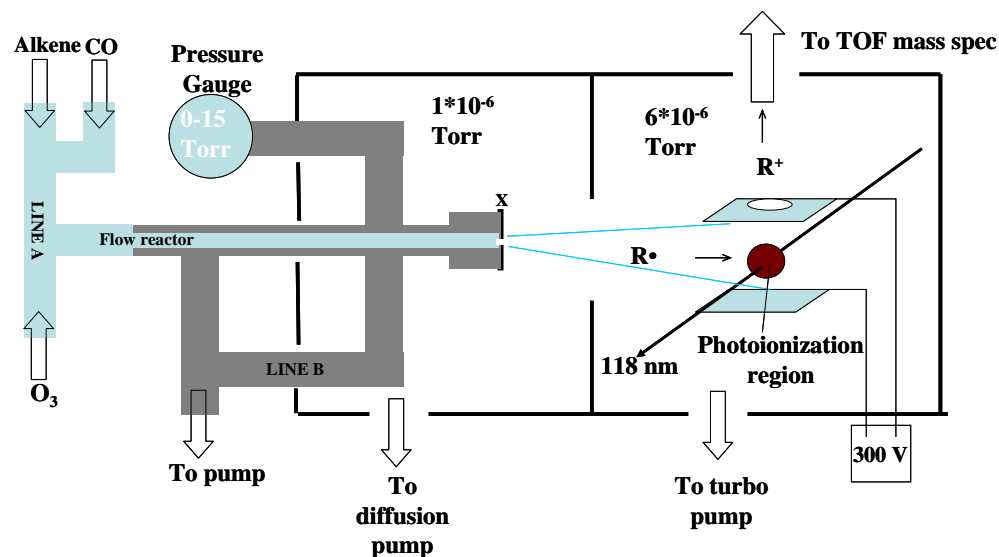


Figure 2- 2 Schematic of the photoionization time-of-flight mass spectrometer.

### 2.2.1 Faster flow reactor

Fast flow reactions were performed in the apparatus schematically depicted in Figure 2-2. In those investigated systems, the reactant gases are injected in line A and reacted. The exhausted line is line B. In the reactor, the pressure of the was kept at 7 – 11 Torr for all measurements. The fast flow reactor was based on the design of Clay and Ault [6] and further modified by us, in which the ozone and alkene encounter in line A and are permitted to mix and react during passage through the flow reactor. To avoid the surface reaction of the gas samples, the inlet and flow reactor are constructed of Teflon FEP. To probe the initial steps of reactions, a short reaction time scale is required (in tens of milliseconds level). In this approach, line A works as a plug flow reactor, where the gases merged and then reacted. The flow reactor of line A is combined with a 50 – 180 cm long, 1/8" O.D. Teflon FEP tube

and a 1/4" O.D. Teflon FEP tube, whose length could be varied to approach different reaction times. The 1/8" O.D. Teflon FEP tube is inserted inside of a larger, 1/4" O.D. standard steel tube (Line B). At the joint end of line A and line B, a 0.26 mm sampling orifice (X in Figure 2-2) is opened to the TOFMS main chamber. Mixing of ozone, CO and alkene begins at the 1/4" O.D. Teflon FEP tube where the gases encounter and react continuously along both the 1/4" tube and the 1/8" tube until reaching sampling orifice X. To keep a fast flow, a mechanic pump is used to pump line B from both the outside tube of line A and another port of line B. Therefore, most of the gas mixture is pumped away by line B and only a small portion of the gas mixture can pass through the sampling orifice X to arrive in the ionization region and then be detected by TOFMS. The third port of line B is linked with a pressure gauge with which the pressure of the flow reactor could be monitored. This configuration ensures a millisecond time scale while maintaining a necessary low pressure in the TOF main chamber. Another advantage of this fast flow reactor is that the outlet of the reactor is right in front of the sampling orifice, which eliminated the "dead volume" of the reactor and provides the possibility to detect the nascent products, including free radicals. The linear velocity of the sample within the flow reactor is around 3500 cm/s which correlate to an approximate 20-100 ms residence time depending on different experiments. Upon exiting the orifice, the products and remaining reactants were cooled and isolated by supersonic expansion into a molecular beam where they proceeded to the photoionization region.

The longer reaction time and 1 atm experiments are carried out using similar setup except with a pulsed valve (General Valve series 9) instead of the continuous orifice and no pumps connect to line B. This pulsed sampling configuration allows us to run an ambient pressure (1 atm) reaction in the much slower reactor while keep a low pressure ( $1 \times 10^{-5}$  Torr) in the main chamber. And since the reactions are studied with long reaction time (1-10 s), the “dead volume” of the pulsed valve is no longer an issue.

### **2.2.2 Molecular Beam Theory[7]**

Under this experimental configuration, when the reaction intermediates pass through the sampling orifice X to arrive in the photoionization region, it becomes supersonic molecular beam. The use of a supersonic molecular beam in our apparatus provides many advantages which will be explained in this section.

A free-jet molecular beam is a neutral beam extracted from the continuous jet expansion of a gas from a high pressure reservoir to a low-pressure region, similar to the converging-diverging expansion of supersonic rocket nozzles. The unique properties of these molecular beams are due to the supersonic nature of the gas, which is the result of the "underexpansion" of the gas, and will be explained below. In the high pressure region of the molecular beam nozzle, known as the "stagnation state," the gas has a negligibly small velocity. The gas velocity increases as the nozzle constricts and the area decreases toward the source exit. At the source exit,

the gas can reach sonic speed (Mach number = 1) when the ratio of reservoir pressure to background pressure,  $P_0/P_b$ , becomes greater than

$$G \equiv \left( \frac{\gamma + 1}{2} \right)^{\frac{\gamma}{\gamma - 1}}$$

where  $\gamma$  is the ratio of heat capacities at constant pressure versus constant volume,  $C_p/C_v$ . When  $P_0/P_b$  is greater than  $G$ , then the exit pressure  $\approx P_0/2$ , which is independent of the background pressure,  $P_b$ , and thus the expansion is termed "underexpanded."

Two major characteristics of supersonic flow are 1) supersonic flow velocity increases as the flow area increases, and 2) the particles in the beam can not sense downstream conditions due to their supersonic nature- i. e. the flow of information is limited to the speed of sound. Essentially, particles traveling in the same direction with the same velocity cannot interact with each other. Eventually, collisions with the background gas in the expansion chamber will reduce the molecular beam flow to a subsonic velocity, introducing shock waves which are regions with large pressure, temperature, and velocity gradients. Where these shock waves occur depend largely on the  $P_0/P_b$  pressure ratio and the nozzle diameter,  $d$ . The region where the first shock wave appears downstream from the nozzle is known as the "Mach disk," and the region where the expansion creates supersonic flow is called the "zone of silence" (see figure 2.2). The Mach disk is located at

$$x_m/d = 0.67 \left( \frac{P_0}{P_b} \right)^{1/2}$$

which is in units of nozzle diameters. The thermodynamics of a free jet assume the gas is an ideal gas, and neglect viscosity and heat conduction effects, and the expansion is isentropic. By the First Law of Thermodynamics, enthalpy and kinetic energy are conserved:  $H + V^2/2 = H_0$ , where  $H_0$  is the stagnation enthalpy per unit mass. As the gas expands and cools,  $H$  decreases and  $V$  increases. In other words, enthalpy is converted to kinetic energy of the gas particles, which also have a definite directionality.

In order to determine the velocity of the molecular beam, we can introduce the relationship between enthalpy and heat capacity:

$$dH = C_p dT$$

which leads to the expression:

$$V^2 = 2 \int_H^{H_0} dH = 2(H_0 - H) = 2 \int_T^{T_0} C_p dT = 2C_p(T_0 - T)$$

where

$$C_p = \left( \frac{\gamma}{\gamma - 1} \right) \left( \frac{R}{MW} \right)$$

When  $T \ll T_0$  due to efficient supersonic cooling, the terminal velocity can be determined:

$$V_\infty = \sqrt{\frac{2R}{MW} \left( \frac{\gamma}{\gamma - 1} \right) T_0}$$

Note that the terminal velocity is dependent only on the nozzle temperature and the molecular weight of the gas, and is independent of the source pressure or nozzle

diameter. The beam temperature, however, depends on the collision frequency at the exit, and is dependent upon  $P_0$  and  $d$ , which will be discussed below.

Because the terminal velocity is inversely proportional to the square root of the *average* molecular weight in a gas mixture, this allows for the acceleration of a heavy species by diluting it in a lighter gas, or conversely, deceleration of a lighter species by dilution in a heavier gas. This practice is known as "seeding," where, in a binary gas mixture, the species with a small mole fraction is known as the "seed" gas, and the species with a large mole fraction is known as the "carrier" gas.

The transition from continuum flow to free molecular flow occurs when the collision frequency can no longer maintain continuum flow. This is referred to as the freezing region because, in the absence of molecular collisions, the beam properties are frozen in, which generally occurs when the beam velocity reaches 98% of the terminal velocity. This occurs within the first several nozzle diameters distance from the source exit.

The temperature within the beam is usually characterized by the spread in molecular velocities about the beam mean velocity. The vibrational and rotational temperatures of molecules are lowered by the cooling effect of the expansion as well, which is useful for simplifying and interpreting complicated fluorescence spectra. Using these cooling effects minimizes further reactions by avoiding reactive collisions within the beam.

### 2.2.3 VUV PI TOFMS

Fast flow reactions are performed in the apparatus schematically depicted in Figure 2-2, and the investigated reactions intermediates are sampled as supersonic molecular beam, where it is detected by a Wiley-Mac Laren type linear time-of-flight mass spectrometer (TOFMS, model D-651, R. M. Jordan Company [8]). This TOFMS monitors the reactions intermediates products by 118 nm (10.45 eV) photonization. Typical resolution attainable with this TOFMS is 200 at  $m/e=150$ . The main reaction chamber was pumped by a cryobaffled Varian VHS-6 diffusion pump, and the mass spectrometer was differentially pumped with a turbomolecular pump and sometimes in addition with a liquid nitrogen cooled cryotrap.

After exiting from the fast flow reactor, the unreacted reactants and their products are cooled and isolated by supersonic expansion. Reaction products are ionized by single photon ionization at 118 nm (10.49 eV), using the frequency tripled third harmonic (355 nm) of a Nd:YAG laser output in a low pressure (15 – 20 Torr) Xe cell attached directly to the vacuum chamber[9]. The VUV radiation is focused into the chamber with a  $MgF_2$  lens, and the intensity at these wavelengths is maximized by measuring the photoionization current of organics in an ionization cell located at the back of the chamber. The ion current produced is measured as a voltage drop between two electrode plates within this cell, biased at 0 and +180 volts. Alignment of the molecular beam and the photoionizing radiation is optimized by changing the positions of the 355 nm focusing lenses and the molecular beam nozzle to give a maximum intensity mass peak when running



samples of interest through the molecular beam nozzle. Data are averaged with a Tektronix TDS3032 digital oscilloscope (300 MHz, 512 laser shots) and recorded with LabView software, or on a multi-channel scaler (EG&G Turbo-MCS, 2000 laser shots), with sampling rate of 10 Hz.

The 118 radiation is focused by a MgF<sub>2</sub> lens through a small aperture into the photoionization zone, while the fundamental 355 beam diverged in this region. This divergence and aperture minimized multi-photon ionization (MPI) and the amount of scattered 355 nm radiation within the ionization region.

This technique presents many advantages: 1) a short reaction time to examine the initial steps of reaction, 2) supersonic cooling quenches the reaction, resulting in the minimal recombination of products and intermediates, and 3) minimal ion fragmentation by the use of the 10.49 eV “soft” ionization source that imparts sufficient energy to ionize many of the products. Supersonic cooling further reduces photoionization fragmentation by minimizing the internal energy of reaction products.

One of the limitations of this apparatus is the occurrence of a small amount of electron-impact ionization (EI) resulting from photoelectrons produced by scattered light within the photoionization region. A small amount of ionization takes place as a result of electrons that are generated from metal surfaces by the photoelectric effect and accelerated. Efforts are made to eliminate this effect, such as minimizing the 355 nm spot size and masking the photoionization region from the (diverging) 355 nm beam. These attempts to eliminate all EI contributions result in the loss of the photoionization signal as well. A compromise is made to minimize the EI

contribution while retaining sufficient photoionization signal. The possibility of multi-photon ionization (MPI) occurring has also been considered. In the design of the 118 nm source, due to differences in the indices of refraction of 118 and 355 nm wavelengths, the 118 nm light is focused in the photoionization region, while the 355 nm light diverges here. Large fluences are required to initiate a measurable MPI signal, thus multi-355 nm photon ionization is unlikely. MPI with 118 + 355 nm photons (14.0 eV) is also unlikely which has been demonstrated in our lab before[10].

**Reference:**

1. O'keefe, A. and D.A.G. Deacon, *Cavity ring-down optical spectrometer for absorption measurements using pulsed laser sources*. Review of Scientific Instruments, 1988. 59(12): p. 2544-2551.
2. Berden, G. and R. Engeln, *Cavity ring-down spectroscopy: techniques and applications*. 2009: Wiley.
3. Berden, G., R. Peeters, and G. Meijer, *Cavity ring-down spectroscopy: Experimental schemes and applications*. International Reviews in Physical Chemistry, 2000. 19(4): p. 565-607.
4. Zalicki, P. and R. Zar, *Cavity ring-down spectroscopy for quantitative absorption measurements*. J. Chem. Phys., 1995. 102(2708-2717).
5. Sappey, A.D., et al., *Fixed-frequency Cavity Ringdown Diagnostic for Atmospheric Particulate Matter*. Optics Letters, 1998. 23(12): p. 954-956.

6. Clay, M.A., Bruce S., *Infrared Matrix Isolation and Theoretical Study of the Initial Intermediates in the Reaction of Ozone with cis-2-Butene* Journal of Physical Chemistry A, 2010. 114(8): p. 2799-2805.
7. Scoles, G., ed. *Atomic and Molecular Beam Methods*. Vol. vol. 1. 1988, Oxford University Press: New York.
8. Lubman, D.M. and R.M. Jordan, *Design for improved resolution in a time - of -flight mass spectrometer using a supersonic beam and laser ionization source*. Review of Scientific Instruments, 1985. 56(3): p. 373-376.
9. Chambreau, S.D., et al., *Photoionization of methyl t-butyl ether (MTBE) and t-octyl methyl ether (TOME) and analysis of their pyrolyses by supersonic jet/photoionization mass spectrometry*. International Journal of Mass Spectrometry, 2000. 199(1-3): p. 17-27.
10. Cahmbreau, S.D. and J. Zhang, *VUV Photoionization time-of-flight mass spectrometry of flash pyrolysis of silane and disilane*. Chem. Phys. Lett., 2001. 343(5-6): p. 482-488.

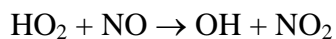
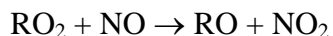
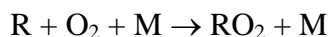
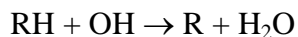
# Chapter 3 Measurements of Peroxy Radicals Using Chemical Amplification – Cavity Ringdown Spectroscopy

## Abstract

The peroxy radical chemical amplification (PERCA) method is combined with cavity ringdown spectroscopy (CRDS) to detect peroxy radicals ( $\text{HO}_2$  and  $\text{RO}_2$ ). In PERCA,  $\text{HO}_2$  and  $\text{RO}_2$  are first converted to  $\text{NO}_2$  via reactions with  $\text{NO}$ , and the  $\text{OH}$  and  $\text{RO}$  co-products are recycled back to  $\text{HO}_2$  in subsequent reactions with  $\text{CO}$  and  $\text{O}_2$ ; the chain reactions of  $\text{HO}_2$  are repeated and amplify the level of  $\text{NO}_2$ . The amplified  $\text{NO}_2$  is then monitored by CRDS, a sensitive absorption technique. The PERCA-CRDS method is calibrated using a  $\text{HO}_2$  radical source (0.5-3 ppbv), which is generated by thermal decomposition of  $\text{H}_2\text{O}_2$  vapor (permeated from 2%  $\text{H}_2\text{O}_2$  solution through a porous Teflon tubing) up to  $600^\circ\text{C}$ . Using a 2-meter long 6.35-mm o.d. Teflon tubing as the flow reactor and 2.5 ppmv  $\text{NO}$  and 2.5-10% vol/vol  $\text{CO}$ , the PERCA amplification factor or chain length,  $\Delta[\text{NO}_2]/([\text{HO}_2]+[\text{RO}_2])$ , is determined to be  $150 \pm 50$  (90% confidence limit) in this study. The peroxy radical detection sensitivity by PERCA-CRDS is estimated to be  $\sim 10$  pptv/60 s ( $3\sigma$ ). Ambient measurements of the peroxy radicals are carried out at Riverside, California in 2007 to demonstrate the PERCA-CRDS technique.

### 3.1 Introduction

Peroxy radicals (hydroperoxy HO<sub>2</sub> and organic peroxy RO<sub>2</sub>) play significant roles in the photochemistry of the troposphere. They are involved in the production and removal of ozone in photochemical cycles through the competition between oxidation of NO by RO<sub>2</sub> and O<sub>3</sub>, and they are also closely related to hydroxyl (OH) radical in atmospheric radical budgets [1]. In the polluted air with hydrocarbon RH and NO<sub>x</sub> (NO + NO<sub>2</sub>), HO<sub>2</sub> and RO<sub>2</sub> radicals involve in the following reactions:

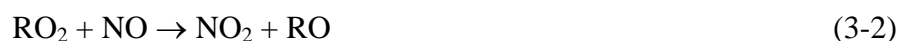


HO<sub>2</sub>, organic oxy (RO), and organic peroxy (RO<sub>2</sub>) radicals are formed in the atmospheric reactions of OH with hydrocarbons as shown above. HO<sub>2</sub> is also formed following the atmospheric reaction of OH with CO, HCHO photolysis, and some NO<sub>3</sub> reactions, as well as reactions of alkenes with ozone [1].

It is important and challenging to accurately measure the trace and reactive tropospheric peroxy radicals, especially in situ and in real time. Several methods have previously been developed for the peroxy radical detection. The matrix isolation and electron spin resonance (MI-ESR) method measures HO<sub>2</sub> and RO<sub>2</sub> directly and specifically using off-line ESR after cryogenic matrix isolation and enrichment of the peroxy radicals [2, 3]. This technique requires a long sample accumulation time of approximately 30 min to achieve sufficient sensitivity, and the typical detection limit is ~5 pptv. The laser-induced fluorescence (LIF) method monitors HO<sub>2</sub> indirectly, by converting HO<sub>2</sub> to OH with the NO + HO<sub>2</sub> reaction and detecting OH by LIF [4-7]. While the LIF method has a detection sensitivity of 10<sup>6</sup>-10<sup>7</sup> molecules/cm<sup>3</sup> for HO<sub>2</sub>, it is complex and requires careful calibrations [4-7]. Peroxy radical chemical amplification (PERCA) is a widely utilized indirect method to measure the total concentrations of peroxy radicals [8-19]. The PERCA technique is sensitive to total RO<sub>x</sub> (OH + HO<sub>2</sub> + RO + RO<sub>2</sub>), but since the atmospheric concentrations of OH and RO are much smaller than those of HO<sub>2</sub> + RO<sub>2</sub>, PERCA effectively measures the sum of HO<sub>2</sub> + RO<sub>2</sub>. The PERCA method was first developed by Cantrell et al. in 1980's [8, 9], and later by Hastie et al. [12] and others [13-19]. In PERCA, the peroxy radicals are converted to a larger amount of NO<sub>2</sub> in chain reactions by adding high concentrations of NO and CO in a flow reactor. The amplified NO<sub>2</sub> level is then detected by sensitive NO<sub>2</sub> detection methods. One approach to detect NO<sub>2</sub> is chemiluminescence reaction of NO<sub>2</sub> with luminal [8, 12, 14]; the detection limit varies from 0.2 to 2 pptv for a 30-min averaging time but this

detection method could suffer from interferences from other oxidants. Another one is LIF detection of NO<sub>2</sub>, which was developed by Sadanaga and co-workers [17]; the calibration, including humidity dependence of the detection sensitivity of the peroxy radicals, was conducted. The detection limit of the peroxy radicals in the study was determined to be 2.7 and 3.6 pptv at the ambient relative humidity of 50 and 80%, respectively [17]. Reiner et al. used SO<sub>2</sub> instead of CO to carry out chain reactions to produce H<sub>2</sub>SO<sub>4</sub> instead of NO<sub>2</sub> [20], and H<sub>2</sub>SO<sub>4</sub> is detected by chemical ionization mass spectrometry (CIMS) [20]. A similar method, peroxy radical chemical ionization mass spectrometer (PerCIMS) [21] is developed by Cantrell et al., in which HO<sub>2</sub> is also converted to H<sub>2</sub>SO<sub>4</sub> using NO and SO<sub>2</sub>, followed by CIMS detection. These two methods could measure the sum of HO<sub>2</sub> + RO<sub>2</sub> or HO<sub>2</sub> only by controlling the reaction conditions for RO<sub>2</sub> to HO<sub>2</sub> conversion. The detection limit of the CIMS techniques is 0.5-1.0 pptv in 15-60 sec.

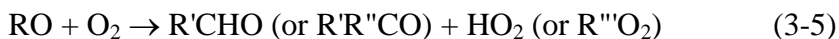
The key feature of PERCA using NO and CO is to convert HO<sub>2</sub> and RO<sub>2</sub> to NO<sub>2</sub> via reactions with an excess amount of NO, with subsequent reactions to recycle most of the OH and RO coproducts back to HO<sub>2</sub> by reactions with an excess amount of CO in O<sub>2</sub> and amplify the level of NO<sub>2</sub>. The chain reaction mechanism of PERCA using NO and CO is summarized in the following steps [9, 10, 17]. The HO<sub>2</sub> and RO<sub>2</sub> radicals in the air sample react with NO first to produce OH and RO plus NO<sub>2</sub> in the initial steps of the chain reactions:



When in an environment of a great concentration of CO and O<sub>2</sub>, the chain reactions involving HO<sub>2</sub> can continue and bring back HO<sub>2</sub> to the initial steps:



Similarly, the RO radical—produced in eqn. (2) — reacts with O<sub>2</sub> to form HO<sub>2</sub> or RO<sub>2</sub>, which could return to the initial steps:



By these reactions and cycles with NO, CO and O<sub>2</sub>, RO<sub>2</sub> + HO<sub>2</sub> radicals can increase the level of NO<sub>2</sub> by hundreds of times. The amplified NO<sub>2</sub> is then detected by a NO<sub>2</sub> analyzer, indirectly providing information of the concentrations of RO<sub>2</sub> + HO<sub>2</sub>.

The level of amplification and thus the sensitivity of PERCA are limited by radical removal processes from the system. The following are some of the chain termination reactions of HO<sub>2</sub>:



Among these processes and the similar ones for RO<sub>2</sub>, wall losses are likely most significant and difficult to quantify [10, 12, 13].

To accurately measure the concentrations of RO<sub>2</sub>/HO<sub>2</sub> in the PERCA method, the number of NO<sub>2</sub> molecules produced per peroxy radical, which is called



amplification factor or chain length (CL) [9, 10, 12], must be determined. This factor depends on the rates of reactions, concentrations of the reagents, removal processes of radicals from the system, and other experimental conditions such as flow rates of the reagent gases, reaction time, etc. The typical CL values are in the range of 100-200 [13, 14, 17].

In this work, the PERCA method is combined with cavity ringdown spectroscopy (CRDS) for peroxy radical detections. CRDS is a highly sensitive absorption technique based on measurement of the rate of light attenuation by a sample [22-25]. CRDS has been applied to detection and quantitative analysis of ambient air pollutants such as NO<sub>2</sub> [25]. In this study, the amplified NO<sub>2</sub> signal in PERCA is measured directly using CRDS, with high sensitivity and fast time response [25]. Compared with the detection of NO<sub>2</sub> with luminol, the CRDS detection of NO<sub>2</sub> provides direct spectroscopic measurements on NO<sub>2</sub> with minimum interferences. Compared with the LIF detection of NO<sub>2</sub>, the CRDS setup is simpler, is not affected by quenching of electronically excited NO<sub>2</sub>, and could provide absolute concentrations of NO<sub>2</sub> without calibration gas. The PERCA-CRDS method is calibrated using a HO<sub>2</sub> radical source, and ambient measurements of the peroxy radicals RO<sub>2</sub>/HO<sub>2</sub> are carried out.

## 3.2 Experimental

The PERCA-CRDS instrument has two major components: (1) a flow-reactor system for PERCA, including the chain reactions with and without amplification; and (2) the CRDS setup, as the detection system for NO<sub>2</sub>. The complete ambient monitoring of peroxy radicals includes both ambient measurements and calibration of the amplification factor or CL of PERCA under laboratory control; both are carried out under the same conditions of the reaction system.

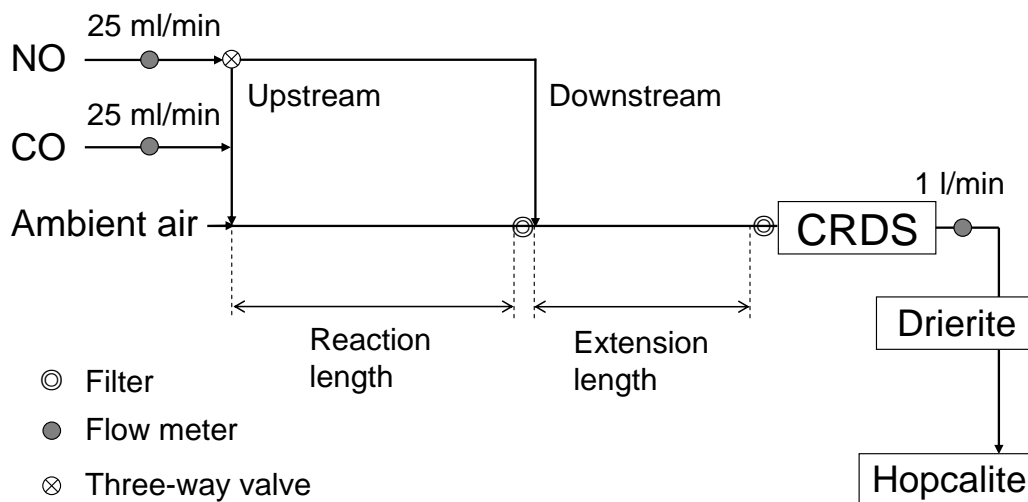


Figure 3- 1 Schematic diagram of the ROx measurements using

### 3.2.1 Chemical reaction system and ambient measurements

The chemical reaction system is composed of a flow reactor to carry out the chain reactions; the schematic of our PERCA setup is shown in Figure 3-1. Several reaction system setups for PERCA have been reported before. The original

configuration was developed by Cantrell et al. [8], and it was improved later by Hastie et al. [12], Cantrell et al., [10] Hu and Stedman [13], and Sadanaga et al [17]. Our setup is similar to the configuration developed by Sadanaga et al [17]. Due to the complexity of the chain reactions, an important issue in the PERCA method is to address potential backgrounds and interferences from other atmospheric species [10, 12, 13].

Ambient  $\text{NO}_2$  sets the background level of  $\text{NO}_2$ . Ambient ozone is converted to  $\text{NO}_2$  in the flow reactor by the excess amount of  $\text{NO}$ , which also contributes to the background level of  $\text{NO}_2$ . Furthermore, other ambient species such as peroxyacetyl nitrate ( $\text{CH}_3\text{C}(\text{O})\text{O}_2\text{NO}_2$ , PAN) and peroxy nitric acid ( $\text{HO}_2\text{NO}_2$ , PNA) may cause interferences, as they could decompose and generate  $\text{NO}_2$  and peroxy radicals, which can be subsequently involved in the chain reactions in PERCA and cause amplified  $\text{NO}_2$  signals as interferences [10, 12, 13]. Similar to the previous PERCA experiments, a modulation of the  $\text{NO}_2$  signal is utilized in this work. As shown in Figure 1, the CO reagent gas runs along with the ambient air sample, and the modulation is achieved by employing NO injection along with CO at the ambient air addition point (the upstream configuration) and an alternative NO addition point after a Teflon filter at 2-meter downstream from the ambient air addition point (the downstream configuration). The upstream addition configuration allows for chemical amplification of the peroxy radicals in the reaction length and it also converts ambient ozone to  $\text{NO}_2$ . At the end of the reaction length, the installed Teflon filter terminates all the radicals and their chain reactions in the air stream; [17]

the filter also blocks ambient aerosol particles and thus they would not be an interference in the experiment. The downstream addition configuration, which is after the Teflon filter, does not have the chemical amplification, and the ambient ozone is converted to  $\text{NO}_2$  in the extension length (3 m) after the downstream NO addition point. As many kinds of substances from the polluted air, such as CO and  $\text{CH}_3\text{OH}$ , [26] could cause chemical amplifications in the PERCA reactor, NO is added both downstream and upstream in our setup for modulation of the  $\text{NO}_2$  signal. The residence time in the reaction length of the flow reactor (between the upstream and downstream NO addition points) is about 2 sec with a 1000 ml/min flow rate. This short time effectively minimizes thermal decomposition of PAN and PNA and their interferences in the PERCA reactions [10, 12, 13].

For ambient measurements, ambient sample is introduced at a flow rate of 950 ml/min into the flow reactor (Teflon tubing). As shown in the previous studies [17, 18], the Teflon tubing inlet and reactor have good transmission of radicals; our large CL is comparable with those in the previous studies (discussed later), also indicating small radical losses. The tubing inlet is positioned outside of the laboratory window (Riverside, CA). The sampled ambient air is mixed with a small flow of CO at the inlet of the Teflon tubing, outside the window. A tee valve is installed at the NO inlet point to control the NO reagent gas path into either downstream or upstream configuration (Figure 3-1). The amplified  $\text{NO}_2$  in the gas stream is flowed into CRDS for  $\text{NO}_2$  detection. The exhaust from CRDS is passed through a drierite filter

and a hopcalite filter to remove H<sub>2</sub>O and CO, respectively, before entering into the exhaust system.

The experimental conditions of the PERCA reactor (for both ambient measurement and calibration) are listed as follows. (a) A 2-meter long, 6.35-mm o.d., and 4.6-mm i.d. Teflon tubing is used as the flow reactor. A 0.45- $\mu$ m Teflon particle filter is installed at the end of the reaction tubing to completely remove the peroxy radicals and terminate the chain reactions. The total sample flow rate is 1000 ml/min, including both the NO and CO flows. (b) The flow rate of NO (100 ppmv in N<sub>2</sub>, Airgas Inc) is 25 ml/min, giving a NO concentration of 2.5 ppm (vol/vol) in the reaction system. Prior to the flow reactor, the NO gas mixture passes through a FeSO<sub>4</sub> trap to remove a trace amount of NO<sub>2</sub> in the NO gas cylinder [14]. (c) The CO gas passes first through an iodated charcoal filter to remove impurities such as carbonyl complexes in the CO gas cylinder [14]. The flow rate of CO (99.999%, Airgas Inc) for the amplification reactions is 25 ml/min in the ambient measurement and calibration experiment, giving a CO concentration of ~2.5% (vol/vol) in the reaction system. Occasionally, to ensure enough CO is involved in the reaction of calibration where the HO<sub>2</sub> level is higher than the ambient level, larger flow rate of CO (up to 100 ml/min) is used. (d) As temperature and pressure could affect the chain reactions in PERCA, the experiments are carried out at approximately the same temperature (21°C) and 1 atmosphere pressure. After the Teflon filter at the end of the 2-m reaction tubing, the gas mixture is sent to CRDS via a 3-m long Teflon tubing. In this extension length tubing, the ambient ozone that passes through

the Teflon filter is quantitatively converted to NO<sub>2</sub> by the NO + O<sub>3</sub> reaction with the excess amount of NO added at the downstream and upstream configurations (discussed in more detail later).

As the chain reactions can be initiated by the peroxy radicals (HO<sub>2</sub> and RO<sub>2</sub>) or OH and RO radicals, the PERCA method actually measures the total concentrations of RO<sub>x</sub> (HO<sub>2</sub>, RO<sub>2</sub>, OH and RO radicals). However, since the atmospheric concentrations of OH and RO are about 200-1000 times smaller than those of HO<sub>2</sub> + RO<sub>2</sub>, the PERCA technique effectively provides the sum concentrations of HO<sub>2</sub> + RO<sub>2</sub>. Figure 2 shows an example of the ambient measurement for HO<sub>2</sub> + RO<sub>2</sub>. The higher level in the upstream NO addition configuration represents both the amplified NO<sub>2</sub> and background signal (with both NO and CO in the 2-m flow reactor), while the lower level in the downstream configuration is from the unamplified NO<sub>2</sub> background (with only CO added in the 2-m flow reactor). The difference of these two measurements, Δ[NO<sub>2</sub>], removes the interferences and systematic error, giving the amplified concentration of NO<sub>2</sub> due to the HO<sub>2</sub> + RO<sub>2</sub> radicals in the air sample. The HO<sub>2</sub>/RO<sub>2</sub> concentration can then be determined using this difference signal and the chain length CL,  $([HO_2] + [RO_2]) = \Delta[NO_2]/CL$ .

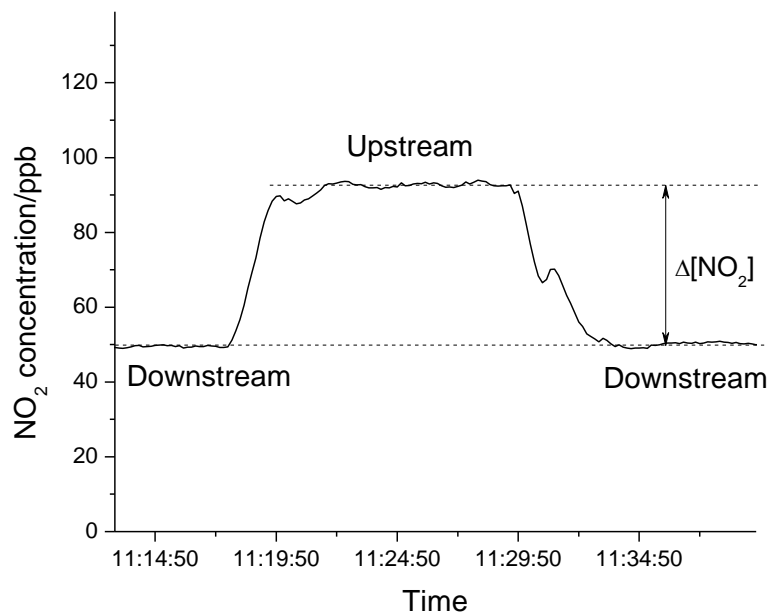


Figure 3- 2 Example of ambient measurement on March 29, 2007.

### 3.2.2 Calibration reaction system

To determine the CL value and calibrate the PERCA system, a HO<sub>2</sub> radical source that is based on thermal decomposition of H<sub>2</sub>O<sub>2</sub> is constructed. Figure 3-3 shows the experimental setup for the calibration measurement.

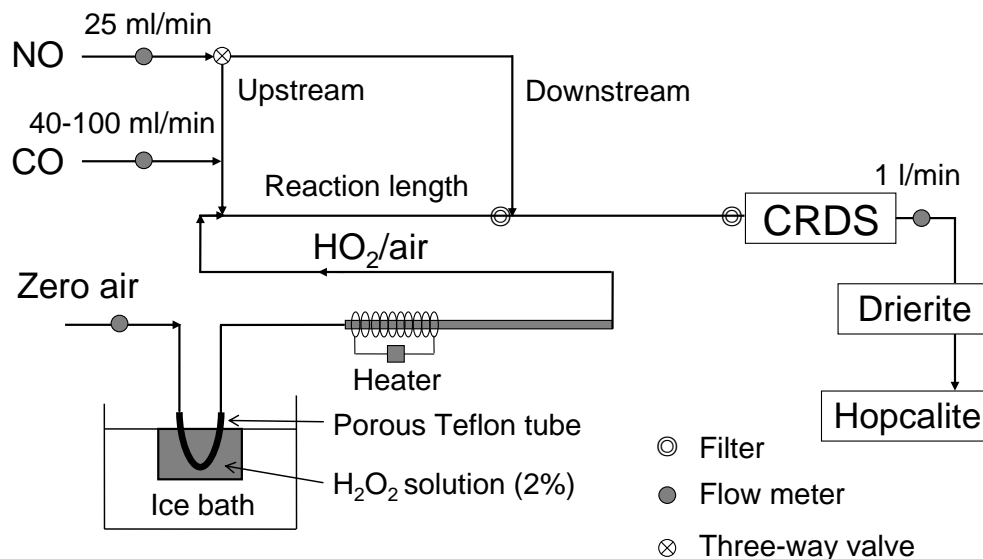


Figure 3- 3 Schematic diagram of the HO<sub>2</sub> calibration system.

The main part of the calibration setup is the same as for the ambient measurement. The difference is that a HO<sub>2</sub> radical source in zero air is introduced into the system instead of the ambient air. The HO<sub>2</sub> radicals are generated by thermal decomposition of H<sub>2</sub>O<sub>2</sub> that permeates through a porous Teflon tube immersed in a diluted H<sub>2</sub>O<sub>2</sub> solution. The H<sub>2</sub>O<sub>2</sub> source is similar to that reported by Tanner and co-workers[27]. The porous Teflon tubing (Gore-tex, 6.0 mm o.d., 50% porosity, W. L. Gore and Associates) is 8 cm long and immersed in the aqueous solution of H<sub>2</sub>O<sub>2</sub> (2% vol/vol) in a 260 cm<sup>3</sup> brown glass bottle, which is kept in a 0°C ice-water bath. The HO<sub>2</sub> generation method by thermal decomposition of H<sub>2</sub>O<sub>2</sub> vapor is based on a previous method developed by Cantrell and co-workers[10], in which the HO<sub>2</sub> radicals were generated from decomposition of H<sub>2</sub>O<sub>2</sub> in air flowing over a resistively heated tungsten wire. In our setup, zero air is passed through the Teflon tubing as a



carrier stream for H<sub>2</sub>O<sub>2</sub> vapor and then enters a heater (a quartz tubing of 75 cm length and 6.4 mm o.d., with its 19-cm middle section wrapped with a heating tape). The heating power is controlled by a Variac transformer to 125 V, and heats the quartz tubing to 600°C (monitored by a type K thermocouple). Production of the HO<sub>2</sub> radicals involves the reactions H<sub>2</sub>O<sub>2</sub> → 2OH and OH + H<sub>2</sub>O<sub>2</sub> → HO<sub>2</sub> + H<sub>2</sub>O. With this method, a flow source of 0.5-3 ppbv HO<sub>2</sub> radicals can be generated.

In order for the chemical amplifier to function as a viable instrument for the measurement of atmospheric peroxy radicals, the number of NO<sub>2</sub> molecules produced per peroxy radical, i.e., the chain length CL, must be determined accurately. This number is dependent on many factors such as the rates of reactions, removal processes of the radicals, and the reaction time. Under the specified conditions, the sensitivity of the system to peroxy radicals can be assessed quantitatively. Therefore, the first important part in this project is to calibrate and obtain a reasonable CL.

To determine the CL value, HO<sub>2</sub> concentration from the HO<sub>2</sub> radical source is measured first in the form of NO<sub>2</sub> after conversion of HO<sub>2</sub> to NO<sub>2</sub> via reaction with NO (eqn. (3-1)), without amplification. Specifically, zero air is used to replace CO to obtain the difference of the upstream and downstream configurations, which corresponds to the concentration of HO<sub>2</sub> without amplification. The HO<sub>2</sub> radicals from the calibration source are then amplified by the chain reactions described above, and the increased NO<sub>2</sub> level is measured. As the calibration HO<sub>2</sub> concentration is much higher than the ambient level, more CO is required. Therefore,

the flow rate of CO is increased to 40-100 ml/min for calibration of PERCA using the HO<sub>2</sub> radical source. The amplification factor CL is determined from the ratio:

$$CL = \Delta[\text{NO}_2]/([\text{HO}_2] + [\text{RO}_2]) \quad (3-10)$$

In our experiment, five measurements on NO<sub>2</sub> are carried out to obtain the CL and instrumental sensitivity to HO<sub>2</sub>. These five signals are shown in the schematics of the calibration processes in Figure 3-2. S<sub>1</sub> is the background level from zero air. S<sub>2</sub> is the CRDS reading for the downstream configuration with only NO and calibration air (HO<sub>2</sub>) in the reactor; this corresponds to the background NO<sub>2</sub> impurity in the NO reagent gas and the zero sample gas, with HO<sub>2</sub> removed by the Teflon filter at the end of the 2-m flow reactor tubing. S'<sub>2</sub> is the NO<sub>2</sub> signal of the upstream configuration with only NO and calibration air (HO<sub>2</sub>) in the reactor, in which HO<sub>2</sub> is converted to NO<sub>2</sub> (without amplification) by reaction with NO in the flow system. S<sub>3</sub> is the signal of the downstream configuration with NO, CO, and calibration air (HO<sub>2</sub>) in the reactor; this corresponds to the background NO<sub>2</sub> level without amplification, as HO<sub>2</sub> is removed by the filter at the end of the flow system. S'<sub>3</sub> is the signal in the upstream configuration with NO, CO and calibration air (HO<sub>2</sub>) in the reactor (with amplification). The difference signal, (S'<sub>2</sub>-S<sub>2</sub>), is from the NO<sub>2</sub> that is converted from the HO<sub>2</sub> radicals in the source; as the HO<sub>2</sub> radicals can be quantitatively converted to NO<sub>2</sub> in the excess amount of NO, this difference signal is effectively equal to the HO<sub>2</sub> concentration. Therefore the output of the HO<sub>2</sub> radical source is determined from these two measurements (S'<sub>2</sub>-S<sub>2</sub>); the concentration of HO<sub>2</sub> in the flow source is found to be in the range of 0.5-3 ppbv. (S'<sub>3</sub>-S<sub>3</sub>) is the

amplified NO<sub>2</sub> signal from the HO<sub>2</sub> radicals in the radical source. The ratio between the amplified signal and the radical concentration gives the chain length of the chemical amplifier:

$$\Delta[\text{NO}_2]/[\text{HO}_2] = (\text{S}'_3 - \text{S}_3)/(\text{S}'_2 - \text{S}_2) = \text{CL} \quad (3-11)$$

In the calibration processes, optimized signals require a stable zero-air baseline (S<sub>1</sub>), and the difference between S<sub>2</sub> and S'<sub>2</sub> need to be measured accurately because it is small. With the high sensitivity of CRDS for NO<sub>2</sub> detection (<1 ppbv), a reliable (S'<sub>2</sub>-S<sub>2</sub>) can be readily obtained.

Figure 3-5 shows an example of the experimental calibration data. The evidence of PERCA, (S'<sub>3</sub>-S<sub>3</sub>), is quite pronounced. After several repeated measurements, the chain length is determined to be 150 with a 90% confidence interval of 50, CL = 150±50. Our CL value is close to the value of 190 reported by Sadanaga et al. using a similar PERCA flow system [17].

Our CL is obtained with low concentration of HO<sub>2</sub> of ~ 0.5 ppb, close to the measured ambient level. It was shown that at higher concentration of HO<sub>2</sub> (>10<sup>11</sup> cm<sup>-3</sup>), the CL may be significantly reduced [12]. However, the large CL observed in this study indicates that the HO<sub>2</sub> radical concentration is reasonably low, and the derived CL could be used for ambient measurements.

- S<sub>3</sub>'** Signal of upstream - NO, CO and calibration air (HO<sub>2</sub>) in flow reactor, with amplification
- S<sub>3</sub>** Signal of downstream - NO, CO and calibration air (HO<sub>2</sub>) in flow reactor
- S<sub>2</sub>'** Signal of upstream - NO and calibration air (HO<sub>2</sub>) in flow reactor
- S<sub>2</sub>** Signal of downstream - NO and calibration air (HO<sub>2</sub>) in flow reactor
- S<sub>1</sub>** Zero air

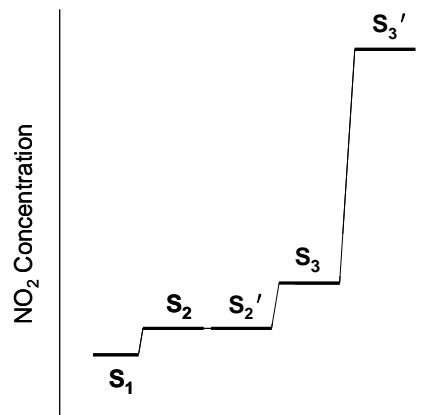


Figure 3- 4 Schematics of calibration model

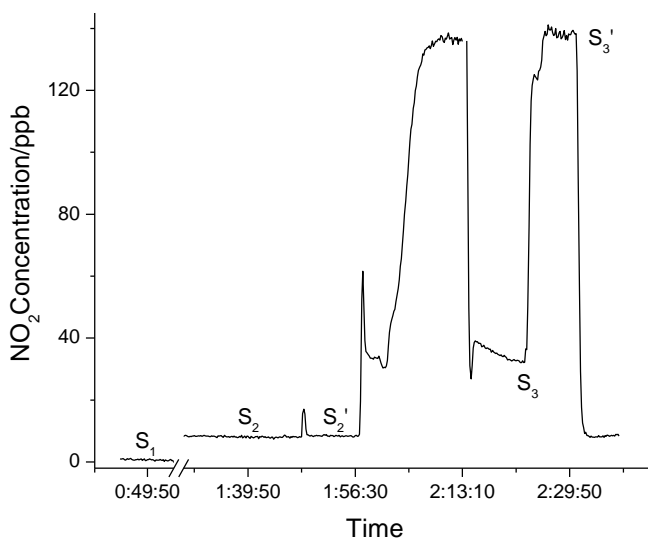


Figure 3- 5 Experimental calibration data

The CL for the RO<sub>2</sub> radicals is slightly different from that of HO<sub>2</sub>, as the RO<sub>2</sub> radicals are converted to HO<sub>2</sub> via reactions with NO and O<sub>2</sub> with an efficiency that

depends upon the structures of RO<sub>2</sub> and the intermediate RO radicals. Cantrell and co-workers discussed the factors that control the efficiency with which the RO<sub>2</sub> radicals are converted into the HO<sub>2</sub> radicals [10, 28, 29]. Those factors include (1) branching ratio for RO<sub>2</sub> + NO → RO + NO<sub>2</sub> relative to RO<sub>2</sub> + NO → RONO<sub>2</sub>; (2) competition of the reactions of the alkoxy radicals with oxygen (in the PERCA chain reactions) and with NO (removal of the RO radicals from the PERCA reactions); and (3) removal of the alkoxy radicals from PERCA due to their unimolecular decomposition or isomerization to hydroxyl substituted radicals [28, 29]. The different efficiencies of converting the RO<sub>2</sub> radicals to HO<sub>2</sub> could be related to their different numbers of carbon atoms and reactivities that depend on temperature, pressure and NO concentration. In the calculations by Cantrell and co-workers [10, 28], it was shown that in clean to moderately polluted atmospheres the conversion efficiencies of selected peroxy radicals to HO<sub>2</sub> in the chemical amplifier are about 0.9. This indicates that the CL's of the RO<sub>2</sub> radicals could be assumed to be about 90% of that of HO<sub>2</sub>.

In the calibration process in this work, [RO<sub>2</sub>] is assumed to be zero in the HO<sub>2</sub> calibration source. The chain length is determined to be 150±50 (90% confidence limit) Our CL value is close to that of 190 by Sadanaga et al. using a similar PERCA flow system [17]. With the determination of CL, the detection sensitivity of the PERCA method to peroxy radicals can be assessed quantitatively.

### 3.2.3 CRDS instrument setup

The CRDS instrument used for the NO<sub>2</sub> measurements has been described before [24, 25]. CRDS is an absorption technique based on measurement of light decay rate rather than light attenuation. CRDS has a long effective absorption length (>km) that leads to high sensitivity [22-25]. In a typical CRDS setup, laser pulses are trapped in an optical cavity composed of two high-quality mirrors (with typical reflectivity R>99.9 %). The intensity of the trapped laser pulses decreases by a very small percentage in each round trip within an empty cavity due to mirror loss and light scattering, decaying as an exponential function of time (with a decay constant, ring-down time  $\tau_0$ ). When an absorbing sample is present in the cavity, its absorbance will increase the loss, which can be determined from comparing the empty cavity ring-down time ( $\tau_0$ ) and the one with the analyte ( $\tau$ ) [22-25]:

$$\alpha = \frac{L}{cl_s} \left( \frac{1}{\tau} - \frac{1}{\tau_0} \right) = \sigma N \quad (3-12)$$

where  $\alpha$  is the absorption coefficient,  $c$  is the speed of light,  $L$  is the cavity length, and  $l_s$  is the sample path length;  $\sigma$  and  $N$  are the absorption cross sections and number density of the analyte. CRDS has the advantage of being insensitive to variations in laser intensity. It is a rapid, real-time technique, with individual ring-down events on the millisecond time scale. Another advantage is that the absorbing analyte can be selectively removed from the sample stream, and it becomes possible to obtain a measure of the concentration without any calibration

gasses. Our group has utilized CRDS for ambient measurements of NO<sub>2</sub> and demonstrated a limit of detection of 150 pptv/10s (S/N=3) [25].

The CRDS measurements of NO<sub>2</sub> are carried out at ~405.23 nm near its peak absorption. As described before [25], the 532-nm output from a Nd:YAG laser pumps a dye laser to produce radiation near 810 nm, which is then doubled to ~405 nm. The 405-nm laser radiation enters the cavity ring-down chamber (0.90 m in length) and the output light is detected by a photomultiplier. The cavity mirrors are separated by 0.90 m and have a reflectivity of ~99.985% at 405 nm (Research Electro-Optics, diameter = 20 mm, and ROC = 1 m). The typical ring-down time for a cavity filled with zero air is 15 μs. The ring-down signal is collected on a 14-bit 200 MS/s oscilloscope card (Gage); each ring-down curve is fitted with a fast algorithm in combination with the data collection software on National Instruments Labview [25]. The gas flow from the PERCA reactor enters in the ring-down cavity after passing through a 0.45-μm particle filter [25]. Buffer gas is not required to protect the mirror surfaces since the air sample is sufficiently filtered, and thus the air sample filled the entire optical path ( $L=l_s$ ). After removing the background and interferences signals, NO<sub>2</sub> measurements with a limit of detection of 150 pptv/10s (S/N=3) can be achieved [25]. Reliable NO<sub>2</sub> measurements could be obtained by this method without the need for frequent calibration with a calibration gas [25].

## **3.3 Results and discussion**

### **3.3.1 Ambient measurements**

Ambient measurements of the peroxy radicals were carried out from March to October 2007 outside our laboratory building at the University of California, Riverside, which is about 4 miles east of downtown Riverside and 60 miles east of Los Angeles. The ambient air sample was drawn in through the Teflon tubing positioned outside the laboratory and immediately into the PERCA reactor. As the free radicals are easily destroyed by surface reactions, no trap or filter was employed for the ambient air before it entered the reaction inlet. The operating conditions of the PERCA and CRDS instruments are described in the experimental section. The CRDS measurements were taken every 10 sec by averaging 100 ring-down decay rates.



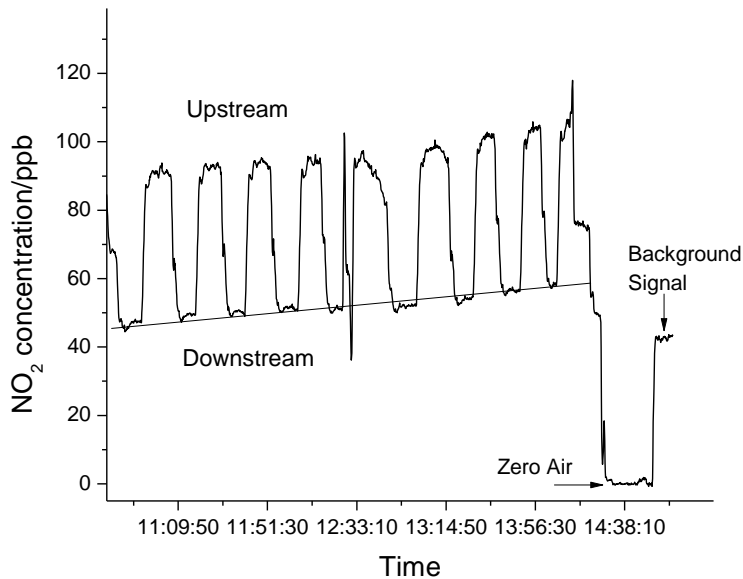


Figure 3- 6 A typical ambient air measurement (March 29, 2007)

In Figure 3-6, the zero-air signal level is chosen as the zero concentration. The NO<sub>2</sub> signal level for the ambient air sample only, without addition of NO and CO in the flow reactor, is mostly due to the ambient NO<sub>2</sub> (as the aerosol is removed by the filter before the ringdown cavity) [25], and is indicated as the background signal in Figure 3-6. The ambient NO<sub>2</sub> concentration is the difference of this background signal and the zero air level [25]. The PERCA-CRDS measurements are periodically switched from the upstream NO injection configuration (the higher levels) to the downstream NO injection configuration (the lower levels). The difference between the downstream signal and the background signal is due to the ambient ozone (which reacts with NO to produce NO<sub>2</sub>, as discussed in the following); thus the

ozone level is also accounted for as the background interference. For the example in Figure 3-3, the baseline of the downstream configuration indicates that the background signal level (both ambient NO<sub>2</sub> and O<sub>3</sub>) increased slowly, but it was shown to be reasonably stable for a period of 12 hours in this study.

The NO<sub>2</sub> measurement by CRDS has demonstrated a detection limit of 150 ppt/10s (3 $\sigma$ ) in our group's previous work [25]. As the measurements of the peroxy radicals are derived from the difference of NO<sub>2</sub> levels in the upstream and downstream configurations, the detection sensitivity of PERCA-CRDS depends on the noise in both the upstream and downstream NO<sub>2</sub> measurements and the fluctuations of the ambient NO<sub>2</sub> and O<sub>3</sub> levels, in addition to the variation of CL. The noises in the NO<sub>2</sub> measurements and the detection sensitivity of HO<sub>2</sub>/RO<sub>2</sub> are analyzed for both the calibration and ambient measurements. In the calibration measurement using the HO<sub>2</sub> source, there are no contributions from the ambient NO<sub>2</sub> and O<sub>3</sub>; the detection sensitivity is estimated to be 10 pptv/60 s (3 $\sigma$ , combined uncertainty from the upstream and downstream NO<sub>2</sub> measurements). The ambient measurements such as those in Figure 3-6 are also analyzed; in this case, the noises and fluctuations due to the ambient NO<sub>2</sub> and O<sub>3</sub> are modest (as the modulation takes place in a short period of a few minutes and the average values of upstream and downstream are used for each modulation), and the detection sensitivity of PERCA-CRDS is also ~10 pptv/60 s (3 $\sigma$ ) in this ambient study.

### 3.3.2 Ozone background

The difference between the downstream and the background NO<sub>2</sub> signal is mainly from the ozone background. The ambient ozone can react with the high-level NO in the PERCA reactor to produce NO<sub>2</sub>,  $O_3 + NO \rightarrow NO_2 + O_2$  ( $k = 1.84 \times 10^{-14}$  cm<sup>3</sup>/molecules s). In both the upstream and downstream configurations, the ozone contributions are the same, as both have the same ambient air and the NO + O<sub>3</sub> reaction is not part of the chemical amplification. Essentially, ozone could be considered as background interference and does not affect the measurements of the RO<sub>x</sub> radicals, since  $\Delta[NO_2]$  removes the ozone interference. However, to ensure the same concentrations of NO<sub>2</sub> from the ozone reactions in both the upstream and downstream configurations, the ambient ozone should react completely, which requires a sufficient amount of reaction time. For an example of 50 ppbv ambient ozone, with a flow rate of 4 l/min (corresponding to the shortest reaction time) and a reaction length of 5 m (2-m PERCA flow reactor + 3-m extension tubing to CRDS) for the upstream configuration or 3 m for the downstream configuration, 99% of the ozone should react with the controlling NO concentration of 2.5 ppmv. The total flow rate of 1 l/min in this study allows sufficient time for the ambient ozone to be completely converted to NO<sub>2</sub> in both the upstream and downstream configurations. Indeed, the NO<sub>2</sub> level due to the ambient ozone contribution, which is the difference NO<sub>2</sub> signals between the ambient air with NO addition and the ambient air only, are shown to be the same in both the upstream and downstream NO injection configurations. This indicates that the ambient ozone passes through the Teflon filter

at the end of the 2-m flow reactor and is quantitatively converted to NO<sub>2</sub> in both configurations. Overall, the background interference from the ambient ozone is effectively accounted for and removed by the upstream and downstream modulation in the PERCA experiment.

### **3.3.3 Ambient measurements of RO<sub>x</sub> in Riverside, CA**

Our sample point was located outside window of our lab, which was in the shadow and faced a street. A parking lot is ~100 meter away from the point. As a result, the NO and NO<sub>2</sub> concentrations were high and fluctuated rapidly. Based on our data, the NO<sub>2</sub> level is from 5 ppbv to more than 40 ppbv; according to the available online NO measurements (using chemiluminescence analyzer) taken by the California Air Resources Board at Mount Rubideaux approximately 6 km to the west, the NO level fluctuated from 10 ppbv to more than 120 ppbv.

The ambient measurements have been carried out from March to October 2007. Figure 3-7 shows the HO<sub>2</sub> + RO<sub>2</sub> concentrations measured in different time, days, and months during this period. The HO<sub>2</sub> + RO<sub>2</sub> level generally is below 0.1 ppb; the afternoon time typically corresponds to higher concentrations of HO<sub>2</sub> + RO<sub>2</sub>. The weather during March to October was quite changeable. In general, the wind flows western to eastern in spring and summer, which transfers pollutants from Los Angeles area, and flows in the opposite direction in autumn and winter, which dilutes the pollution with the air of the inland desert. The concentration of HO<sub>2</sub> +

RO<sub>2</sub> is also related with its chemistry, as well as the temperature, intensity and time of sunshine, and humidity. Interestingly, the highest level of HO<sub>2</sub> + RO<sub>2</sub> was observed on October 26, 2007, when there were widespread wildfires in San Diego, Los Angeles, and Riverside counties. For this day, the PERCA-CRDS experiment ran continuously for 12 hours from 8:00 am to 8:00 pm.

While this work serves to demonstrate the PERCA-CRDS method, the technique can be further improved for future field measurements. For example, dual inlets/channels can be used to replace the upstream and downstream modulation of signals [11, 18, 19]. This will allow real-time subtraction of the background signals from the ambient NO<sub>2</sub> and O<sub>3</sub>, minimizing noises in the PERCA measurements due to fluctuations of the ambient NO<sub>2</sub> and O<sub>3</sub>. It will also enhance the time response for the peroxy radical measurements, as the time response in the current study is largely limited by the switching time between the upstream and downstream NO injection configurations. It is also desirable to carry out cross-comparison studies with other peroxy radical instruments (such as the standard PERCA instrument) in the future. Compact NO<sub>2</sub> analyzers based other variations of CRDS, such as cavity attenuated phase shift spectroscopy (CAPS) [30] and broadband cavity enhanced absorption spectroscopy (BBCEAS) [31], utilize light emitting diodes (LEDs) instead of lasers as the light sources and also provide sensitive detection of NO<sub>2</sub>; they could be readily incorporated in the PERCA-CRDS method, providing much more economical and portable instruments for the peroxy radical measurements.

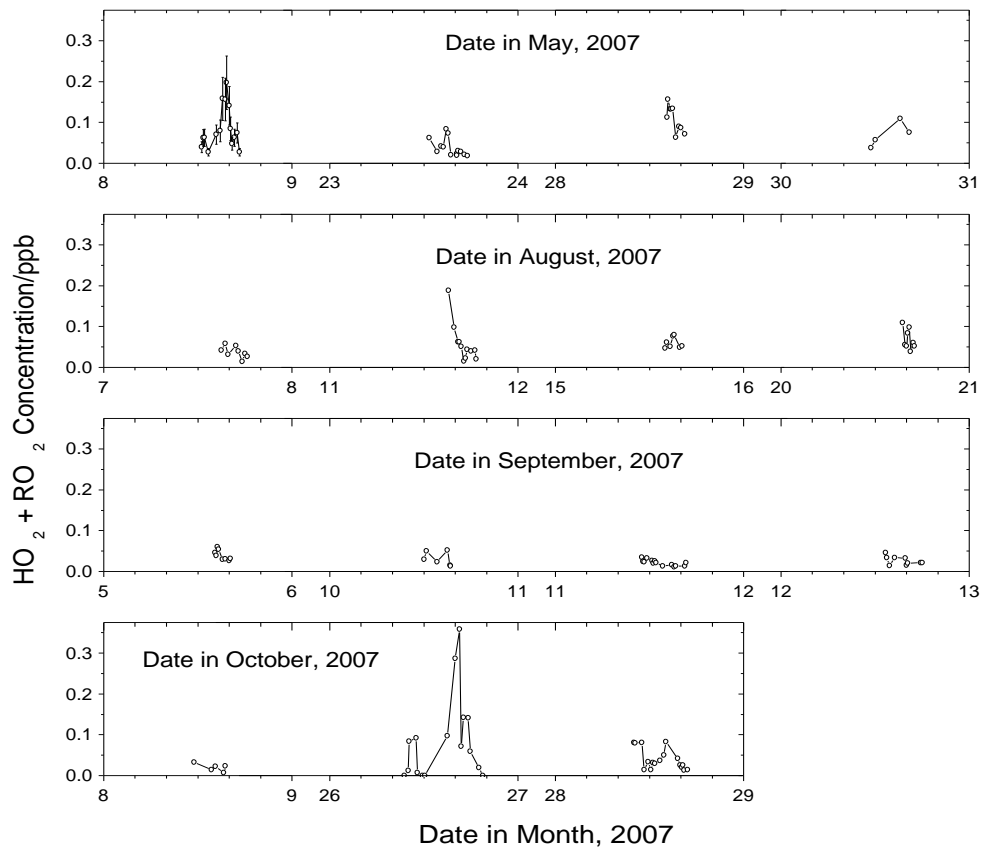


Figure 3- 7 Ambient measurements of HO<sub>2</sub>/RO<sub>2</sub> at different time and days in 2007. The error bars (shown only for May 8, 2007) reflect the uncertainty in CL

## References

1. Finlayson-Pitts, B.J. and J.N.J. Pitts, *Chemistry of the Upper and Lower Atmosphere*. 2000, New York: Academic Press.

2. Mihelcic, D., P. Musgen, and D.H. Ehhalt, *An improved method of measuring tropospheric NO<sub>2</sub> and RO<sub>2</sub> by matrix-isolation and electron-spin-resonance*. Journal of Atmospheric Chemistry, 1985. **3**(3): p. 341-361.
3. Mihelcic, D., et al., *Numerical-analysis of ESR-spectra from atmospheric samples*. Journal of Atmospheric Chemistry, 1990. **11**(3): p. 271-297.
4. Kanaya, Y., et al., *Development of a ground-based LIF instrument for measuring HO<sub>x</sub> radicals: Instrumentation and calibrations*. Journal of Atmospheric Chemistry, 2001. **38**(1): p. 73-110.
5. Creasey, D.J., et al., *Implementation and initial deployment of a field instrument for measurement of OH and HO<sub>2</sub> in the troposphere by laser-induced fluorescence*. Journal of the Chemical Society-Faraday Transactions, 1997. **93**(16): p. 2907-2913.
6. Hard, T.M., et al., *Diurnal HO<sub>2</sub> cycles at clean-air and urban sites in the troposphere*. Journal of Geophysical Research-Atmospheres, 1992. **97**(D9): p. 9785-9794.
7. Stevens, P.S., J.H. Mather, and W.H. Brune, *Measurement of tropospheric OH and HO<sub>2</sub> by laser-induced fluorescence at low-pressure*. Journal of Geophysical Research-Atmospheres, 1994. **99**(D2): p. 3543-3557.
8. Cantrell, C.A. and D.H. Stedman, *A possible technique for the measurement of atmospheric peroxy radicals*. Geophysical Research Letters, 1982. **9**(8): p. 846-849.

9. Cantrell, C.A., D.H. Stedman, and G.J. Wendel, *Measurement of atmospheric peroxy radicals by chemical amplification*. Analytical Chemistry, 1984. **56**(8): p. 1496-1502.
10. Cantrell, C.A., et al., *An improved chemical amplifier technique for peroxy radical measurements*. Journal of Geophysical Research-Atmospheres, 1993. **98**(D2): p. 2897-2909.
11. Cantrell, C.A., R.E. Shetter, and J.G. Calvert, *Dual-inlet chemical amplifier for atmospheric peroxy radical measurements*. Analytical Chemistry, 1996. **68**(23): p. 4194-4199.
12. Hastie, D.R., et al., *Calibrated chemical amplifier for atmospheric RO<sub>x</sub> measurements*. Analytical Chemistry, 1991. **63**(18): p. 2048-2057.
13. Hu, J. and D.H. Stedman, *Free radical detector for tropospheric measurement using chemical amplification*. Analytical Chemistry, 1994. **66**(20): p. 3384-3393.
14. Clemitshaw, K.C., et al., *A calibrated peroxy radical chemical amplifier for ground-based tropospheric measurements*. Journal of Geophysical Research-Atmospheres, 1997. **102**(D21): p. 25405-25416.
15. Burkert, J., et al., *Peroxy radical and related trace gas measurements in the boundary layer above the Atlantic Ocean*. Journal of Geophysical Research-Atmospheres, 2001. **106**(D6): p. 5457-5477.



16. Mihele, C.M. and D.R. Hastie, *Optimized operation and calibration procedures for radical amplifier-type detectors*. Journal of Atmospheric and Oceanic Technology, 2000. **17**(6): p. 788-794.
17. Sadanaga, Y., et al., *Development of a measurement system of peroxy radicals using a chemical amplification/laser-induced fluorescence technique*. Review of Scientific Instruments, 2004. **75**(4): p. 864-872.
18. Green, T.J., et al., *Airborne measurements of peroxy radicals using the PERCA technique*. Journal of Environmental Monitoring, 2003. **5**(1): p. 75-83.
19. Green, T.J., et al., *An improved dual channel PERCA instrument for atmospheric measurements of peroxy radicals*. Journal of Environmental Monitoring, 2006. **8**(5): p. 530-536.
20. Reiner, T. and F. Arnold, *Stratospheric SO<sub>3</sub>: Upper limits inferred from ion composition measurements - Implications for H<sub>2</sub>SO<sub>4</sub> and aerosol formation*. Geophysical Research Letters, 1997. **24**(14): p. 1751-1754.
21. Cantrell, C.A., et al., *Peroxy radical observations using chemical ionization mass spectrometry during TOPSE*. Journal of Geophysical Research-Atmospheres, 2003. **108**(D6): p. 14.
22. O'Keefe, A. and D.A.G. Deacon, *Cavity ring-down optical spectrometer for absorption measurements using pulsed laser sources*. Review of Scientific Instruments, 1988. **59**(12): p. 2544-2551.
23. Wheeler, M.D., et al., *Cavity ring-down spectroscopy*. Journal of the Chemical Society-Faraday Transactions, 1998. **94**(3): p. 337-351.

24. Wang, L.M. and J.S. Zhang, *Detection of nitrous acid by cavity ring down spectroscopy*. Environmental Science & Technology, 2000. **34**(19): p. 4221-4227.
25. Hargrove, J., et al., *Cavity ring-down spectroscopy of ambient NO<sub>2</sub> with quantification and elimination of interferences*. Environ. Sci. Technol., 2006. **40**(24): p. 7868-7873.
26. Nadadur, S.S., et al., *The complexities of air pollution regulation: The need for an integrated research and regulatory perspective*. Toxicological Sciences, 2007. **100**(2): p. 318-327.
27. Tanner, R.L., et al., *Sampling and determination of gas-phase hydrogen peroxide following removal of ozone by gas-phase reaction with nitric oxide*. Analytical Chemistry, 1986. **58**(8): p. 1857-1865.
28. Cantrell, C.A., et al., *Measurement methods for peroxy radicals in the atmosphere*. Advances in Chemistry Series, 1993(232): p. 291-322.
29. Madronich, S. and J.G. Calvert, *Permutation reactions of organic peroxy-radicals in the troposphere*. Journal of Geophysical Research-Atmospheres, 1990. **95**(D5): p. 5697-5715.
30. Keabian, P.L., S.C. Herndon, and A. Freedman, *Detection of nitrogen dioxide by cavity attenuated phase shift spectroscopy*. Analytical Chemistry, 2005. **77**(2): p. 724-728.
31. Langridge, J.M., S.M. Ball, and R.L. Jones, *A compact broadband cavity enhanced absorption spectrometer for detection of atmospheric NO<sub>2</sub> using light emitting diodes*. Analyst, 2006. **131**(8): p. 916-922.

# **Chapter 4 An improved dual channel Peroxy radicals Chemical Amplification measurement using diode laser based cavity ring down spectroscopy**

## **Abstract**

Peroxy radicals (hydroperoxy HO<sub>2</sub> and organic peroxy RO<sub>2</sub>) are important intermediates in the photo oxidation processes of the troposphere. It is challenging to accurately measure the trace and reactive tropospheric peroxy radicals, especially in situ and in real time. An improved dual channel peroxy radical chemical amplification (PERCA) instrument using diode laser cavity ring down spectroscopy (CRDS) is developed in this work for measurements of the peroxy radicals. The sample air is sampled into two channels – an amplification channel and a reference channel. In the amplification channel, HO<sub>2</sub> and RO<sub>2</sub> are first converted to NO<sub>2</sub> via reactions with an excess amount of NO, and the OH and RO coproducts are recycled back to HO<sub>2</sub> in subsequent reactions with CO and O<sub>2</sub>; the chain reactions of HO<sub>2</sub> are repeated and amplify the level of NO<sub>2</sub>. The reference channel is for the background NO<sub>2</sub> and O<sub>3</sub> converted to NO<sub>2</sub> by reaction with NO. NO<sub>2</sub> concentrations from both channels are monitored simultaneously by two diode laser based CRDS systems at 408.5 nm. The converted NO<sub>2</sub> of RO<sub>x</sub> concentration is determined as the difference between the amplification and the reference channels. The amplification factor or

chain length (CL) for this PERCA-dual CRDS system is 180, which was calibrated using laboratory generated HO<sub>2</sub> radical and CH<sub>3</sub>O<sub>2</sub> radicals and the optimized condition under different conditions is characterized and discussed. The detective sensitivity is shown to be ~12ppt/10s (1σ) for peroxy radicals. This instrument has fast time response and is less sensitive to fluctuations in ambient conditions than the earlier single-channel version, as the background and background plus radical signals are continuously monitored. The instrument has been applied in ambient studies of Riverside, California in 2011.

## 4.1. Introduction

The Peroxy radicals (HO<sub>2</sub> and RO<sub>2</sub>) play critical roles in atmospheric chemistry. In the polluted atmosphere loaded with hydrocarbon [1], HO<sub>2</sub> and RO<sub>2</sub> radicals are intermediate species generated during the oxidative conversion of RH. HO<sub>2</sub> may also be formed following HCHO photolysis and from the reaction of alkenes with ozone. The reactions of HO<sub>2</sub> with itself and other organic peroxy radicals are important to shape the atmospheric makeup, especially in clean troposphere. It is therefore critical to accurately measure the concentrations of the HO<sub>2</sub>/RO<sub>2</sub> radicals in the ambient atmosphere in order to understand their contribution to the air pollution, since atmospheric modeling requires HO<sub>2</sub>/RO<sub>2</sub> abundance to predict the atmospheric composition and to forecast air quality.

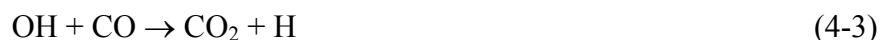
The peroxy radicals are highly reactive and therefore the concentrations are very low in the ambient atmosphere. As a result, monitoring the peroxy radicals with high sensitivity

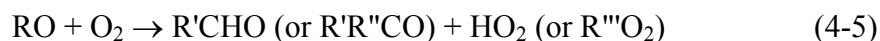
and selectivity *in situ* is a great challenge. . In the last two decades, there have been many efforts and attempts in previous studies, however, most of them have limitations.. The matrix isolation and electron spin resonance (MI-ESR) method requires a long sample accumulation time of approximately 30 min to achieve sufficient sensitivity, which is about 5 ppt [2]. Laser-induced fluorescence (LIF) [3, 4] method is complex and requires careful calibrations. And it requires low pressure which might get interferences from decomposition [5-7]. Peroxy radical chemical amplification (PERCA) coupled with luminol detection is subject to interferences [8]. Despite two decades of work, it is clear that more studies are required, particularly for simultaneous monitoring HO<sub>2</sub> and RO<sub>2</sub> with high sensitivity and precision.

In the PERCA method, HO<sub>2</sub> and RO<sub>2</sub> convert to NO<sub>2</sub> via reactions with an excess amount of NO, with subsequent reactions to recycle most of the OH and RO co-products back to HO<sub>2</sub> by reactions with an excess amount of CO, and amplify the level of NO<sub>2</sub> [9-11]. In the PERCA chain reactions, HO<sub>2</sub> and RO<sub>2</sub> radicals in the air sample react with NO first to produce OH and RO plus NO<sub>2</sub> in the initial steps as follows [12]:



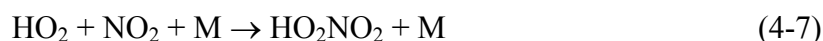
When in an environment of a great concentration of CO and O<sub>2</sub>, the chain reactions involving HO<sub>2</sub> can continue and bring back HO<sub>2</sub> to the initial steps, and the RO radical—produced in eqn. (4-2)—reacts with O<sub>2</sub> to form HO<sub>2</sub> or RO<sub>2</sub>, which could return to the initial steps too[13]:





By these reactions and cycles with NO, CO and O<sub>2</sub>, peroxy radicals (RO<sub>2</sub> + HO<sub>2</sub>) can increase the level of NO<sub>2</sub> by hundreds of times. The amplified NO<sub>2</sub> is then detected by a NO<sub>2</sub> analyzer, indirectly providing information of the concentrations of peroxy radicals

The level of amplification and thus the sensitivity of PERCA are limited by radical removal processes from the system. The following are the chain termination reactions of HO<sub>2</sub>:



As the chain reactions can be initiated by peroxy radicals (HO<sub>2</sub> and RO<sub>2</sub>) or OH and RO radicals, the PERCA method actually measures the total concentrations of RO<sub>x</sub> (HO<sub>2</sub>, RO<sub>2</sub>, OH and RO radicals). However, since the atmospheric concentrations of OH and RO are about 200-1000 times smaller than those of HO<sub>2</sub> + RO<sub>2</sub>, the PERCA technique effectively provides the sum concentrations of HO<sub>2</sub> + RO<sub>2</sub>.

To accurately measure the concentrations of RO<sub>2</sub>/HO<sub>2</sub> in the PERCA method, the number of NO<sub>2</sub> molecules produced per peroxy radical, which is called amplification factor or chain length (CL) [9, 11, 14], must be determined. This factor depends on the rates of reactions, concentrations of the reagents, removal processes of radicals from the

system, and other experimental conditions such as flowrates of the reagent gases, reaction time, etc. The typical CL values are in the range of 100-200.[10, 15, 16]

To quantify the role of peroxy radical chemistry in atmospheric chemistry, a sensitive laser absorption technique, cavity ring-down spectroscopy (CRDS), has been utilized in our work. This technique serves in measurements of NO<sub>2</sub> for the PERCA method in a flow-tube sample cell with high sensitivity, interference free and real time response.

To monitor the HO<sub>2</sub> and RO<sub>2</sub> radicals, an improved dual channel PERCA instrument using diode laser CRDS has been developed based on our previous single channel instrument [17], and is applied in ambient studies. The ambient air is sampling into two channels – an amplification channel and a reference channel. In the amplification channel the converted peroxy radicals has been measured using PERCA, while the reference channel is for the background NO<sub>2</sub> and O<sub>3</sub>. NO<sub>2</sub> concentrations from both inlet channels are monitored simultaneously by two diode laser based CRDS systems at 408.5 nm wavelength. This instrument is improved over the single-channel version, as it continuously monitors the background and can minimize the effects of fluctuations in ambient ozone. In addition, it improves the time response and allows the detection of changes in peroxy radical concentrations that are related to the rapid changes in nitric oxide concentrations and ozone photolysis frequency. Furthermore, in this new setup a small blue diode laser is incorporated as the light source, and a portable instrument is constructed for the ambient measurements.

## **4.2 Experimental**

The dual-channel PERCA-CRDS instrument has two major components: [12] two flow-reactors (one for PERCA and another for reference); and (2) two CRDS systems for NO<sub>2</sub> detection channels. A calibration system with HO<sub>2</sub> and RO<sub>2</sub> radical sources in laboratory used to characterize and optimize the CL of PERCA. The ambient measurements were then carried out under the same optimized conditions of the flow reactors.

### **4.2.1 NO<sub>2</sub> detection using CRDS**

CRDS is a technique based on measurement of light decay rate rather than light attenuation [18, 19] which has been described in chapter 2. In this work, a small blue diode laser is used as the light source and a portable instrument is constructed for ambient measurements, which is shown in Figure 4-1.



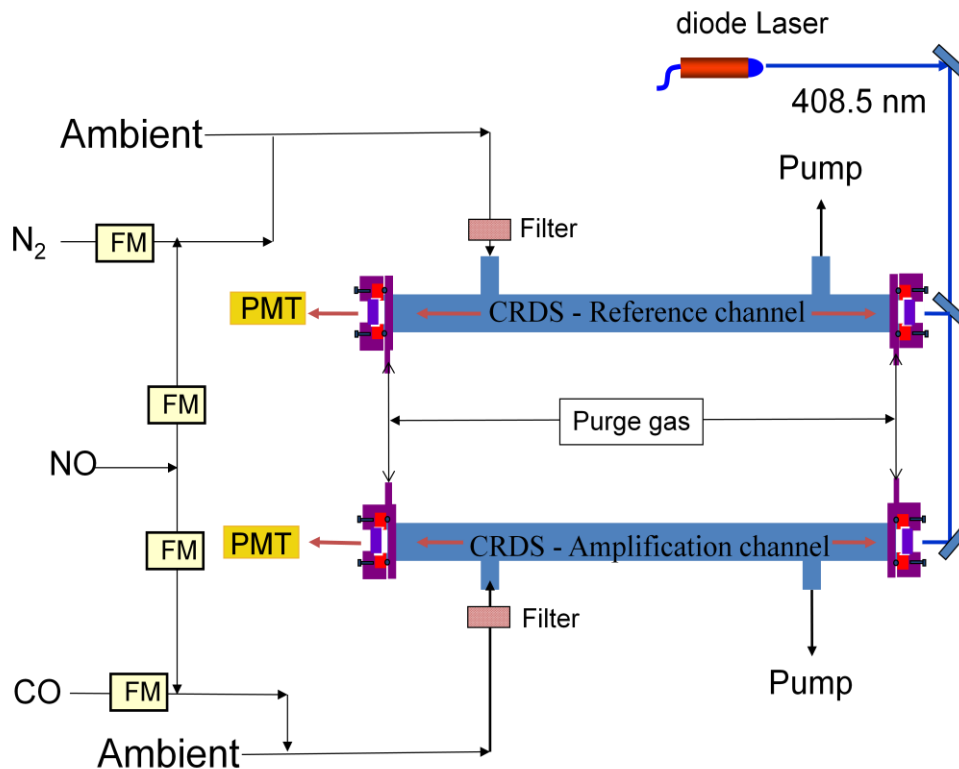


Figure 4- 1 Schematic diagram of the ROx measurements using dual channel PERCA-CRDS.

FM = Flow meter

In this setup, each cavity ringdown cell consisted of a pair of high reflectivity mirrors ( Los Gatos, 2.54 cm diameter, 1 m radius of curvature), with a measured reflectivity of 99.98%. The typical ringdown time constant was approximately 18  $\mu$ s at wavelength of 408.5 nm with the cell filled with ambient pressure zero air. The mirrors were mounted at both end of the 86 cm long cell, with the center 66 cm constructed of 1 inch O.D. glass tube through which the sample air flowed. Small purge flows (~25 sccm of air for each mirror) are introduced directly at the mirrors to maintain their cleanliness. The total cavity length (L) (in eqn (10)) includes the

length over which the absorber is present ( $l_s$ ) and the purge volumes adjacent to the mirrors filled with dry purge gas. The ratio of  $L$  over  $l_s$  has been studied in the pervious works [20] and it has been proved that it is independent of flow rate and in agreement with the measured physical dimensions of the cells. Therefore, here, the total cavity length  $L$  was used as 80 cm and the sample path length  $l_s$  was used as 66cm without further calibration

The sample flow from the common inlet was divided into the two CRDS cells, and enters and exits each sample cell through PFA Teflon fittings. For ambient measurement, the tubing inlet was positioned outside of the laboratory window. The sampling flowrate was maintained at 1 standard liter per min (slpm) for each cell by two orifices connected to an oil-free scroll pump, which was used to pull sample air through the cells. Other flows including NO, CO, zero air and purge gas were measured using mass flow meters (figure 1), and observed concentrations are corrected for the small dilution from the mirror purge gas. Pressure and temperature were measured independently for each cell. Two 0.45 micrometer particle filters were used for each cell for terminated the radicals and removing the particulates in the ambient air stream (thus minimizing particulate Mie scattering) and to prevent possible deposition of particles on the mirror surfaces.

The blue diode laser (Sharp) has an optical output of approximately 20 mW at 408.5nm with a 0.5 nm bandwidth. The laser output is amplitude modulated with a square-wave voltage signal at a repetition of 2 kHz and a duty cycle of 50%. The modulated laser output has a fast rise and falling edge with modulation bandwidth of

1.2 MHz Using a beamsplitter and two turning mirrors, the laser beam is send into two cavity ring down cells. Since the laser is broadband ( $\sim 0.5$  nm), the laser output can be directly coupled into the cavity without any requirements for active matching of the modes of the laser output to the resonant frequencies of the cavity or a scheme to increase the cavity mode density. [21] (Fuchs, H. 2009) When the laser is modulated off, the light intensity in the cavity exponentially decreases.

The light transmitted through the end mirror of each cavity is projected onto a photomultiplier tube module (Hamamatsu). Ring-down transients at a repetition rate of 2 kHz were acquired with a PCI-based transient digitizer (Adlink), co-added, and fit to a single exponential. To achieve this, data collection software has been written in house starting from the Adlink software development kit using National Instruments Labview v.7.1.

$\text{NO}_2$  has strong absorptions in the range of 400-450 nm of visible light with neglect interference of other species [22], and even such interferences are eliminated by using the dual – channel approach. Meanwhile, diode laser of 405-410 nm is available for us to construct such instruments.

#### **4.2.2. Determination of $\text{NO}_2$ cross sections and instrument sensitivity**

To obtain quantitative measurements of  $\text{NO}_2$  concentration, the absorption cross sections of  $\text{NO}_2$  at the center wavelength and within the linewidth of the diode laser need to be evaluated. There are two independent methods to determine the effective  $\text{NO}_2$  cross-section corresponding to the laser wavelength, [12] from intercomparison and

calibration with a NO<sub>x</sub> analyzer and (2) from convolution of the high-resolution literature absorption cross sections of NO<sub>2</sub> using the center wavelength and linewidth of the diode laser.

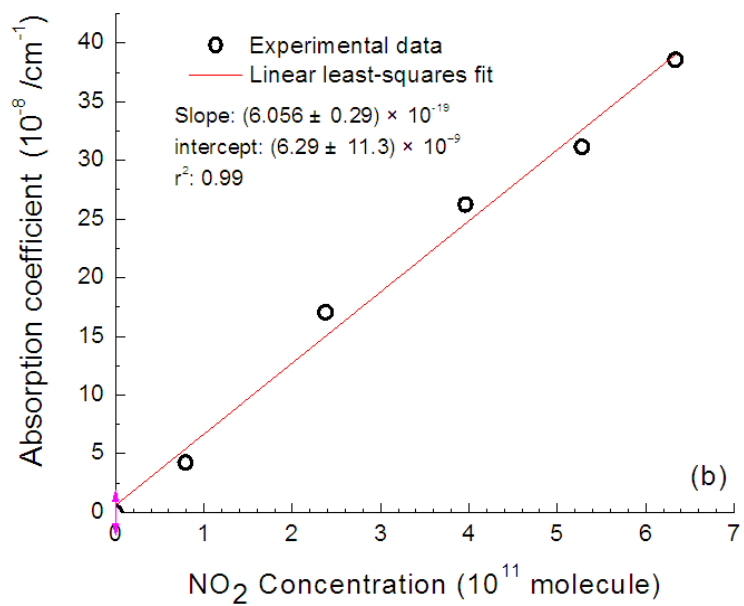
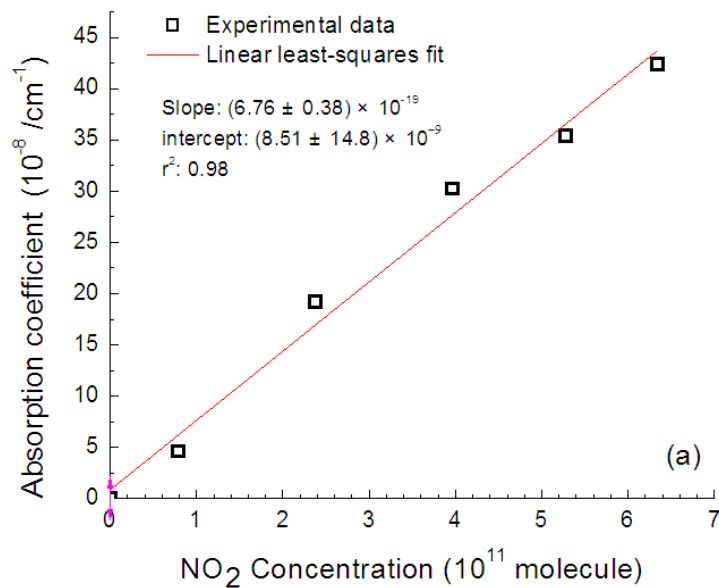


Figure 4- 2 Calibration of NO<sub>2</sub> cross sections from the CRDS and NO<sub>x</sub> analyzer measurement. Absorption coefficient is from CRDS, NO<sub>2</sub> concentration is from NO<sub>x</sub> analyzer measurement. (a) is from reference CRDS cell and (b) is from amplification CRDS cell. 1 ppb =  $2.46 \times 10^{10}$  molecule/cm<sup>3</sup> at 1 atm 25°C.

The comparisons of NO<sub>2</sub> measurements by CRDS and the NO<sub>x</sub> analyzer have been carried out using NO<sub>2</sub> standard mixtures in zero air. In this comparison, the gas samples passed through the CRDS cavity for the CRDS measurements and then entered into the NO<sub>x</sub> analyzer. The absorption cross sections of NO<sub>2</sub> in the CRDS spectrum are obtained using Eqn 10, with the absorption coefficient measured by CRDS and number density  $N$  from the NO<sub>x</sub> analyzer. Figure 2 shows a plot of absorption coefficient from CRDS versus NO<sub>2</sub> concentration using the NO<sub>x</sub> analyzer, whose slope is equal to the NO<sub>2</sub> absorption cross sections. The average effective NO<sub>2</sub> cross-section from the two channels is  $6.41 \times 10^{-19} \text{ cm}^2$ . The two channels has slight differences due to various factors, including drifts in pressure, temperature, purge volume flows, systematic differences and different cavity alignment in the two cavities [23].

In the second approach, using a CCD spectrometer (Andor Shamrock SR-303i, at a resolution of 0.10 nm), the emission spectrum of the diode laser is measured. As show in Figure 3, the diode laser output is centered at 408.48 nm with a fullwidth at half maximum (FWHM) of 0.2 nm. the high resolution NO<sub>2</sub> absorption cross sections by Yoshino et al (Yoshino) are then convoluted with the measure FWHM, giving an effective NO<sub>2</sub> cross sections of  $6.34 \times 10^{-19} \text{ cm}^2/\text{molecule}$

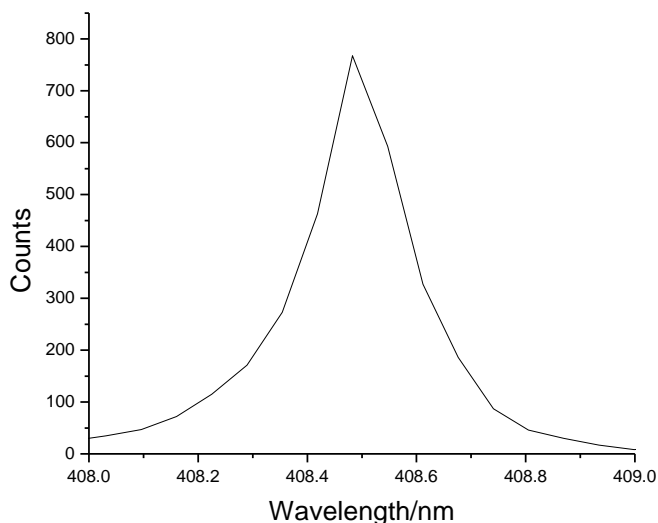


Figure 4- 3. Diode laser emission spectrum

The two calibration methods for effective NO<sub>2</sub> absorption cross section are consistent within approximately 5%. Therefore we used an average effective NO<sub>2</sub> absorption cross section of  $6.375 \times 10^{-19} \text{cm}^2/\text{molecule}$ .

With this NO<sub>2</sub> cross section, at 1 s integration time for one points and with 10 points (10 s), both of the channels can achieve the standard deviation precision of 150 pptv/ 10 s and 160 pptv/ 10 s, respectively, under the laboratory conditions.

#### **4.2.3 Chemical reaction system and ambient measurement setup**

The ambient air is sampled into two CRDS channels – an amplification channel and a reference channel (Figure 1). The amplification channel is composed of a flow reactor to carry out the PERCA chain reactions, similar to our pervious single

channel PERCA CRDS setup [17]. Due to the complexity of the chain reactions, an important issue in the PERCA method is to address potential backgrounds and interferences from other atmospheric species. [11, 14, 16] Ambient  $\text{NO}_2$  sets the background level of  $\text{NO}_2$ .  $\text{O}_3$  in the ambient air is converted to  $\text{NO}_2$  in the flow reactor by the excess amount of  $\text{NO}$ , which increases the background  $\text{NO}_2$  reading. Furthermore, other ambient species such as peroxyacetyl nitrate ( $\text{CH}_3\text{C}(\text{O})\text{O}_2\text{NO}_2$ , PAN) and peroxy nitric acid ( $\text{HO}_2\text{NO}_2$ , PNA) may cause interferences, as they could decompose and generate  $\text{NO}_2$  and peroxy radicals, which could subsequently be involved in the chain reactions in PERCA and cause amplified  $\text{NO}_2$  signals as interferences.[11, 14, 16]. In the dual channels approach, a modulation of the  $\text{NO}_2$  signal is utilized. As shown in Figure 2, the  $\text{NO}$  reagent gas runs along with the ambient air sample all the time in both of the channels, and the modulation is achieved by employing  $\text{CO}$  injection along with  $\text{NO}$  at the ambient air addition point for the amplification channels, while using the same amount of  $\text{N}_2$  to replace  $\text{CO}$  and injecting along with  $\text{NO}$  at the ambient air addition point for the reference channel. The amplification channel configuration allows for chemical amplification of the peroxy radicals in the reaction length and it also converts ambient  $\text{O}_3$  to  $\text{NO}_2$ , while the reference channel is only for the background  $\text{NO}_2$  and  $\text{O}_3$  that is converted to  $\text{NO}_2$  without chemical amplification of the peroxy radicals. At the end of both channels, the installed Teflon filter terminates all the radicals and their chain reactions in the air stream (Figure 1) [10]; the filter also blocks ambient aerosol particles and thus the aerosol particles would not be interference in the experiment.



The residence time in the reaction length of both channels is about 1 sec with the 1000 ml/min flow rate. This short time effectively minimizes thermal decomposition of PAN and PNA and their interferences in the PERCA reactions.[11, 14, 16]

The experimental configurations of the PERCA reactor for ambient measurement are listed as follows. In the amplification channel, the reactor consists (a) a 1-meter long, 6.35-mm o.d., and 4.6-mm i.d. Teflon tubing used as the flow reactor. A 0.45  $\mu\text{m}$  Teflon particle filter is installed at the end of the reaction tubing to completely remove the peroxy radicals and terminate the chain reactions. The total sample flow rate is 1000 ml/min, including both the NO and CO flows. (b) The flow rate of NO (original concentration of 100 ppmv in  $\text{N}_2$ , Airgas Inc) is 25 ml/min, giving a NO concentration of 2.5 ppm (vol/vol) in the reaction system. Prior to the flow reactor, the NO gas mixture passes through a  $\text{FeSO}_4$  trap to remove a trace amount of  $\text{NO}_2$  in the NO gas cylinder.[15] [15] The CO gas passes first through an iodated charcoal filter to remove impurities such as carbonyl complexes in the CO gas cylinder.[15] The flow rate of the pure CO (99.999%, Airgas Inc) for the amplification reactions is around 80 ml/min in the ambient measurement and calibration experiment, giving a CO concentration of ~8% (vol/vol) in the reaction system. (d) As temperature and pressure could affect the chain reactions in PERCA, the experiments are carried out at approximately the same temperature (21°C) and 1 atmosphere pressure. In the reference channel, the configuration is identical to the amplification channel except using pure  $\text{N}_2$  (UHP Airgas) to replace CO gas. For calibration experiment setup, all the flowrates of the gasses and reactor tubing length would be various to optimize

the systems. The exhaust from CRDS, for both ambient measurement and calibration configurations, is passed through a hopcalite filter to remove CO and then goes into a vacuum pump and the exhaust system.

This instrument is less sensitive to fluctuations in ambient ozone than the single-channel version because of the continuous monitoring of the background and background plus radical signals. The converted  $\text{NO}_2$  ( $\Delta[\text{NO}_2]$ ) of  $\text{RO}_x$  concentration is determined as the difference between the amplification and the reference inlet channels. The  $\text{RO}_x$  concentration can then be determined using this difference signal and the chain length CL,  $[\text{RO}_x] = [\text{NO}_2]/\text{CL}$ .

#### **4.2.3 Calibration reaction system**

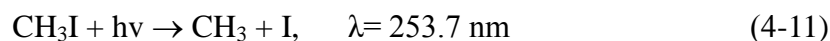
In order for the chemical amplifier to function as a viable instrument for the measurement of atmospheric peroxy radicals, the number of  $\text{NO}_2$  molecules produced per peroxy radical, i.e., the chain length CL, must be determined accurately. This number is dependent on many factors such as the types of peroxy radicals, the rates of reactions, removal processes of the radicals, the concentration of reactants, relative humidity and the reaction time. Under the specified conditions, the sensitivity of the system to peroxy radicals can be assessed quantitatively. Therefore, an important part of this project is to calibrate and obtain a larger CL.

To obtain an optimal value of CL, different radical sources have been test out. Beside the  $\text{HO}_2$  radical source generated from thermal decomposition of  $\text{H}_2\text{O}_2$  vapor (permeated from 2%  $\text{H}_2\text{O}_2$  solution through a porous Teflon tubing) up to  $600^\circ\text{C}$  in

our pervious study [17], photolytical radicals sources of  $\text{CH}_3\text{O}_2$  and  $\text{HO}_2$  are used for calibration of the PERCA method in this work.

The main radical source for calibration in this work is  $\text{CH}_3\text{O}_2$  radical, which was based upon 253.7 nm photolysis of  $\text{CH}_3\text{I}$  in zero air. Mixtures of  $\text{CH}_3\text{I}$ /air were obtained by air bubbling through  $\text{CH}_3\text{I}$  in a liquid nitrogen bath. Under this configuration, the concentration of  $\text{CH}_3\text{I}$  is about 6 ppb in the air mixture. The  $\text{CH}_3\text{I}$ /air mixtures flowed through a 50 cm long 1/4 inch O.D. quartz tubing, which was subject to the UV radiation from an adjacent pen ray low-pressure Hg lamp (UVP). Between the quartz tubing and the pen ray Hg lamp, a quartz curette filled with menthol was installed to filter the UV light shorter than 253.7nm in order to limit the ozone generated by photolysis of oxygen with the 185nm wavelength light.

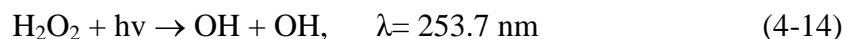
$\text{CH}_3\text{O}_2$  radicals are produced in the quartz tubing upon photolysis of  $\text{CH}_3\text{I}$  in air as follows:



This method can give us a continuous source of  $\text{CH}_3\text{O}_2$  radicals, which was ranging from ~1 ppb to 2 ppb with mostly neglected other byproducts [15]. Concentration of  $\text{CH}_3\text{O}_2$  radicals smaller than 1 ppb can be achieved by dilution with  $\text{N}_2$  adding downstream of the quartz tubing. The radical source outlet was connected to a two-ways valve, with one way was directly coupled to the PERCA

inlet and the other way connected to a Teflon filter first, which eliminated the peroxy radicals, and then to the same PERCA inlet with a tee. Therefore, in the first pathway (radical model), the radicals could undergo the PERCA reactions, while in the second pathway (background mode), all the radicals were removed before entering into the PERCA inlet.

The setup for the HO<sub>2</sub> calibration source was identical to that for CH<sub>3</sub>O<sub>2</sub>. The zero air carrier gas was bubbled through a 60% H<sub>2</sub>O<sub>2</sub> (aq) solution and flowed into the quartz tubing. Since the vapor pressure of H<sub>2</sub>O<sub>2</sub> in the H<sub>2</sub>O<sub>2</sub> (aq) solution is smaller than CH<sub>3</sub>I, higher temperature of the bubbler is required. The HO<sub>2</sub> radicals are produced upon photolysis of H<sub>2</sub>O<sub>2</sub> in air as follows, which can give us a continuous source of HO<sub>2</sub> radicals ranging from 0.8 ppb to 2 ppb:



In our experiment, three measurements on NO<sub>2</sub> were carried out to obtain the CL and instrumental detection sensitivity of the peroxy radicals. First we get the CRDS reading in the “background mode” configuration was taken with only NO and the calibration air sample with CH<sub>3</sub>O<sub>2</sub>/HO<sub>2</sub> in the PERCA reactor; this corresponds to the small amount of background NO<sub>2</sub> impurity in the NO reagent gas and the background ozone generated in the zero sample gas, by removing CH<sub>3</sub>O<sub>2</sub>/HO<sub>2</sub> from the Teflon filter in the “background mode”. Then the two-way valve was switched to the “radical mode” configuration with only NO and calibration air (CH<sub>3</sub>O<sub>2</sub>/HO<sub>2</sub>) in the reactor, in which CH<sub>3</sub>O<sub>2</sub>/HO<sub>2</sub> was converted to NO<sub>2</sub> (without amplification) by

reacting with NO in the flow system. The difference between those two NO<sub>2</sub> concentration readings was from the NO<sub>2</sub> converted from the CH<sub>3</sub>O<sub>2</sub>/HO<sub>2</sub> radicals; as the CH<sub>3</sub>O<sub>2</sub>/HO<sub>2</sub> radicals can be quantitatively converted to NO<sub>2</sub> in the excess amount of NO, this difference signal was effectively equal to the CH<sub>3</sub>O<sub>2</sub>/HO<sub>2</sub> concentration ([RO<sub>2</sub>]). After getting the CH<sub>3</sub>O<sub>2</sub>/HO<sub>2</sub> concentration, CO was introduced and another NO<sub>2</sub> reading (PERCA NO<sub>2</sub> signal) was taken with NO, CO and calibration air (CH<sub>3</sub>O<sub>2</sub>/HO<sub>2</sub>) in the reactor (with amplification). Therefore the amplified NO<sub>2</sub> signal ([NO<sub>2</sub>]) from the CH<sub>3</sub>O<sub>2</sub>/HO<sub>2</sub> radicals in the radical source is equal to this PERCA NO<sub>2</sub> signal subtracting the signal from the value in the “background mode” configuration. The ratio between the amplified signal and the radical concentration gave the chain length of the chemical amplification [12].

$$\Delta[\text{NO}_2]/[\text{RO}_2] = \text{CL} \quad (4-16)$$

In the calibration processes, optimized signals require a stable zero-air baseline, and the difference between “radical mode” and “background mode” need to be measured accurately because it is small. The two CRDS channels can achieve a standard deviation, precision of 150 and 160 pptv/ 10s (1σ), respectively, under laboratory conditions. The difference of these two channels (Δ[NO<sub>2</sub>]) has a precision that is equivalent to a quadrature addition of the two NO<sub>2</sub> readings from each channels, with 220 pptv/10 s(1σ). With the high sensitivity of CRDS detection of NO<sub>2</sub>, a reliable CL can be readily obtained. With the optimized CL of 180 (discussed later), the detection sensitivity of RO<sub>x</sub> can be calculated using the equation [RO<sub>x</sub>] = [NO<sub>2</sub>]/CL, and can achieve as low as 1.2 ppt/10s (1σ).

## 4.3. Results and discussion

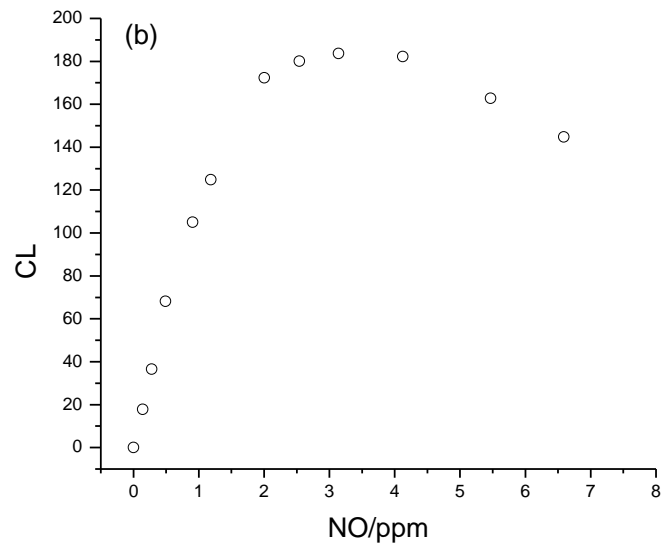
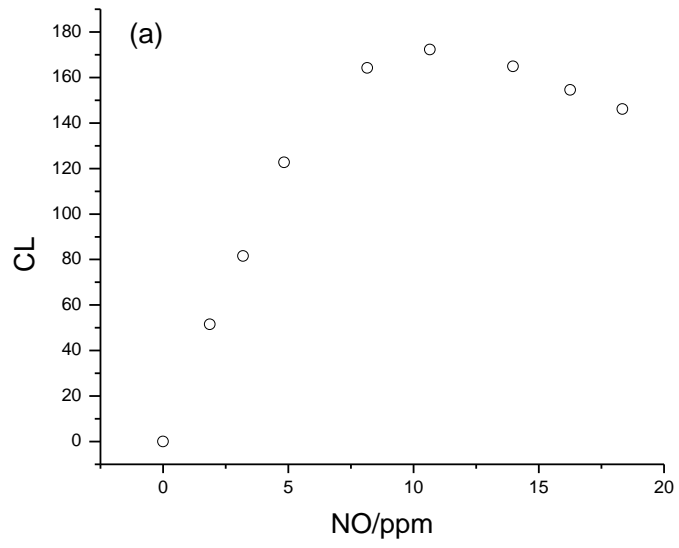
### 4.3.1. Instrumental characterization

The instrument was characterized using the calibration system; reaction system and CL were optimized. NO and CO concentrations, and reaction time were varied to find the optimal CL and the calibration curve with CL of  $\text{CH}_3\text{O}_2$  radical was also analyzed.

#### 4.3.1.1. NO dependence.

Figure 4 shows the dependence of the chain length of the PERCA/ CRDS system on the NO concentrations for several  $\text{CH}_3\text{O}_2/\text{HO}_2$  concentrations with a reaction time of 1s. With a constant CO concentration (8% vol/vol) in the calibration system, the measured chain lengths initially increased with NO mixing ratio, then passed through a maximum value before decreased. This phenomenon has been explained in literature [15]. Basically, under the condition of sufficient [CO], as [NO] increases, the rate of reaction [12] becomes greater relative to those of reactions (6), and an increase in CL is observed. As [NO] increases the radical population shifts toward higher [OH]/[HO<sub>2</sub>] ratios until radical removal occurs predominately via the reaction of OH with NO (6). Further increase in [NO] therefore results in a decrease in the CL. Comparing higher  $\text{CH}_3\text{O}_2$  concentration (1.2ppb) (Figure 4 (a)) with lower  $\text{CH}_3\text{O}_2$  concentration (0.5 ppb) (Figure 4 (b)), it indicates that higher  $\text{RO}_2$

concentration requires higher NO mixing ratio (10 ppm) to reach the maximum CL. Figure 4 (c) shows that the CL for the HO<sub>2</sub> radical has the same behavior with larger value, while the effective CL of CH<sub>3</sub>O<sub>2</sub> (~180) is proximately 90% CL of HO<sub>2</sub> (~200), which is in agreement with earlier work by Cantrell [24]. Since in the ambient atmosphere, the RO<sub>x</sub> level is normally in the range of 0-0.2ppb, 2.5ppm of [NO] should be suitable for most of the ambient measurements.





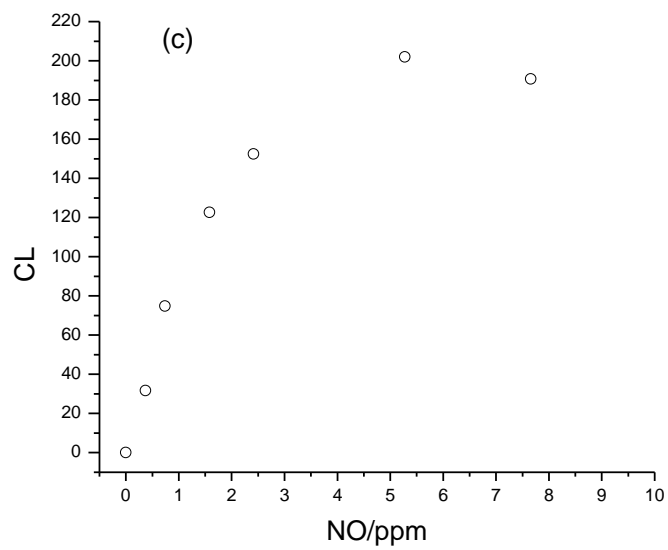


Figure 4- 4 Dependence of CL of the calibration system on NO concentration.

(a)  $[\text{CH}_3\text{O}_2] = 1.2 \text{ ppb}$ . (b)  $[\text{CH}_3\text{O}_2] = 0.5 \text{ ppb}$ . (c)  $[\text{HO}_2] = 0.75 \text{ ppb}$ .

#### 4.3.1.2. CO dependence

Figure 4-5 shows the dependence of the chain length of the PERCA/ CRDS system on the CO concentrations for several  $\text{CH}_3\text{O}_2/\text{HO}_2$  concentrations in the reaction time of 1s. CL increases with the CO mixing ratio toward a limiting value of  $\sim 180$  (for  $\text{CH}_3\text{O}_2$ ) at a constant NO concentration of 2.5 ppm. At low  $[\text{CO}]$ , the radical termination is dominated by loss of OH by reaction (6). As  $[\text{CO}]$  increases, the rate of the chain propagation reaction (3) becomes greater, relative to the chain termination reaction (6), and consequently, the chain length increases. However, at high  $[\text{CO}]$ , radical loss is dominated by removal of  $\text{HO}_2$  and the CL is determined by the ratio of the rate of conversion of  $\text{HO}_2$  to OH by reaction [12] and the rate of loss of  $\text{HO}_2$  by reactions (7) and (8). Reaction [12] and (7) and (8) do not involve CO, and the system therefore becomes insensitive to further increase in its concentration [15]. Figure 5 (a) shows the CO dependence for  $\text{CH}_3\text{O}_2$  concentration (0.6 ppb). And similar to NO dependence experiments, the effective CL of  $\text{CH}_3\text{O}_2$  is proximately 90% CL of  $\text{HO}_2$ . (in Figure 6(b),  $[\text{HO}_2] = 0.9$  ppb) Considering the toxicity and inflammability limit of CO,  $\sim 8\%$  vol/vol of CO is suitable to most of the ambient condition measurement.

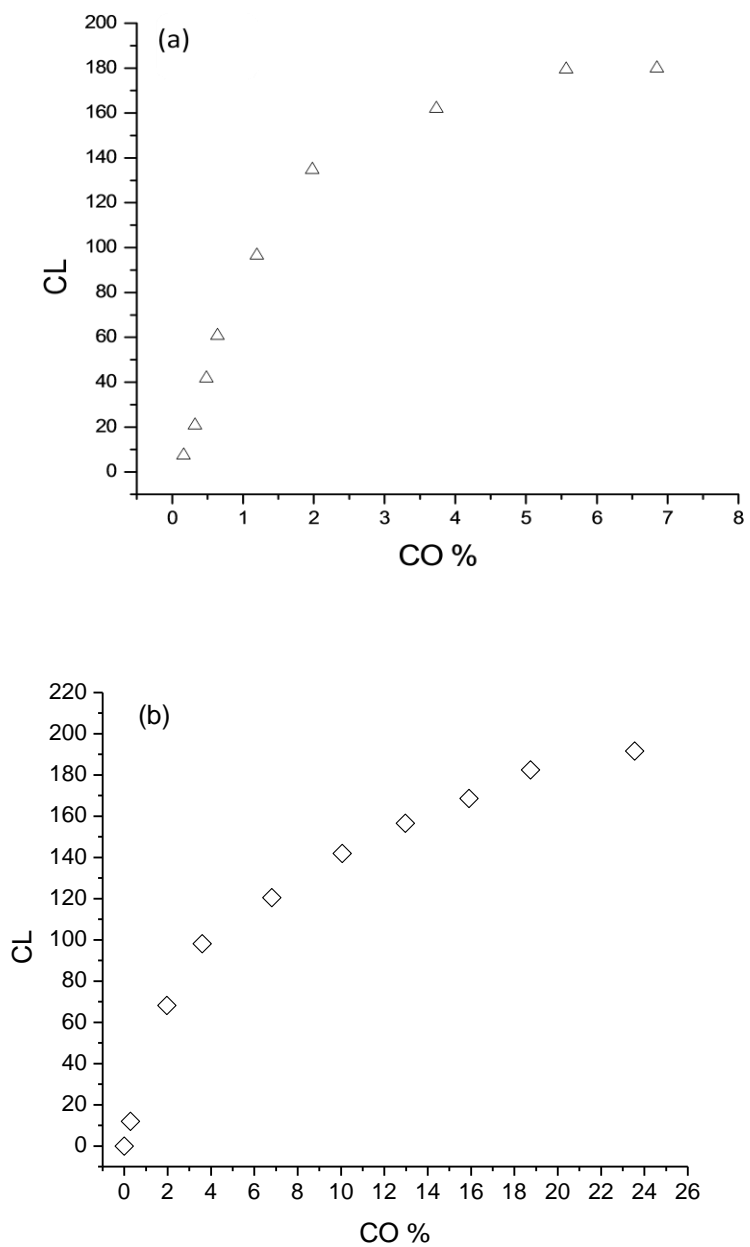


Figure 4- 5 Dependence of CL of the calibration system on CO concentration. (a)  $[CH_3O_2] = 0.6$  ppb. (b)  $[HO_2] = 0.9$  ppb.

#### 4.3.1.3. Reaction time dependence

CL for  $\text{CH}_3\text{O}_2$  was measured as a function of the gas residence time in the flow reactor of the calibration system. The measurements were obtained by varying the length of the  $\text{RO}_x$  reactor at otherwise constant conditions. A higher concentration of  $\text{CH}_3\text{O}_3$  radical ( $\sim 2$  ppb) was used in order to enhance the signal level in the short reaction time in these calibration experiments. Therefore the CL value is much smaller than its optimized value of  $\sim 180$  when the NO and CO concentrations remained 2.5 ppm and 8% vol/vol, respectively. Figure 4-6 shows that the CL raises rapidly up to a reaction time of approximately 1s, after which, the longer reaction time might get interferences from decomposition of PAN and PNA, which is discussed in the interferences (Sec 4.3.2).

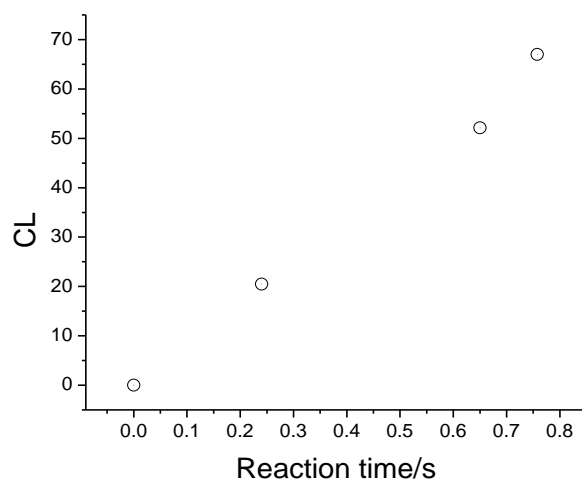


Figure 4- 6 Dependence of the CL of the calibration system and residence time

#### *4.3.1.4. Calibration curve of CRDS signal and RO<sub>2</sub> concentration*

Under the optimum condition, calibration is conducted by use of the CH<sub>3</sub>O<sub>2</sub> resources. The calibration system is described above (Sec 4.2.3). Figure 4-7 represents an example of the calibration curve with CH<sub>3</sub>O<sub>2</sub> radical concentrations ranging from 0.4 pptv to 1pptv. The horizontal axis is the RO<sub>2</sub> (CH<sub>3</sub>O<sub>2</sub>) calculated concentration by dilution. This concentration of CH<sub>3</sub>O<sub>2</sub> radical was first measured using the NO converted NO<sub>2</sub> CRDS signal (~1.1ppb) and then diluted by a certain amount N<sub>2</sub> adding downstream of the quartz tubing. The concentration range of CH<sub>3</sub>O<sub>2</sub> radical was then calculated by this dilution factor. The vertical axis is the concentration of CH<sub>3</sub>O<sub>2</sub> radical reading from CRDS - PERCA method using the optimal CL value of 180. Good linearity was obtained which proved that the CRDS - PERCA method can be applied for the measurement of RO<sub>2</sub> with its concentration in this dramatic range.

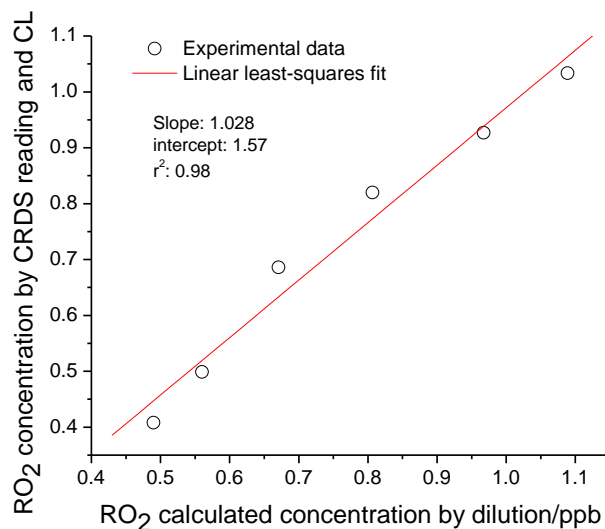


Figure 4- 7 Calibration curve of CRDS signal and  $\text{CH}_3\text{O}_2$  radical concentration. Solid line represents the regression line.

### 4.3.2 Interferences

#### 4.3.2.1. Water - Vapor Interference

Water vapor can potentially interfere with the radical detection. It has been reported that chemical amplifiers for measurement of  $\text{RO}_x$  show a strong change in CL value caused by water vapor enhanced radical losses [15], as a results, the CL decreases monotonously with the humidity in the reactor. To qualify the reduction of CL due to water vapor interference in our instrument, a calibration system has been developed and the dependence of humidity and CL was investigated. In order to vary the humidity in the flow reactor, additional air flow was provided. This

additional air was controlled by a needle valve and passing through a water bubbler and then connected to the system at downstream of the quartz tubing. This additional air pathway has a by-pass pathway to connect to the system without passing the water bubbler. By carefully control the needle valve, a certain amount of carrier gas passed through the water bubbler and the by – pass pathway maintained the same flowrates for the system to keep the same reaction time for all the experiments. Controlling the needle valve could give us different humidity in the system while other conditions remain the same. Figure 8 shows an example of the dependence of the chain length on the relative humidity. Water vapor depress the CL value by more than 60% at RH > 65% and it does not have an obvious influence on the CL value when the RH < 30%. This result is consistent with measurements of the pervious PERCA studies [10].

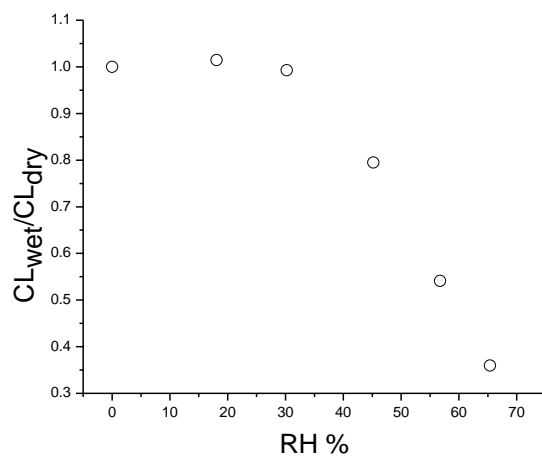


Figure 4- 8 Dependence of CL on the relative humidity of the calibration system.

#### 4.3.2.2. *O<sub>3</sub> background*

The increase of the NO<sub>2</sub> level with addition of NO from the ambient background NO<sub>2</sub> signal is mainly from the ambient O<sub>3</sub> background. The ambient ozone can react with the high-level NO (~ ppm) in the PERCA reactor to produce NO<sub>2</sub>,  $O_3 + NO \rightarrow NO_2 + O_2$  ( $k = 1.84 \times 10^{-14}$  cm<sup>3</sup>/molecules s). This reaction occurs in both channels. In both channels, the ambient NO<sub>2</sub> signals due to the O<sub>3</sub> concentrations are the same, as both have the same ambient sample air and the NO + O<sub>3</sub> reaction is not part of the chemical amplification. Essentially, ozone could be considered as background interference and does not affect the measurement of the RO<sub>x</sub> radicals. In addition, with the difference of the NO<sub>2</sub> readings with and without NO, O<sub>3</sub> concentration could be obtained as a reference. During our experiment, the NO<sub>2</sub> level in the ambient air is measured first, and then NO was added to the ambient air and the increased NO<sub>2</sub> signal was measured again; the difference of these two levels was due to the ambient ozone. Overall, the background interference from the ambient ozone was effectively accounted for and removed

#### 4.3.2.3. *PAN and PAN interference*

Atmospheric pollutants such as NO<sub>2</sub>, CO, and hydrocarbons have little interference on the PERCA measurement because the radical chemical reactions are predominantly controlled by the reagent gases (CO, NO). A potential source of interference is the thermal decomposition of atmospheric PAN and PAN, which



releases peroxy radicals. Since our CRDS system does not operate at low pressure as other LIF systems [25], the interference of the decomposition of these two kinds of species can be neglected in a short reaction time (1s).

#### **4.3.3. Ambient measurements**

Ambient measurements of the peroxy radicals were carried out in the winter of 2011 from outside our laboratory building at the University of California, Riverside, which is about 4 miles east of downtown Riverside and 60 miles east of Los Angeles. Our sample point was located outside window of our lab, which was in the shadow and faced a street. A parking lot is ~100 meter away from the point. As a result, the NO and NO<sub>2</sub> concentrations were high and fluctuated rapidly. The dual channel CRDS system has two inlets and each inlet has identical sampling method. In each inlet, samples were obtained by drawing ambient air in through the Teflon tubing that ran through a hole in the windowsill of the laboratory, and the ambient air was then immediately introduced into the reactor. Since the free radicals are easily destroyed by any surface, no trap or filter was employed for the ambient air before it entered the reaction inlet. The operating conditions of the PERCA and CRDS instruments are described in the experimental section. The CRDS measurements were taken every 2 sec average. The ambient measurements have been carried out for the afternoon of Jan 12 2011, the daytime of Jan 13 2011 and Jan 14 2011 to demonstrate the dual channel- PERCA-CRDS Method.

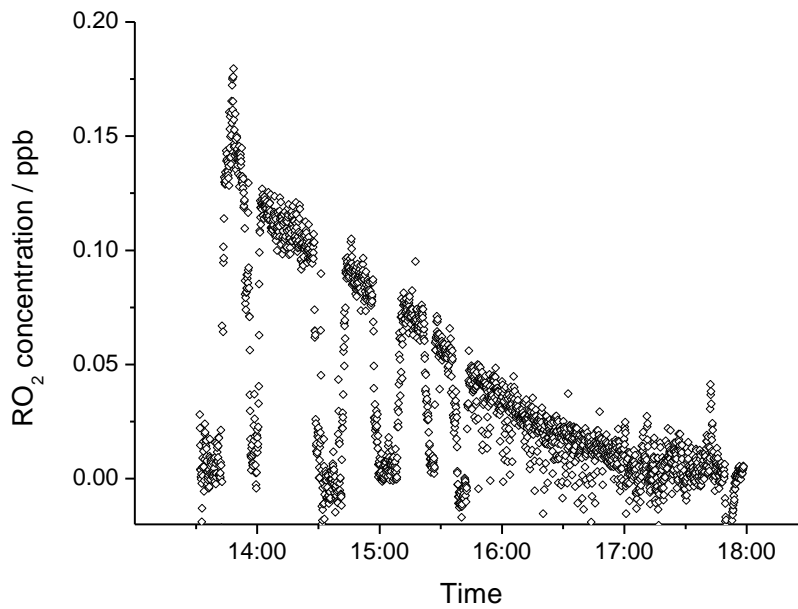
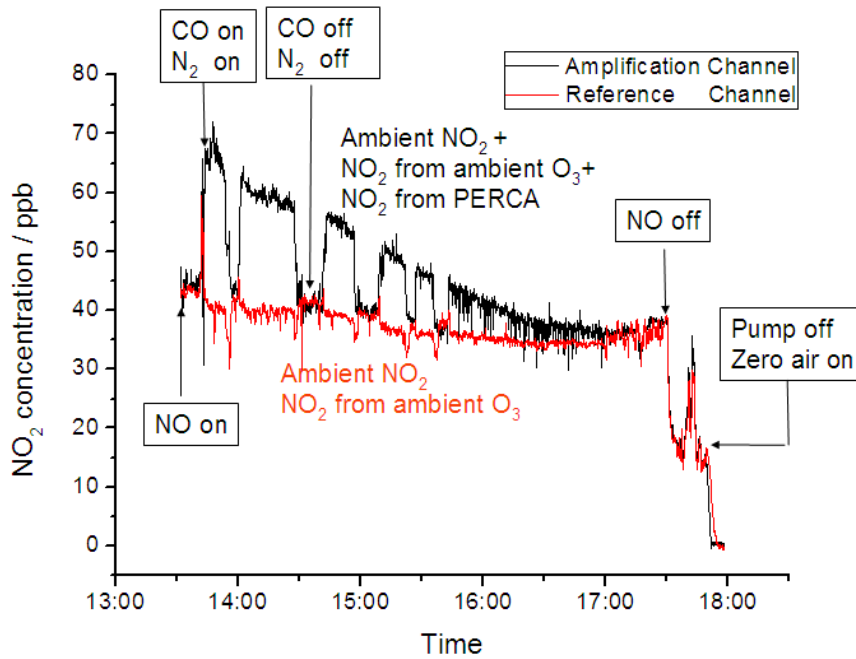


Figure 4- 9 Ambient air measurement of the RO<sub>x</sub> radicals on Jan 12, 2011.

Figure 4-9 shows a half day time data from 11:30 to 18:00 (from noon time to sunset) on Jan 12, 2011. It illustrates the raw NO<sub>2</sub> signals from both channels and the net RO<sub>x</sub> signals produced from the dual channel data. At the beginning of the experiment (Figure 4-9 (a)), the NO was injected into both of the channels to convert the ambient O<sub>3</sub> (and/or any other oxidations) into NO<sub>2</sub>, after that, CO and N<sub>2</sub> were introduced into the amplification channel and reference channel, respectively. In the amplification channel, the PERCA chain reactions of RO<sub>2</sub> are repeated and amplify the level of NO<sub>2</sub> (black line), while the reference inlet measured the sum of the background NO<sub>2</sub> and O<sub>3</sub> (and/or any other oxidations) (red line). To have a reliable reading, the CO and N<sub>2</sub> gas were turned off periodically to ensure that the PERCA reactions in the amplification channel are not initialized without CO and the amplification channel return to the level of reference channel, which demonstrated the difference between the two channels are caused by the PERCA reactions. The converted NO<sub>2</sub> ( $\Delta[\text{NO}_2]$ ) from RO<sub>x</sub> amplification is determined as the difference between the amplification and the reference channels. The RO<sub>x</sub> concentration is then be determined using this difference signal divided by the CL, which is 180 in our experimental setup. Around sunset time (17:20), both of the amplification channel and reference channel were in agreement, which proved that all the peroxy radicals were eliminated by that time. NO was then turned off for both of the channels and the difference between the signal with NO and without NO is due to ambient O<sub>3</sub> (and/or any other oxidations) level; thus the O<sub>3</sub> (and/or any other oxidations) level is accounted for as the background interference. The NO<sub>2</sub> signal level for the ambient

air sample only, without addition of NO and CO in the flow system, is mostly due to the ambient NO<sub>2</sub> (as the aerosol is removed by the filter before the ringdown cavity), and is indicated as the background NO<sub>2</sub> signal in both of the dual channels in Figure 4-9(a). At the end of this experiment, both of the sampling pumps were turned off and the zero-air signal level was measured and chosen as the zero concentration. From Figure 4-9 (a), the ambient NO<sub>2</sub> is about 14 ppb and the level of O<sub>3</sub> is about 26 ppb for that time. The NO<sub>2</sub> and O<sub>3</sub> background has been recorded at the beginning and the end of each experiment and they are in agreement with the online data according to the available online database taken by the California Air Resources Board at Mount Rubideaux approximately 6 km to the west.

Figure 4-9 (b) shows the RO<sub>x</sub> concentration derived from the data in figure 4-9 (a) using the equation  $([RO_x]) = [\Delta NO_2]/CL$ . Several dips in this figure are due to background checking by cutting the CO and N<sub>2</sub> gases off which described before.

Figure 4-10 shows the whole day data from sunrise to sunset for RO<sub>x</sub> concentrations measured on Jan 13, 2011 and Jan 14, 2011. Several spikes in both of the figure 9 and figure 10 are due to pressure spikes from switching on and off the gas flows. The RO<sub>x</sub> concentration level is generally below 0.15 ppb; and it increases from sunrise and gradually approaches its maximum level around 12:00 to 14:00, and then gradually decreases until finally reaches to zero at sunset. This tendency is coordinate with the intensity of the sunlight flux. The ideal instrument detection sensitivity is 1.2 ppt/10s (1σ) which was obtained in the calibration experiments and has been discussed before. However, in the ambient measurement, detection

sensitivity is worse than this ideal case due to the fluctuation of ambient temperature, pressure, concentrations of background NO<sub>2</sub> and / or O<sub>3</sub> and the real fluctuant response of ambient RO<sub>x</sub>. Therefore, the realistic sensitivity is ~ 8 ppt /10s (1σ), which is still remarkable compare to other studies with a better fast time response [4, 8-11].

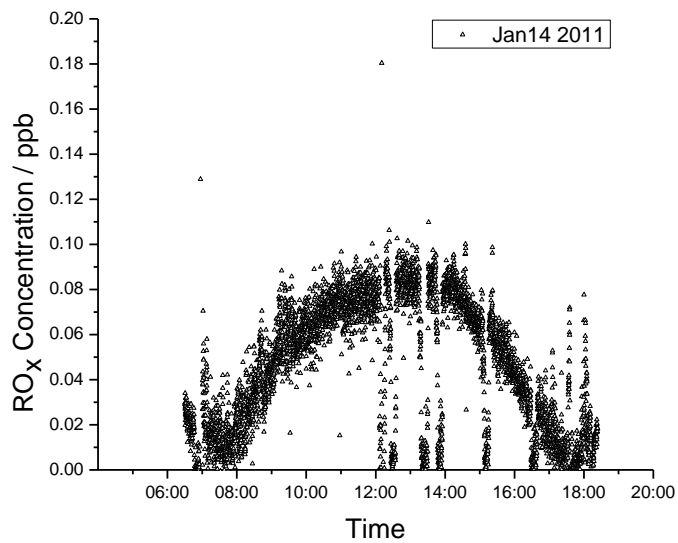
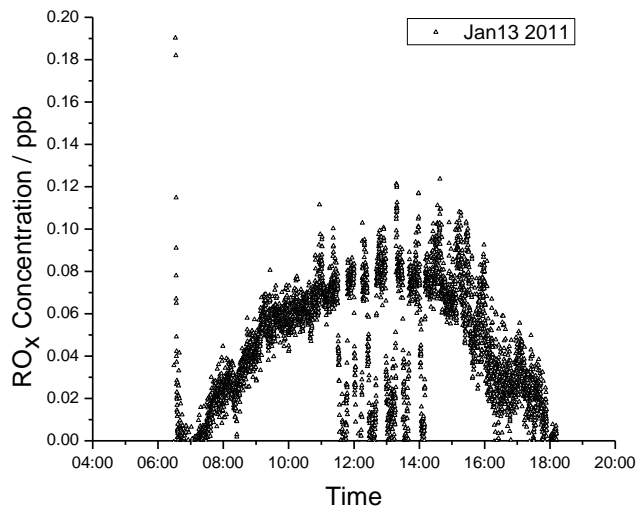


Figure 4- 10 Ambient measurements of  $RO_x$  from sunrise to sunset on Jan 13, 2011 (upper) and (b) Jan 14, 2011 (bottom).

## 4.4. Conclusion

The dual-channel PERCA-CRDS method described in this work is an improvement over our previous single-channel version [17]. The dual inlet system employs two identical inlet reactor-NO<sub>2</sub> detector combinations, one of which is operated in the background, while the other operates in the radical measurement mode. It continuously monitors the background and can minimize the effects of fluctuations in background O<sub>3</sub> and NO<sub>2</sub>. In addition, it improves the time response and allows the detection of changes in peroxy radical concentrations that are related to the rapid changes in nitric oxide concentrations and ozone photolysis frequency. The instrument has a detection sensitivity of 1.2 ppt/10s (1 $\sigma$ ) which approach the sensitivity of LIF with simpler operation and less interference. The CL factor has been fully characterized and optimized at 180. These studies will provide accurate and real time measurement of peroxy radicals in lab study and in ambient atmosphere. The development of portable instruments based on diode lasers and CRDS is a significant advancement. It is hoped that these new CRDS techniques will provide accurate measurement of peroxy radicals for both understanding atmospheric chemistry and monitoring air quality, and with their small size and low costs, they may be utilized widely for many future experiments.

### Reference:

1. Jung, C. and B.K. Rhee, Simultaneous determination of thickness and optical constants of polymer thin film by analyzing transmittance. *Appl. Opt.*, 2002. **41**(19): p. 3861-3865.
2. Mihelcic, D., P. Musgen, and D.H. Ehhalt, An Improved Method of Measuring Tropospheric NO<sub>2</sub> and RO<sub>2</sub> by Matrix-Isolation and Electron-Spin-Resonance. *Journal of Atmospheric Chemistry*, 1985. **3**(3): p. 341-361.
3. Kanaya, Y., et al., Development of a ground-based LIF instrument for measuring HO<sub>x</sub> radicals: Instrumentation and calibrations. *Journal of Atmospheric Chemistry*, 2001. **38**(1): p. 73-110.
4. Creasey, D.J., et al., Implementation and initial deployment of a field instrument for measurement of OH and HO<sub>2</sub> in the troposphere by laser-induced fluorescence. *Journal of the Chemical Society-Faraday Transactions*, 1997. **93**(16): p. 2907-2913.
5. Hard, T.M., et al., Diurnal HO<sub>2</sub> Cycles at Clean-Air And Urban Sites in the Troposphere. *Journal of Geophysical Research-Atmospheres*, 1992. **97**(D9): p. 9785-9794.
6. Stevens, P.S., J.H. Mather, and W.H. Brune, Measurement of Tropospheric OH and HO<sub>2</sub> by Laser-Induced Fluorescence at Low-Pressure. *Journal of Geophysical Research-Atmospheres*, 1994. **99**(D2): p. 3543-3557.



7. Holland, F., M. Hessling, and A. Hofzumahaus, In-Situ Measurement of Tropospheric OH Radicals by Laser-Induced Fluorescence - a Description of the KFA Instrument. *Journal of the Atmospheric Sciences*, 1995. **52**(19): p. 3393-3401.
8. Cantrell, C.A. and D.H. Stedman, A possible technique for the measurement of atmospheric peroxy radicals. *Geophysical Research Letters*, 1982. **9**(8): p. 846-849.
9. Cantrell, C.A., D.H. Stedman, and G.J. Wendel, Measurement of atmospheric peroxy radicals by chemical amplification. *Analytical Chemistry*, 1984. **56**(8): p. 1496-1502.
10. Sadanaga, Y., et al., Development of a measurement system of peroxy radicals using a chemical amplification/laser-induced fluorescence technique. *Review of Scientific Instruments*, 2004. **75**(4): p. 864-872.
11. Cantrell, C.A., et al., Measurement methods for Peroxy radicals in the atmosphere. *Advances in Chemistry Series*, 1993(232): p. 291-322.
12. Volkamer, et al., High-resolution absorption cross-section of glyoxal in the UV-vis and IR spectral ranges. Vol. 172. 2005, Amsterdam, PAYS-BAS: Elsevier.
13. Bertram, T.H., R. C. Cohen, W. J. Thorn III and P. M. Chu (2005), Consistency of ozone and nitrogen oxides standards at tropospherically relevant mixing ratios. *Journal of the Air & Waste Management Association*, 2005. **55**(10): p. 1473-1479.

14. Hastie, D.R., et al., Calibrated chemical amplifier for atmospheric RO<sub>x</sub> measurements. *Analytical Chemistry*, 1991. **63**(18): p. 2048-2057.
15. Clemitshaw, K.C., et al., A calibrated peroxy radical chemical amplifier for ground-based tropospheric measurements. *Journal of Geophysical Research-Atmospheres*, 1997. **102**(D21): p. 25405-25416.
16. Hu, J. and D.H. Stedman, Free radical detector for tropospheric measurement using chemical amplification. *Analytical Chemistry*, 1994. **66**(20): p. 3384-3393.
17. Yingdi Liu, R.M.-C., James Hargrove, David Medina and Jingsong Zhang, Measurements of Peroxy Radicals Using Chemical Amplification-Cavity Ringdown Spectroscopy. *Environ. Sci. Technol*, 2009. **43** (20): p. 7791–7796.
18. O'keefe, A. and D.A.G. Deacon, Cavity ring-down optical spectrometer for absorption measurements using pulsed laser sources. *Review of Scientific Instruments*, 1988. **59**(12): p. 2544-2551.
19. Wheeler, M.D., et al., Cavity ring-down spectroscopy. *Journal of the Chemical Society-Faraday Transactions*, 1998. **94**(3): p. 337-351.
20. Brown, S.S., et al., Simultaneous in situ detection of atmospheric NO<sub>3</sub> and N<sub>2</sub>O<sub>5</sub> via cavity ring-down spectroscopy. *Review of Scientific Instruments*, 2002. **73**(9): p. 3291-3301.
21. Fuchs, H., et al., A Sensitive and Versatile Detector for Atmospheric NO<sub>2</sub> and NO<sub>x</sub> Based on Blue Diode Laser Cavity Ring-Down Spectroscopy. *Environmental Science & Technology*, 2009. **43**(20): p. 7831-7836.

22. Hargrove, J., et al., Cavity ring-down spectroscopy of ambient NO<sub>2</sub> with quantification and elimination of interferences. *Environ. Sci. Technol.*, 2006. **40**(24): p. 7868-7873.
23. Paul, D., A. Furgeson, and H.D. Osthoff, Measurements of total peroxy and alkyl nitrate abundances in laboratory-generated gas samples by thermal dissociation cavity ring-down spectroscopy. *Review of Scientific Instruments*, 2009. **80**(11).
24. Cantrell, C.A., R.E. Shetter, and J.G. Calvert, Dual-inlet chemical amplifier for atmospheric peroxy radical measurements. *Analytical Chemistry*, 1996. **68**(23): p. 4194-4199.
25. Fuchs, H., et al., Determination of inlet transmission and conversion efficiencies for in situ measurements of the nocturnal nitrogen oxides, NO<sub>3</sub>, N<sub>2</sub>O<sub>5</sub> and NO<sub>2</sub>, via pulsed cavity ring-down spectroscopy. *Analytical Chemistry*, 2008. **80**(15): p. 6010-6017.

# **Chapter 5 Study of gas Initial steps of phase ozonolysis of important alkene using VUV photoionization time-of-flight mass spectrometry: cis-2-butene, tetramethylethylene and cyclohexene.**

## **Abstract**

Ozone-alkene reactions are significant removal processes of alkenes in the troposphere and generation processes of secondary organic aerosol (SOA), and they are also important sources of OH radicals. To detect the early transient reactive intermediates and investigate the mechanisms of initial steps of ozonolysis of alkenes, these gas-phase reactions are carried out in a fast flow reactor under the conditions of low pressure (7-10 Torr) and room temperature. The alkenes investigated include *cis*-2-butene, tetramethylethylene and cyclohexene. CO is used as an OH scavenger to minimize the reactions between the OH byproduct and alkenes. After a short reaction time of ~ 25 - 200 ms, the initial products, both free radical intermediates and stable species, are sampled into a supersonic molecular beam and directly detected by 118-nm vacuum ultraviolet (VUV) photoionization time-of-flight mass spectrometry (TOFMS). Mass peaks corresponding to the Criegee intermediates or their isomers are identified. The alkene-ozone reactions with longer reaction time (up to 10 s) and 1 atm pressure are also carried out and

studied. A general trend in the mass spectra and the reaction mechanisms will be discussed.

## 5.1. Introduction

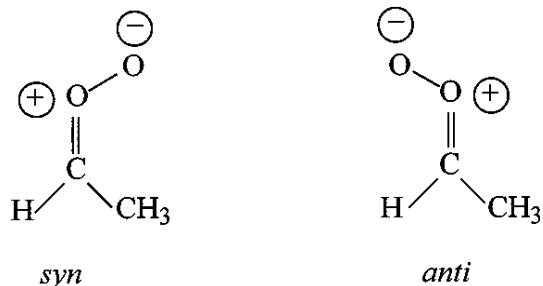
Alkenes are the major class of volatile organic compounds (VOCs) emitted from vegetation [1] [2], and are also emitted from anthropogenic sources, including in vehicle exhaust [3]. In urban areas, alkenes (primarily from anthropogenic sources) comprise ~10% of nonmethane VOCs [1]. A substantial portion of the atmospheric oxidation of all alkenes is due to reaction with ozone; hence, an accurate description of both urban and rural ozone formation requires an understanding of the ozone-alkene reaction. Although ozone-alkene reactions have been studied for decades, many questions remain, particularly as to the fate of the Criegee biradicals in the gas phase [4]. Some of these studies have found evidence for substantial quantities of OH formation from the O<sub>3</sub> reaction with alkenes, such as tetramethylethylene [5] propene [6] [7], isobutene [6], and a series of terpenes [8]. The studies of tetramethylethylene [5] and propene [7] provide the quantification of this OH source, at 0.7 and roughly 0.3 per molecule of alkene reacted. Quantification and analysis of the effect of the OH source on other measured quantities remain very scarce, as does an explanation of the pathway to the formation of OH. Further, although possible mechanisms for the generation of the

products have been suggested, there is no direct observation of the intermediates and the overall understanding of the reaction mechanisms is still inadequate [9].

The ozonolysis reactions of alkenes are thought to proceed *via* the formations of 5-membered ring energy rich compounds (primary ozonide, POZ) which are formed by initial addition of O<sub>3</sub> across the C=C unsaturated bond. The highly energized POZs undergo (a) direct decomposition into a carbonyl oxide (Criegee intermediate, CI) and a carbonyl product, or (b) non-concerted decomposition, followed by 1,4-hydrogen shift [10-15].

The significance of the non-concerted decomposition is unclear; however, the direct decomposition is usually considered as the primary reaction channel, as shown in reaction (5-1) [16]. The complexity of the ozonolysis reactions arises from the subsequent isomerizations, decompositions and reactions of CIs, which are produced with extensive vibrational and/or electronic excitation.





The chemically activated carbonyl oxides are proposed to undergo collisional stabilization [reaction (5-2a)], isomerization to a “hot” hydroperoxide followed by breakage of the O-OH bond to form an OH radical plus a substituted alkyl radical [the “hydroperoxide channel,” reaction (5-2b)] [13, 20, 21], rearrangement to a “hot” ester with subsequent decomposition [the “ester channel,” reaction (5-2c)], or elimination of an O (<sup>3</sup>P) atom [reaction (5-2d)].

For monosubstituted carbonyl oxides (the carbonyl oxides are hereafter termed Criegee intermediates), formation of OH radicals through the hydroperoxide channel is anticipated to occur almost totally from the *syn* configuration [19, 21, 22]. And, unless the OH radicals formed in the primary O<sub>3</sub> reaction with an alkene are scavenged, the reaction systems involve both O<sub>3</sub> and OH radical reactions with the alkene and the measured products and their yields are not those for the O<sub>3</sub> reaction alone [23-25]

We have undertaken to examine the free radical as well as carbonyl production from the alkene ozonolysis reactions in an effort to delineate the mechanism for these reactions. We have carried out a series of different alkene experiments, including *cis*-2-butene, tetramethylethylene and cyclohexene to study all of them with and without the addition of CO, which serves as an OH scavenger. We have



focused on identifying and quantifying even relatively minor products to understand the reaction pathways of the Criegee biradicals.

## 5.2 Experimental

The gas phase reactions were studied in a homemade fast flow reactor coupled with a VUV photoionization time-of-flight mass spectrometry (TOFMS) through a 0.26 mm sampling orifice. The configuration of the fast flow reactor and TOFMS has been described in Chapter 2, which consisted of a fast flow reactor, in which radicals and products are generated and reacted, and a linear TOFMS, in which radicals and products are detected. The ionization region of the TOFMS was located about 5 cm behind the 0.26 mm orifice and the nascent compounds (exiting from the orifice) were ionized by 118.2 nm (10.48 eV) photons produced by frequency tripling the 355 nm output of a Nd:YAG laser in a Xe cell (~15 Torr) and were subsequently detected in the TOFMS. The TOFM spectra were collected using a digital oscilloscope (Tektronix) and averaged 500-2000 laser shots; they were then converted to mass spectra using the appropriate time to mass transformation.

The alkene – ozone reactions have been carried in the experimental setup showed in Figure 2-2. *cis*-2-butene (Aldrich chemical company 99+%) was first diluted in argon with a volume ratio of 1:10 in a lecture bottle and then introduced into the system at room temperature. Cyclohexene (Aldrich chemical company 99%) and tetramethylethylene (TME) (2,3-dimethyl-2-butene) (Aldrich chemical company

99%) were diluted in He, without additional purification. This was accomplished by bubbling the He carrier gas through the liquid at ice/water bath temperatures. The CO gas first passed through an iodated charcoal filter to remove impurities such as carbonyl complexes in the CO gas cylinder [26]. The flow rate of CO (99.999%, Airgas Inc.) as an OH scavenger was around 100 mL/min in the ozone – alkene reactions. Occasionally, to ensure enough CO was involved in the reaction, larger flow rate of CO (up to 150 mL/min) was used. As showed in Figure 2-2, CO was introduced into the system using the same inlet with alkene/He gas mixture. Ozone was generated by static electric discharge of oxygen gas from an ozone generator (Welsbach T408, ~ 5% O<sub>3</sub> in O<sub>2</sub>). The O<sub>3</sub>-O<sub>2</sub> mixture from the ozone generator was passed through a silica gel trap at dry-ice temperature, and O<sub>3</sub> was adsorbed on the silica gel. O<sub>3</sub> was then carried out by passing zero air as the carrier gas through the silica gel trap and introduced into the system as an encounter flow with alkene and CO flow. All the flowrates were controlled precisely by needle valves and monitored by mass flow meter (Aalborg). The concentration of alkenes were varied from ~  $1 \times 10^{13}$  molecule/cm<sup>3</sup> to ~  $1 \times 10^{15}$  molecule/cm<sup>3</sup> by controlling the flow rates of CO, zero air and He gases. As shown in Figure 2-2 and described in Chapter 2, the reactant gases were injected in line A and reacted and then exhausted from line B. The reactions nascent products are detected by TOFMS.

## 5.3 Results

Prior to any ozonolysis experiments, blank experiments and background experiments were run for each of the reagents used in this study. These blanks served as reference mass spectra of the pure starting reactants, allowing for the clear identification of product mass peaks when they appeared. In each case, the blanks were in good agreement with literature spectra. Background experiments were also carried out and recorded for reference. The background experiments were included: zero air background, zero air and ozone background, and zero air, ozone and CO background. By comparing and analyzing the blank and background experiments results, product mass peaks can be identified accurately and clearly.

One consideration with respect to the mass spectra is that the ion peak intensities do not quantitatively reflect the partial pressures of the corresponding neutral species since ion intensity is a function of both partial pressure and mass spectral sensitivity, such as ionization cross sections. The latter could vary widely and is not easily characterized in our laboratory, which explains why a minor product such as ketene, which might have a high sensitivity, would be prominent in the mass spectra [27].

### 5.3.1 *cis*-2-butene + O<sub>3</sub>

The first system studied in this project is the ozonolysis reaction of *cis*-2-butene, which had been thoroughly investigated by Martinez and co-workers

[27] using stopped-flow reactor coupled to a photoionization mass spectrometer in 1980's. In 2010 Clay and Ault [28] claimed that in their matrix isolation studies, which combined with infrared spectroscopy of the twin jet codeposition of ozone and cis-2-butene into argon matrices, have led to the first observation of several early intermediates in this ozonolysis reaction. These studies included the formation and identification of the long sought-after Criegee intermediate, as well as confirmed evidence for earlier reports of the primary and secondary ozonides. Many other published work also used cis-2-butene ozonolysis for proposing a general mechanism for ozone- alkene reaction systems to account for the major products formed in reaction (5-1) and in subsequent free radical reactions. As a result, cis-2-butene is a good agent not only for serving as a simple linear alkene representing for other more complicated alkenes but also a good reference to compare our results with the previous works for a foundation for later experiments with other alkenes.

In this work, the cis-2-butene + O<sub>3</sub> reaction experiments were conducted with samples of cis-2-butene/Ar and O<sub>3</sub>/zero air with merged regions (reaction zone) 50 cm in length for 1/8" Teflon tubing connected with 7 cm long 1/4" Teflon tubing. The zero air gas flowrate was 200ml/min for carrying ozone; and the flowrate of argon which diluted cis-2-butene gas (butene 10% vol/vol) was 4 ml/min. The flowrate for CO as an OH scavenger is 100 ml/min. Under these conditions, the initial concentration of cis-2-butene was roughly  $3 \times 10^{14}$  molecules /cm<sup>3</sup> and the O<sub>3</sub> concentration is about  $2 \times 10^{15}$  -  $1 \times 10^{16}$  molecules /cm<sup>3</sup> in order to achieve the

consumption of ~20% - 80% of butene in the presence of excess ozone. The pressure of the reaction system (line A) was 10 Torr with CO on and 8 Torr with CO off. When the CO was on, the concentration of CO was  $7 \times 10^{16}$  molecules /cm<sup>3</sup>, which allowed 200 times of alkene concentration. The ~20 ms short reaction time before the products passing through the 0.26mm orifice allowed initial steps of ozone – alkene reactions to be detected by TOFMS.

The mass spectra of this experiment is shown in Figure 5-1 and listed in Table 5-1. We attempt to assign each observed peak in the mass spectra to a reaction product or to a fragment ion arising from a product or parent, and then compare with the previous study by Martinez and co-workers [27]. The number of possible isomeric species or species of the same nominal mass corresponding to any given mass spectral peak makes identification on the basis of mass spectra alone difficult, but by referring literature, the identification of products can be supported and a general mechanism could be proposed.

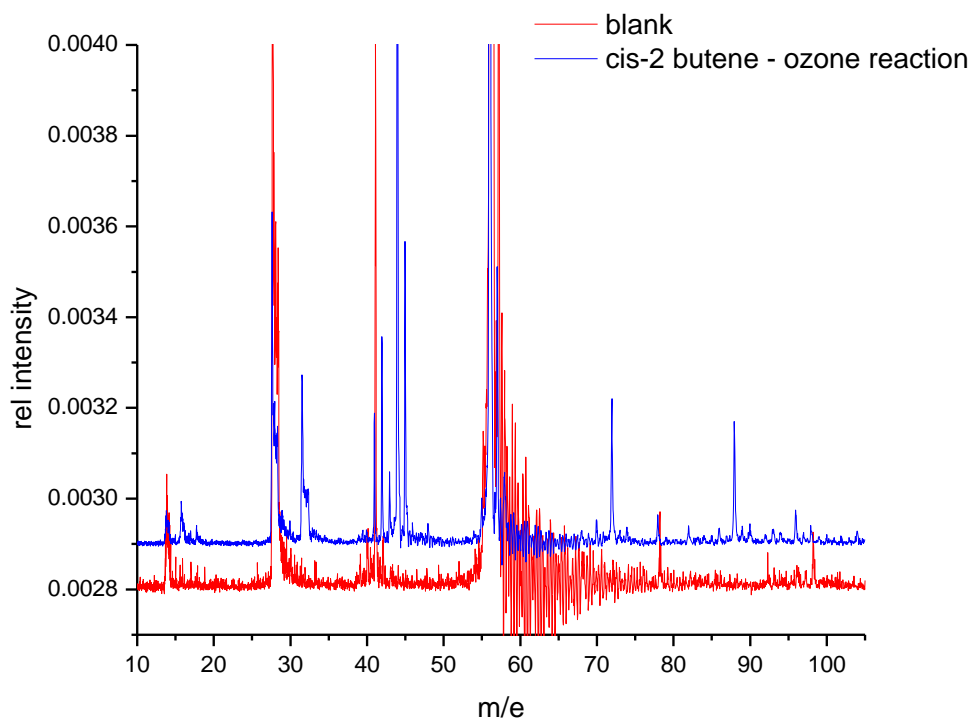
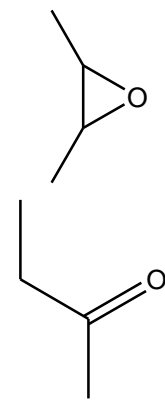
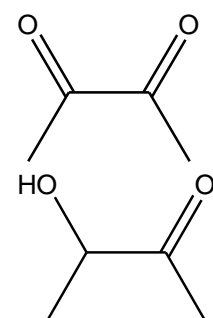
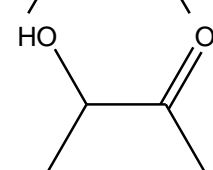
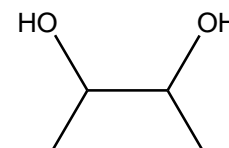
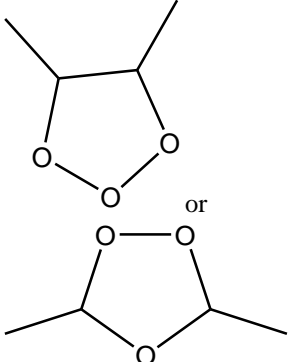


Figure 5- 11 Mass spectrum of ozone cis-2-butene reaction compared with blank spectrum.

Table 5- 1 Peak assignments for the mass spectrum of ozone plus cis-2-butene

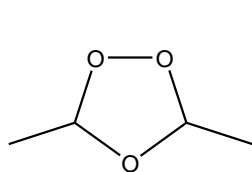
m/e	Intensity: CO off	Compare d intensity: CO on	Possible assignments	possible structure
14 and 28			$N^+$ and $N_2^+$	
16 and 32		Decrease	$O^+$ and $O_2^+$	
18	Vw		$H_2O$	
30	Vw		HCO	
40	Vw		parent related	
41	M		parent related	
42	S	Decrease	$H_2CCO$	$H_2C=C=O$
43	w	Increase	$CH_3CO$	$H_3C=O^+$ or $CH_2CHO$
44	Vs		$CH_3CHO$	

45	S		CH <sub>3</sub> CHOH	
46	V <sub>w</sub>		HC(O)OH, CH <sub>3</sub> CH <sub>2</sub> OH	
48	V <sub>w</sub>		CH <sub>3</sub> OOH	
55	W		parent related	
56	V <sub>s</sub>	Increase	parent peak	
57	M		parent related	
58	W	Increase	Glyoxal	CHOCHO
70	W	Increase	CH <sub>2</sub> CHCOCH <sub>3</sub>	
72	S	Increase	CH <sub>3</sub> CH <sub>2</sub> COCH <sub>3</sub>	
				or
74	V <sub>w</sub>	Increase		
78	S		Impurity	
82	S	Decrease		
84	M		butene+CO	
86	V <sub>w</sub>		CH <sub>3</sub> COCOCCH <sub>3</sub>	
88	S	Decrease	CH <sub>3</sub> COCHOHCH <sub>3</sub>	
89	V <sub>w</sub>			
90	V <sub>w</sub>	Decrease	(CH <sub>3</sub> CHOH) <sub>2</sub>	
92, 93, 94	V <sub>w</sub>		impurity	
96	W	Increase		
98	W		impurity	

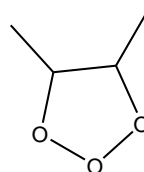
104	W	Decrease	ozonide	
-----	---	----------	---------	---

106	M	(For Peak intensity, w=weak, m=medium, s=strong, v=very )		
-----	---	---	--	--

The first step for the ozone – alkene reaction is the addition of ozone to form 5 number ring on C=C bond, which is the primary ozonide. The primary ozonide has high energy and is unstable, so it falls apart into CI and a carbonyl product. However, the CI and carbonyl product might recombine to form secondary ozonide. Since both of the primary and the secondary ozonide compounds have the same m/e (104), they could not be distinguished in the mass spectrum. Titration of the CI by addition of aldehyde leads to enhancement of the secondary ozonide signal as a consequence of CI and oxoalkane combination reaction[27],[29].



primary ozonide



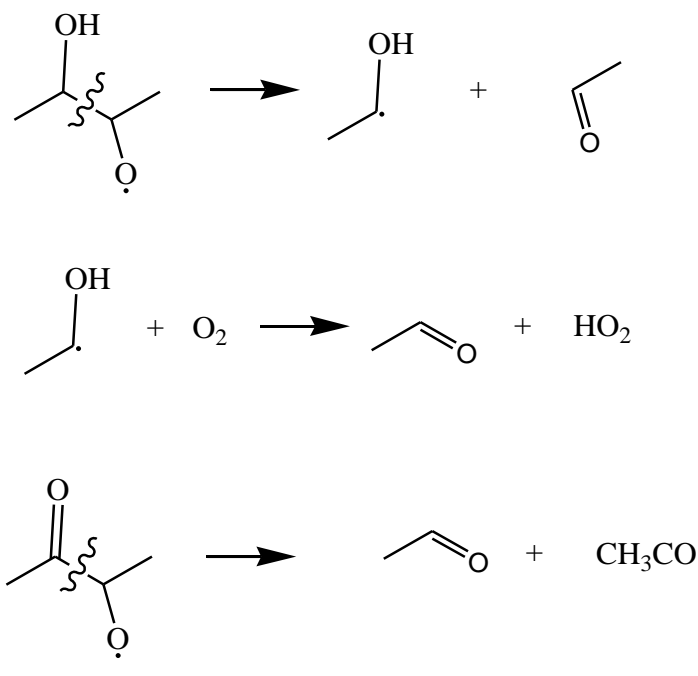
secondary ozonide

The most important product of the ozonation reaction is the oxoalkane expected on the basis of the Criegee mechanism shown in reaction 1. In this case, the m/e 44



peak due mainly to ethanal, it also includes a contribution from oxirane. The Criegee intermediate ( $\text{CH}_3\text{CH-O-O}$ ,  $m/e=60$ ) is an energy -rich compound and easily to fall apart. It can lose one OH group to form  $\text{CH}_3\text{CO}$  ( $m/e=43$ ) radical.

In addition to the ethanal produced via the Criegee split, a significant amount of ethanal probably also result from the OH and cis-2-butene reaction system [30] via such reactions as below:



Methanol is observed at  $m/e$  30 and it is probably formed by reactions of free radicals such as  $\text{CH}_3$  and  $\text{CH}_3\text{O}$  with  $\text{O}_2$  and / or  $\text{O}_3$ . Peaks 40, 41, 55, 56, 57 are parent (cis-2 butene) related and they could serve as a reference for the progress of the reaction.

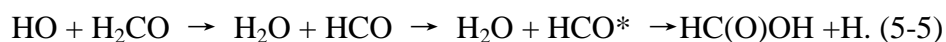
On the basis of its kinetic behavior [31], the product peak at  $m/e$  42 is almost certainly due to ketene. Although the ketene peak is a prominent feature in the mass

spectra because of the high mass spectral sensitivity of ketene, the actual amount formed is small. The observed ketenes is formed by the hydroperoxide R'C(OOH)CHR'', which is formed by rearrangement of an initially formed CI, undergoes the intermolecular elimination processes (shown as below).



It is almost certain that peak 43 contribute vinyloxy radical (CH<sub>2</sub>CHO). Formation of vinyloxy (CH<sub>2</sub>CHO) radical, a proposed co-product of OH from dissociation of Criegee intermediates following the primary ozonolysis of 2-butenes, was observed in these ozonolysis reactions using cavity – ring down spectroscopy in our previous work. Mass peak 43 might also be a fragment ion, which comes from the ionization of m/e 72, 86 and 88 compounds. Peak 45 may also comes from ionization, probably comes from m/e 88 and 90.

Peak 46 might be HC(O)OH or CH<sub>3</sub>CH<sub>2</sub>OH, but most likely HC(O)OH because under this oxidizing atmosphere, CH<sub>3</sub>CHO is hard to be reduced by adding a H to form ethanol. The formation of HC(O)OH might be as below:



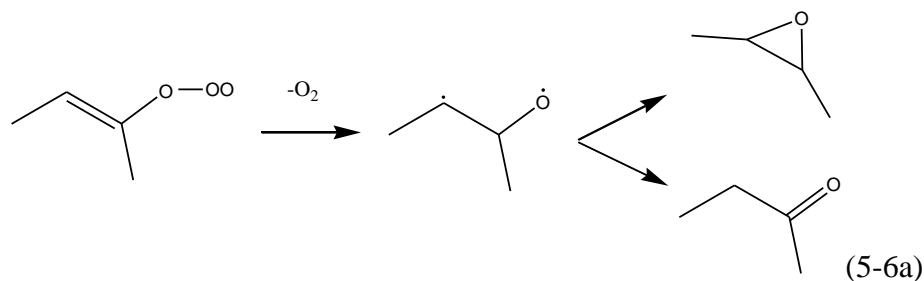
Peak 48 is probably from the radical combination of CH<sub>3</sub> and HO<sub>2</sub>.

The glyoxal (m/e 58) is a unique and important indicator for the hydroperoxide channel of CI. For the C<sub>n</sub>H<sub>2n</sub> alkenes, it has been explained and indicated that C<sub>m</sub> dioxoalkanes and C<sub>m</sub> ketenes, where m<n, originated from the primary, excited dioxymethylene via its isomerization to the hydroperoxide. For example, ketene and glyoxal are C<sub>m</sub> products of alkenes containing the CH<sub>3</sub>C(H)=

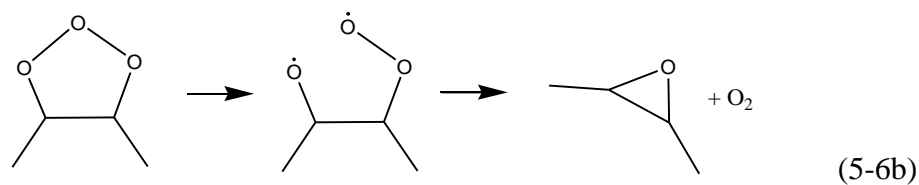
moiety, while methylketene and methylglyoxal are  $C_m$  products of alkenes containing, respectively, the  $CH_3CH_2C(H)=$  and  $(CH_3)_2C=$  moieties [27, 32]

Peak 70 is the  $R(\text{alkene}) + 14$  peak, which was also discussed by previous work[27]. The  $R + 14$  peaks corresponds to  $C_n$ - substituted ketenes and/or  $C_n$  conjugated oxoalkenes (in Table 5-1,  $O_3 + 2\text{-butene} \rightarrow 3\text{-buten-2-one}$ ). 3-buten-2-one has been confirmed as a product of the  $O_3$  and 2-butene reaction by gas chromatography [27, 32]. Longer reaction time (10s) and under 1 atm pressure, this  $m/e$  70 peak becomes very strong.

The peak at  $m/e$  72 is due to 2, 3-epoxybutane and 2-butanone. Epoxides and oxoalkanes arising from the parent alkene are known to be products of the solution phase ozonation of alkenes. Based on the discussion of Martinez [27] , we conclude that under our experimental conditions, these epoxides and oxoalkanes arise from a primary ozonation reaction, as discussed by Bailey[6, 15], which shows below:



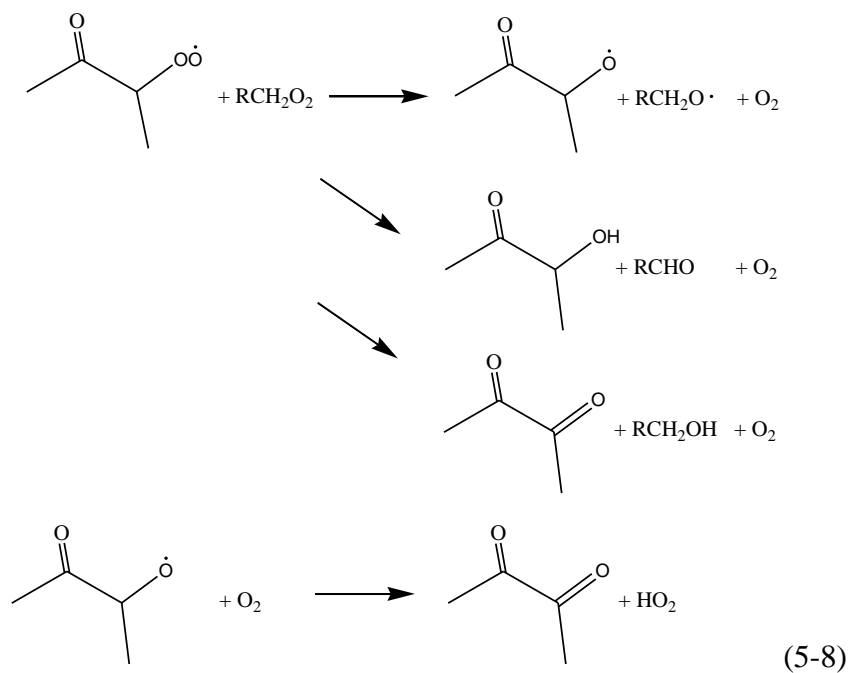
Or



Under our experimental conditions we cannot distinguish between these two reactions as the source of epoxyalkane.

In considering the mass spectrum of the ozone-cis-2-butene reaction in Table 5-1 and Figure 5-1, a particularly set of peaks is the triplet at m/e 86,88, and 90, lying 30, 32, and 34 mass units up from the  $C_nH_{2n}$  alkene, are found in all ozone-alkene reaction mass spectra, and have been discussed by the pervious works[29]. It is believed that these are due to  $C_n$ , dioxoalkanes [ $R'C(O)C(O)R''$ ],  $C_n$ , acyloins [oxoalkanols,  $R'C(O)CH(OH)R''$ ], and  $C_n$ , alkanediols [ $R'CH(OH)CH(OH)R''$ ] respectively, which are probably formed via a complex sequence of reactions initiated by reaction of hydroxyl radicals with the alkene. The peak at m/e 86 is probably due to 2, 3-butanedione. This peak is very weak in both of the mass spectrum with and without CO. the peak at m/e 86 is probably due to 2,3-butanedione. this peak is very weak in both of the mass spectrum with and without CO. The peak at m/e 88 is due to 3-hydroxy-2-butanone (acetoin) and was confirmed by GC [27]. This peak is strong and can be dramatically decreased by adding CO. The weak peak observed at m/e 90 is probably due to 2, 3- butanediol. This study involving the addition of radical scavengers CO to the system, we were able to infer that these products at m/e 88, and 90 were due to secondary radical reactions arising from the reaction of the hydroxyl radical with butene, thus leading to 3-hydroxy-2-butanone and 2,3-butanediol.





In the 10 s reaction time and 1 atm experiment, the peaks of mass spectrum are broader and the most apparent peaks are  $m/e$  44, 70, 72.

Our ozone - cis-2-butene experiment has good agreement with the literature and most all the peaks can be explained based on the pervious works, which provides us with a good foundation for other alkene – ozone experiments

### 5.3.2 tetramethylethylene (TME) + O<sub>3</sub>

Another important reaction we studied is the O<sub>3</sub> – TME reaction. TME is a simple branched alkene which is also well studied before. It is different from other chain alkenes because of its higher reactivity and special structure. In this work, the TME and O<sub>3</sub> reaction experiments were conducted similarly with the ozone – butene

reaction mentioned above. TME (2,3-dimethyl-2-butene) were diluted in Helium, without additional purification. This was accomplished by bubbling the 10ml/min Helium noble carrier gas through TME at ice/water bath temperatures samples. The merged region (reaction zone) was still 180 cm in length with 1/8" Teflon tubing connected with 40 cm 1/4" Teflon tubing. The zero air gas flowrate was 80ml/min for carrying ozone. The flowrate for CO as an OH scavenger was 80 ml/min. Under these conditions, the initial concentration of TME is roughly  $6 \times 10^{14}$  molecule /cm<sup>3</sup> and the O<sub>3</sub> concentration was about  $5 \times 10^{16}$  molecule /cm<sup>3</sup> in order to achieve the presence of excess ozone. The reaction system pressure (line A) was 7 Torr with CO on and 4 Torr with CO off, and when the CO was on, the concentration of CO was  $1 \times 10^{16}$  molecule /cm<sup>3</sup> which about 170 times of the alkene concentration. The 100 ms short reaction time before the products passing through the 0.26mm orifices allows initial steps of ozone – alkene reactions to be detected by TOFMS.

The mass spectra of the ozone- TME experiment is shown in Figures 5-2 and by carefully analysis, we have assigned the mass spectra in Table 5-2.

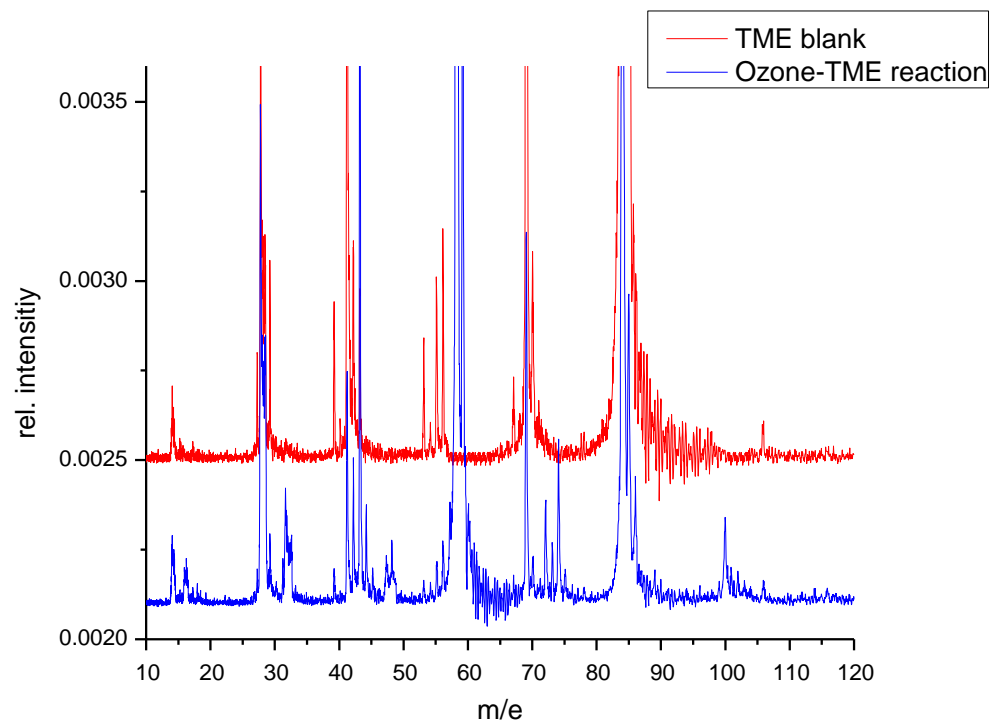
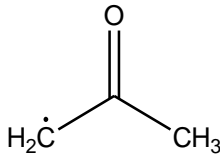
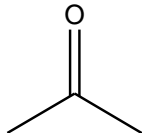
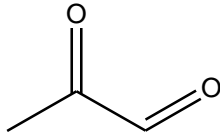
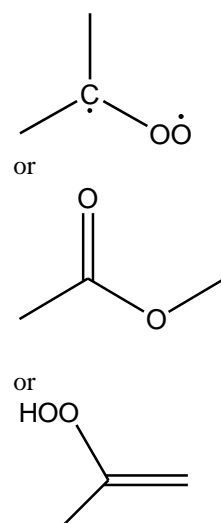
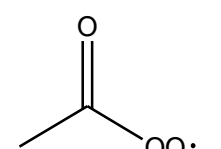
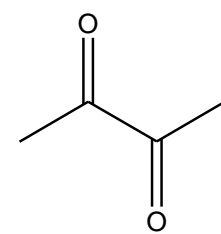
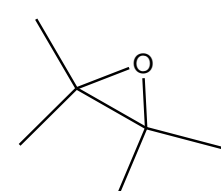
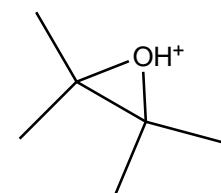


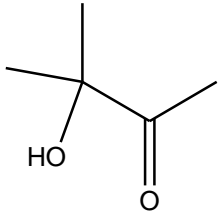
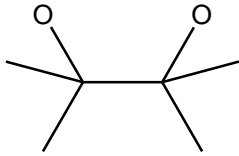
Figure 5- 12 Mass spectrum of ozone TME reaction compared with blank spectrum



Table 5- 2 Mass spectrum of ozone plus TME

m/e	Intensity	Compared intensity:	possible assignments	possible structure
	CO off			
16	vw		O	
28	s b		N <sub>2</sub>	
32	m b		O <sub>2</sub>	
39	w		parent related	
40	vw		parent related	
41	s		parent related	
42	m		H <sub>2</sub> C <sub>2</sub> O	H <sub>2</sub> =C=C=O
43	vs		CH <sub>3</sub> CO	
44	w	increase	CH <sub>3</sub> CHO	
45	vw	decrease		
48	w		O <sub>3</sub> and CH <sub>3</sub> OOH	
53	w		parent related	
54	vw		parent related	
55	w		parent related	
56	w		parent related	
57	m		CH <sub>3</sub> C(=O)CH <sub>2</sub> •	
58	vs		(CH <sub>3</sub> ) <sub>2</sub> CO	
59	s		CH <sub>3</sub> C(O)OH	
60	w		parent related	
69	vs		parent related	
70	w		parent related	
72	m		CH <sub>3</sub> CHCHO	
73	w			

74	s		$\text{CH}_3\text{COOCH}_3$	
75	vw	increase	$\text{CH}_3\text{CO}(\text{OH})\text{CH}_3$	
84	vs	increase	parent	
85	s		parent related	
86	s	increase	$\text{CH}_3\text{COCOCH}_3$	
100	m	increase	$(\text{CH}_3)_2\text{COC}(\text{CH}_3)_2$	
101	vw	increase	$(\text{CH}_3)_2\text{COHC}(\text{CH}_3)_2$ +	

102	vw			
103	vw			
104	vw			
106	w		impurity	
114	vw	decrease		
116	vw	decrease	$(\text{CH}_3)_2\text{COCO}(\text{CH}_3)_2$	

---

(For Peak intensity, w=weak, m=medium, s=strong, v=very )

The ozone-TME reaction has been well studied before, and its 1 atm products are identified using FTIR by Niki and co-workers [5]. We compared our mass spectrum carefully and compared with their work. We found that the products are comparable to the ozone-butene results and believe that the reactions should follow the same procedure. Except the peaks from minor electron impact ionization of  $\text{N}_2$ ,  $\text{O}_2$  and  $\text{O}_3$  and the set of parent related peaks, we focus on the mass peaks arising from the products of ozone – TME reactions.

The first step for the ozone – alkene reaction is again the addition of ozone to form primary ozonide and then splits into CI and oxoalkane. In this case, the  $\text{O}_3$ -TME reaction is so fast that we could not observe either of the primary ozonide or secondary ozonide. Therefore, no R+48 peak can be observed

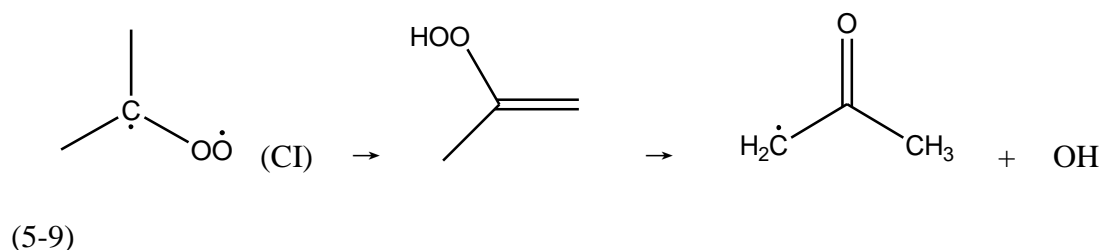
In this  $\text{O}_3$ -TME system, the carbonyl product expected on the basis of the Criegee mechanism shown in reaction 1 is propan-2-one (ketone), which is at m/e 58.

And the strong peak m/e 43 is also related to m/e 58 for it is the fragment ion,  $\text{H}_3\text{CO}^+$  from m/e 58,  $\text{H}_3\text{C}(\text{O})\text{CH}_3$ . Similarly, peak 59 is the fragment ion  $(\text{CH}_3)_2\text{COH}^+$  also probably from m/e 58  $\text{H}_3\text{C}(\text{O})\text{CH}_3$ .

Peak m/e 42 might still be ketene which has similar explanation with that in butene ozonolysis reactions. It could be a Criegee rearrangement product, which is formed by an intramolecular elimination that occurs subsequently to one of the possible intermolecular rearrangements of a Criegee intermediate.

Beside the minor electron impact ionization of  $\text{O}_3$ , peak 48 may also be related to  $\text{CH}_3\text{OOH}$  which has been identified by FTIR before [5].

Peak m/e 72 and 74 do not change with or without CO, which indicate that OH radicals were not involved in the formation of the observed products. The m/e 72 is  $\text{CH}_3\text{C}(=\text{O})\text{CHO}$ , which may arise from the oxidation of  $\text{CH}_3\text{C}(=\text{O})\text{CH}_2 \cdot$  (peak m/e 57) radicals formed in reaction (9). And this methyglyoxal has also been discussed above. The m/e 74 is from the isomerization or stabilization of the CI.

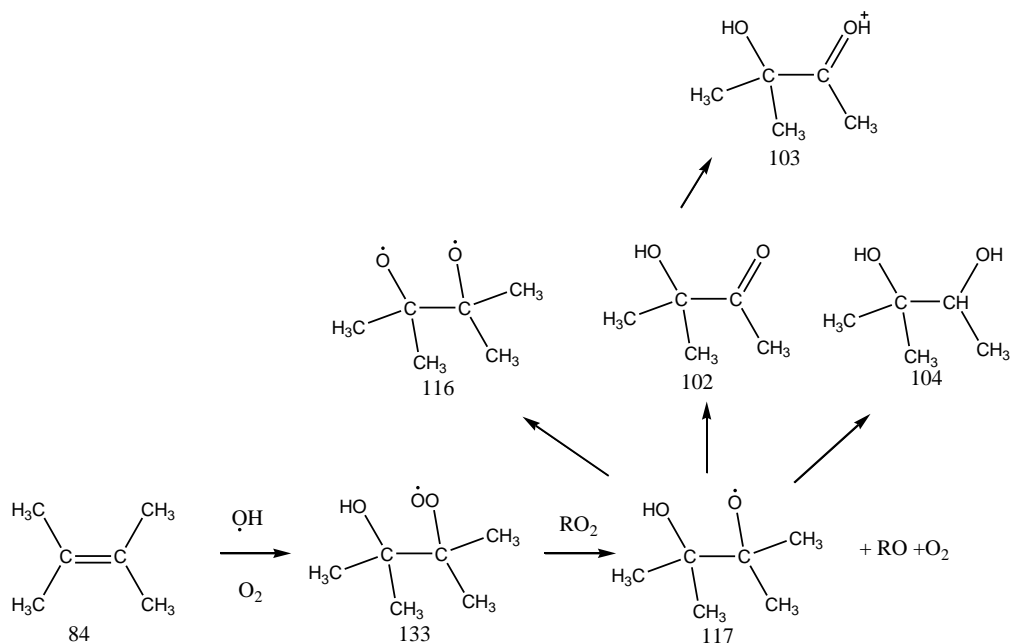


Peak 75 is the  $\text{CH}_3\text{C}(=\text{O})\text{OO}$  radical, which has been identified and proved by Niki and co-workers [5]. In their work, they added  $\text{NO}_2$  into the TME  $\text{O}_3$  system and they saw the marked decrease in the yields of  $\text{CH}_3\text{C}(=\text{O})\text{CHO}$ , which indicated the

highly efficiency of the OH radicals decreasing by NO<sub>2</sub> in their experiments. Among the N-containing products identified in their experiments were HONO, HOONO, and PAN. These products clearly demonstrate the presence of HO, HO<sub>2</sub>, and CH<sub>3</sub>C(=O)OO radicals in the O<sub>3</sub>-TME-O<sub>2</sub> system.

The peak at m/e 100 is due to 2,3-dimethy-2,3-epxybutane and 2,3-dimethy-2-butanone, whose mass is equal to R+16 (R=84 for TME). This process is also following Bailey's theory mentioned before[6, 15] and shown in reaction (5-6). We also notice that when peak 100 increases, peak 101 increases as well, so we assume that the m/e 101 is (CH<sub>3</sub>)<sub>2</sub>COHC(CH<sub>3</sub>)<sub>2</sub><sup>+</sup>, which is related to (CH<sub>3</sub>)<sub>2</sub>COC(CH<sub>3</sub>)<sub>2</sub>.

It is uncertain to assign mass peak 102 to 116 in Table 5-2, except that peak 106 might be impurity. From the peak analysis, we found that peak 116 and 114 decrease with CO, and therefore these reactions might be related to OH initialized alkene reactions. We propose a reaction path shown as following reactions:



(5-10)

In the ozone – TME reaction system, assignments of most of the peaks are in agreement with the previous studies [5]. However, we have observed more peaks, such as the peaks from m/e 102 to 116. Considering that the reaction time in our experiments is much shorter, we argue these additional mass peaks are initial products during the first 100 ms. In this case, it is more likely that these peaks are due free radicals. Base on this argument, peak 74 might be CI instead of  $\text{CH}_3\text{C}(\text{O})\text{CH}_2\text{OH}$ .

In the 1 atm reaction and 7 s reaction time, peak m/e 116, 100, 86, 72, 73, 74, 58 could be detected and all of them should be stable products. In this case, peak 74 should be  $\text{CH}_3\text{C}(\text{O})\text{OCH}_3$ , which is a stable compound.

### 5.3.3 cyclohexene + O<sub>3</sub>

The third system we studied is the reaction between cyclohexene and ozone. cyclohexene is a symmetrical cycloalkene which serves as a model compound for several monoterpenes emitted from vegetation. it has been reported that the reaction of O<sub>3</sub> with cyclohexene forms C<sub>5</sub>- and C<sub>6</sub>- dicarboxylic acids, which nucleate and/or partition into seed particles and are important components of secondary organic aerosol [33-35]. A recent study by Ziemann [35] focused on aerosol phase products formed from the reaction of O<sub>3</sub> with cyclohexene, and later the Atkinson's group investigated the gas phase products formed from the reactions of cyclohexene and cyclohexene-d<sub>10</sub> in the presence of OH radical scavengers using gas chromatography with flame ionization detection, combined with gas chromatography mass spectrometry, in situ FTIR spectroscopy, and in situ atmospheric pressure ionization tandem mass spectrometry [36]. However, all the pervious studies focused on long time reactions and no information has been recorded for the initial steps of this reaction in the first several milliseconds. In this work, we have attempted to study and identify the products in the initial steps of this reaction.

In this work, the cyclohexene and O<sub>3</sub> reaction experiments were conducted similarly with ozone – TME experiments mentioned above. Cyclohexene were diluted in Helium, without additional purification. This was accomplished by bubbling the 10 ml/min Helium noble carrier gas through cyclohexene at ice/water bath temperatures samples. The merged region (reaction zone) is 180 cm in length for 1/8" Teflon tubing connected with 40 cm 1/4" Teflon tubing. The zero air gas

flowrate was 80ml/min for carrying ozone. The flowrate for CO as the OH scavenger was 80ml/min. Under these conditions, the initial concentration of cyclohexene was roughly  $5 \times 10^{14}$  molecule /cm<sup>3</sup> and the O<sub>3</sub> concentration was still about  $4 \times 10^{16}$  molecule /cm<sup>3</sup> in order to achieve the presence of excess ozone. The reaction system pressure (line A) was 6 Torr with CO on and 4 Torr with CO off, and when the CO was on, the concentration of CO was  $9 \times 10^{16}$  molecules /cm<sup>3</sup> which about 173 times of alkene concentration.

#### Figure 5-3

Figure 5- 13 shows the mass spectrum of ozone cyclohexene reaction compared with blank spectrum, and Table 3 shows the mass peak assignment based on our analysis.



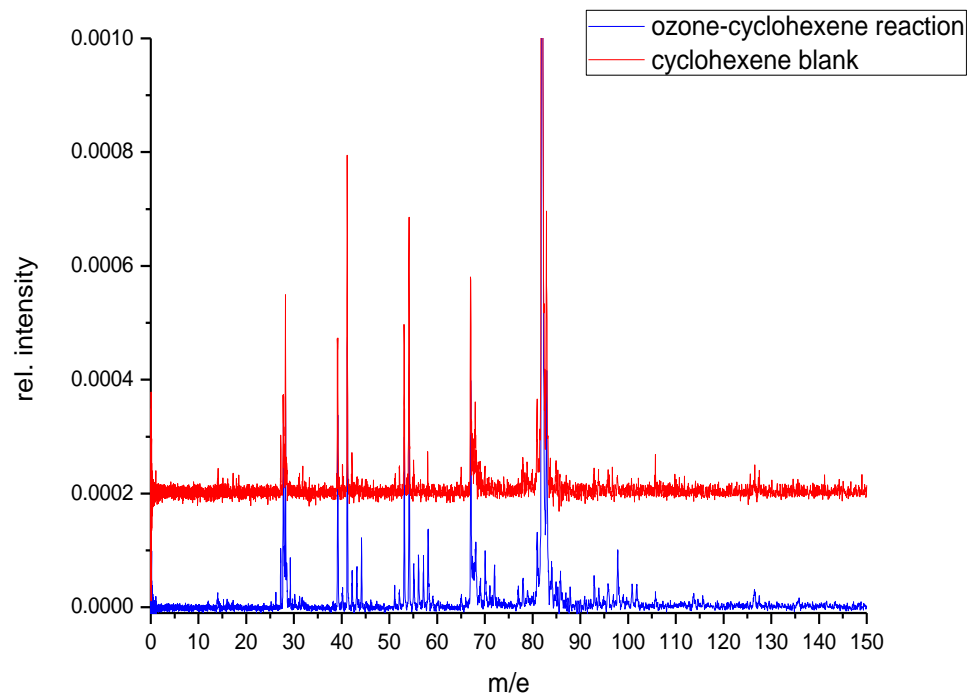
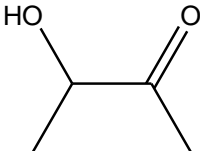
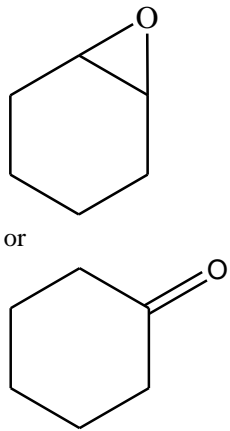
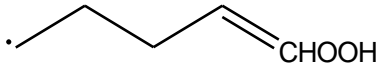
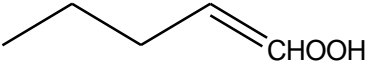
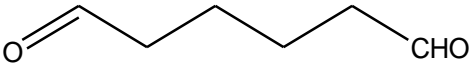


Figure 5- 13. Mass spectrum of ozone cyclohexene reaction compared with blank spectrum.

Table 5- 3. Mass spectrum of ozone plus cyclohexene

m/e	Intensity:	Compared intensity :	possible assignments	possible structure
	CO off	CO on		
14 and 28			$N^+$ and $N_2^+$	
16 and 32		decrease	$O^+$ and $O_2^+$	
18	w		water	
39	s		parent related	
41	s		parent related	
42	s		$H_2CCO$	$H_2C=C=O$
43	m		$CH_3CO$	
44	s		$CH_3CHO$	
45	w		$CH_3CHOH$	
53	s		parent related	
54	s		parent related	
55	w		parent related	
56	s		$CH_2CH_2CH_2CH_2$	
57	w		$CH_2CH_2CH_2CH_3^+$	
58	vs		$H_2C_2O_2$	
59	w			
69	s		parent related	
70	w		$CH_2CHCOCH_3$	$CH_2=CHCOCH_3$
72	m		$CH_3CH_2COCH_3$	
82	s		parent	
83	s		parent related	
84	m		$OCCH_2CH_2CH_2CH_2$	
85	w		$O=CHCH_2CH_2CH_2CH_2$	
86	w		$CH_3CH_2CH_2CH_2CHO$	
88	vw	decrease	$CH_3C(O)C(OH)CH_3$	

98	vs	increase	C <sub>6</sub> H <sub>8</sub> O	
100	vw		HC(O)CH <sub>2</sub> CH <sub>2</sub> CH <sub>2</sub> CHO	
101	vw			
102	w			
106			impurity	
114	w			
127			impurity	
130			HC(O)CH <sub>2</sub> CH <sub>2</sub> CH <sub>2</sub> CH <sub>2</sub> COOH or Or HC(O)CH <sub>2</sub> CH <sub>2</sub> CH <sub>2</sub> CH(OH)CHO	

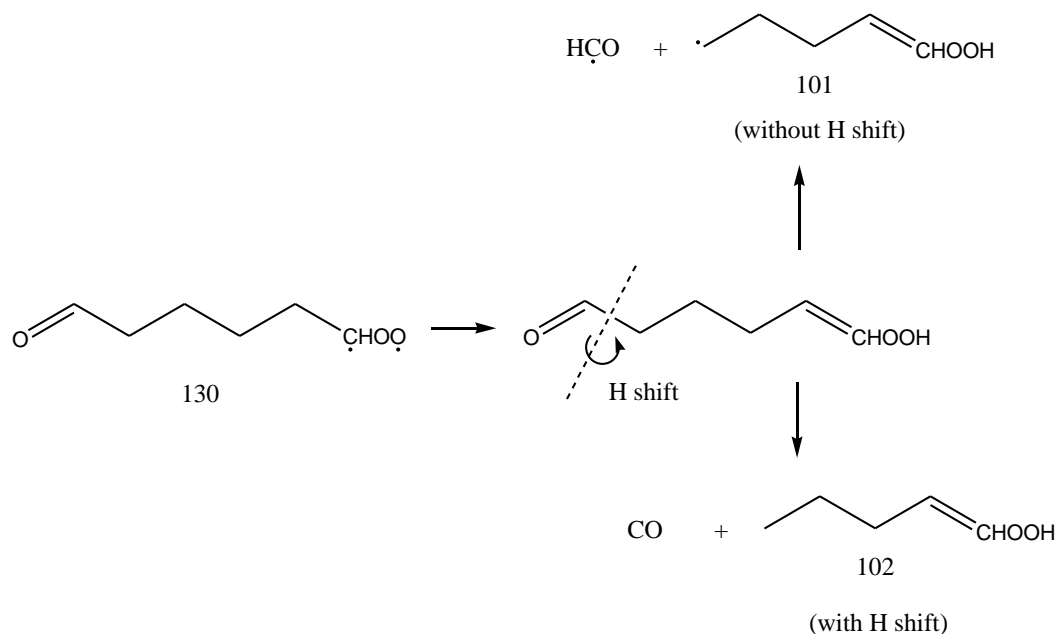
(For peak intensity, w=weak, m=medium, s=strong, v=very )

Based on careful analysis of the mass spectra of the O<sub>3</sub> and cyclohexene reaction, we found that except for several bigger mass peaks, the positions of most of the peaks are similar to those in the ozone cis-2-butene reaction. The mechanism from environment chamber study of reaction of cyclohexene has been proposed by Atkinson [36]. Below is our analysis trying to assign each peak compared with the proposed mechanism.

Since the m/e 130 peak only shows up in longer reaction time experiment (10s), we conclude that the 130 peak is assigned to the stable compound

HC(O)CH<sub>2</sub>CH<sub>2</sub>CH<sub>2</sub>C(O)OH, and the peak 114 to HC(O)CH<sub>2</sub>CH<sub>2</sub>CH<sub>2</sub>CH<sub>2</sub>CHO. Peak 130 could also be HC(O)CH<sub>2</sub>CH<sub>2</sub>CH<sub>2</sub>CH(OH)CHO and peak 100 to HC(O)CH<sub>2</sub>CH<sub>2</sub>CH<sub>2</sub>CHO.

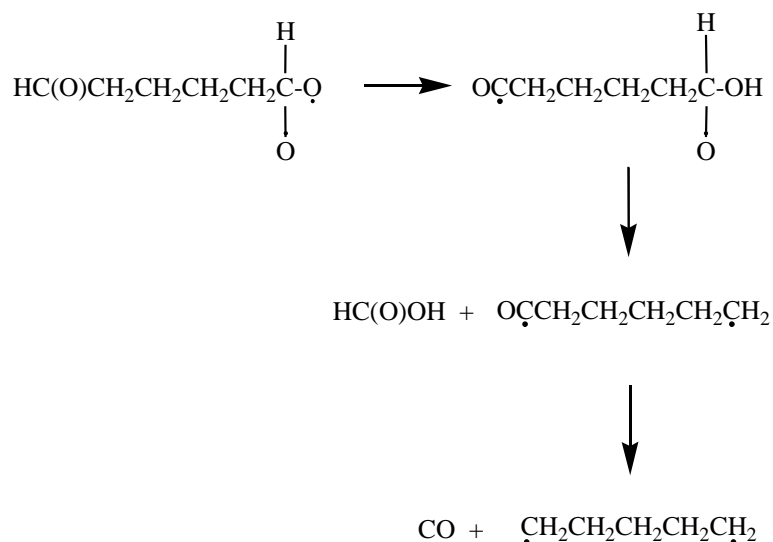
As peak 101 is related to the reaction time, we found that with a shorter reaction time, e.g. < 0.1s (this could be achieved by adjusting the reactor tubing length), the m/e 101 peak became stronger, which indicate that peak m/e 101 is from an initial reaction product, while m/e peak 100 became weaker with shorter reaction time. Apparently, peak 100 is a stable compound, which could be HC(O)CH<sub>2</sub>CH<sub>2</sub>CH<sub>2</sub>CH(OH)CHO, and peak 101 is a radical. The products of m/e peaks 102 and 101 are formed based on the proposed reaction mechanism shown below:



(11)

The peak at m/e 98 is due to cyclohexanone and 7-oxa-bicyclo[4.1.0]heptane, whose mass is equal to R+16 (R=82 for cyclohexene). This process also follows Bailey's theory mentioned before [6, 15] and shown in reaction (5-6).

Peak 88 is one of the peaks which is similar to those in the 2-butene – O<sub>3</sub> reaction. We propose that during the O<sub>3</sub> cyclohexene reactions, radical  $\cdot\text{CH}_2\text{CH}_2\text{CH}_2\text{CH}_2\cdot$  can be formed by the following reaction.



(5-12)

Then, the  $\cdot\text{CH}_2\text{CH}_2\text{CH}_2\text{CH}_2\cdot$  radical behaves like 2-butene to react with O<sub>3</sub> and form a series products. Peak 56 is the splitting part of reaction 12, which is radical  $\cdot\text{CH}_2\text{CH}_2\text{CH}_2\text{CH}_2\cdot$ , or its stable isomer 2-butene. Peak 57 is  $\text{CH}_3\text{CH}_2\text{CH}_2\text{CH}_2\cdot$ , which related to  $\cdot\text{CH}_2\text{CH}_2\text{CH}_2\text{CH}_2\cdot$ , or it is  $^+\text{CH}_3\text{CH}=\text{CHCH}_2$  related to 2-butene.

Peak 41, 42, 43, 44, 45, 58, 70, 72 and 88 are the same products as cis-2-butene and O<sub>3</sub> reactions, which have been discussed before in Section 5.3.1 and they might be the products of O<sub>3</sub> and CH<sub>3</sub>CH<sub>2</sub>CH<sub>2</sub>CH<sub>2</sub> • radicals reactions.

Peak 84 is another splitting part of reaction (5-12), or its stable isomer. Peak 86 is CH<sub>3</sub>CH<sub>2</sub>CH<sub>2</sub>CH<sub>2</sub>CHO which follows the similar reactions shown in reaction (5-1). So peak 85 might be an ionization fragment related to peak 84 and/or peak 86.

In the longer reaction time at 7 Torr pressure, some difference could be observed: peak m/e 86 was stronger with 10s reaction time, which indicated that the more stable compound CH<sub>3</sub>CH<sub>2</sub>CH<sub>2</sub>CH<sub>2</sub>CHO can be generated with longer reaction time. And peak m/e 96 showed up only in longer reaction time. In the 1 atm pressure and 7 s experiments, we noticed that fewer peaks were observed and they are peak m/e 98, 86, 84, 72, 58, 59, 44 and 43. Among them, peak 86 became bigger and peak 84 was smaller, and all the cyclohexene was consumed in this experiment. All of them have been discussed above and we notice that they should be all stable compounds.

## 5.4 Conclusion

Direct observation of ozonolysis of cis-2-butene, tetramethylethylene and cyclohexene are reported. A fast flow reactor coupled with VUV-TOFMS was used to isolate and observe the initial reaction products, both free radical intermediates and stable species. CO has been used as an OH scavenger to eliminate the reaction

between OH and alkenes and the difference between the results with and without CO is discussed. Eliminating the OH-alkene channel will enhance the O<sub>3</sub> – alkene reaction channel and more residue alkene could be observed. Under short reaction time conditions, it is possible to identify the Criegee intermediates. Alkene – ozone reactions with longer reaction time (up to 10 s) and 1 atm pressure were also carried out and studied. The mechanisms of these reactions we proposed are in a good agreement with the previous studies, however, more products are observed and new mechanisms have been proposed and discussed as well.

### **Reference**

1. Sara M. Aschmann, J.A., and Roger Atkinson, Kinetics and products of the reactions of OH radicals with 4,4-dimethyl-1-pentene and 3,3-dimethylbutanal at 296 ± 2 K. *J Phys Chem A*, 2010 114(18): p. 5810.
2. Guenther, A., et al., A global model of natural volatile organic compound emissions. *J. Geophys. Res.*, 1995. 100(D5): p. 8873-8892.
3. Zielinska, B., et al., Volatile organic compounds up to C<sub>20</sub> emitted from motor vehicles; measurement methods. *Atmospheric Environment*, 1996. 30(12): p. 2269-2286.
4. Atkinson, R., et al., Formation of hydroxyl radicals in the gas phase reactions of ozone with a series of terpenes. *J. Geophys. Res.*, [Atmos.], 1992. 97(D5): p. 6065-73.

5. Niki, H., et al., FTIR spectroscopic study of the mechanism for the gas-phase reaction between ozone and tetramethylethylene. *J. Phys. Chem.*, 1987. 91(4): p. 941-6.
6. Huie, J.T.H.a.R.E., Stopped-flow studies of the mechanisms of ozone-alkene reactions in the gas phase propene and isobutene. *Int. J. Chem. Kinet.*, 1978. 10: p. 1019.
7. S.M. Japar, C.H.W., and H. Niki, Effect of molecular oxygen on the gas phase kinetics of the ozonolysis of olefins. *J. Phys. Chem*, 1976. 80: p. 2057.
8. R. Atkinson, D.H., and S. M. Aschmann,, Rate constants for the gas-phase reactions of O<sub>3</sub> with a series of monoterpenes and related compounds at 296K $\pm$ 2-K. *Znt. J. Chem. Kinet*, 1990. 22: p. 871.
9. Paulson, S.E., R.C. Flagan, and J.H. Seinfeld, Atmospheric Photooxidation of Isoprene .2. the Ozone-Isoprene Reaction. *International Journal of Chemical Kinetics* 1992. 24(1): p. 103-125.
10. Calvert, J.G., et al., *The Mechanisms of Atmospheric Oxidation of the Alkenes*. 2000, New York: Oxford University Press. 560 pp.
11. Hatakeyama, S. and H. Akimoto, Reactions of Criegee intermediates in the gas phase. *Res. Chem. Intermed.*, 1994. 20(3-5): p. 503-24.
12. O'Neal, H.E. and C. Blumstein, Nonconcerned Decomposition. *Int. J. Chem. Kinet.*, 1973. 5: p. 397.
13. Fenske, J.D., et al., Measurement of Absolute Unimolecular and Bimolecular Rate Constants for CH<sub>3</sub>CHOO Generated by the trans-2-Butene



Reaction with Ozone in the Gas Phase. *J. Phys. Chem. A*, 2000. 104(44): p. 9921-9932.

14. Anglada, J.M., R. Crehuet, and J.M. Bofill, The ozonolysis of ethylene: A theoretical study of the gas-phase reaction mechanism. *Chemistry-a European Journal*, 1999. 5(6): p. 1809-1822.

15. Harding, L.B. and W.A.I. Goddard, Mechanism of gas-phase and liquid-phase ozonolysis. *Journal of the American Chemical Society*, 1978. 100(23): p. 7180-7188.

16. Baker, J., et al., Reactions of stabilized Criegee intermediates from the gas-phase reactions of O<sub>3</sub> with selected alkenes. *Int. J. Chem. Kinet.*, 2002. 34(2): p. 73-85.

17. Cremer, D., et al., A CCSD(T) investigation of carbonyl oxide and dioxirane. Equilibrium geometries, dipole moments, infrared spectra, heats of formation and isomerization energies. *Chem. Phys. Lett.*, 1993. 209(5-6): p. 547-56.

18. Gutbrod, R., et al., Formation of OH radicals in the gas phase ozonolysis of alkenes: the unexpected role of carbonyl oxides. *Chem. Phys. Lett.*, 1996. 252(3,4): p. 221-229.

19. Gutbrod, R., et al., A Kinetic and Theoretical Investigation of the Gas-Phase Ozonolysis of Isoprene: Carbonyl Oxides as an Important Source for OH Radicals in the Atmosphere. *J. Am. Chem. Soc.*, 1997. 119(31): p. 7330-7342.

20. Kroll, J.H., et al., Mechanism of HO<sub>x</sub> Formation in the Gas-Phase Ozone-Alkene Reaction. 1. Direct, Pressure-Dependent Measurements of Prompt OH Yields. *J. Phys. Chem. A*, 2001. 105(9): p. 1554-1560.
21. Kroll, J.H., et al., Mechanism of HO<sub>x</sub> formation in the gas-phase ozone-alkene reaction. 2. prompt versus thermal dissociation of carbonyl oxides to form OH. *J. Phys. Chem. A*, 2001. 105(18): p. 4446-4457.
22. Fenske, J.D., et al., OH Radical Yields from the Ozone Reaction with Cycloalkenes. *J. Phys. Chem. A*, 2000. 104(31): p. 7246-7254.
23. Ernestoc. Tuazon, Saramaschmann, Janetarey, and Roger Atkinson, Products of the Gas-Phase Reactions of O<sub>3</sub> with a Series of Methyl-Substituted Ethenes. *Environ. Sci. Technol.*, 1997. 31: p. 3004-3009.
24. Atkinson, R., Gas-phase tropospheric chemistry of volatile organic compounds: 1. alkanes and alkenes. *J. Phys. Chem. Ref. Data*, 1997. 26(2): p. 215-290.
25. Hakola, H., et al., Product formation from the gas-phase reactions of OH radicals and O<sub>3</sub> with a series of monoterpenes. *J. Atmos. Chem.*, 1994. 18(1): p. 75-102.
26. Liu, Y.M.-C., Rodrigo; Hargrove, James; Medina, David; Zhang, Jingsong Measurements of Peroxy Radicals Using Chemical Amplification-Cavity Ringdown Spectroscopy. *Environmental Science & Technology*, 2009. 43(20): p. 7791-7796.

27. Martinez, R.I., J.T. Herron, and R.E. Huie, The mechanism of ozone-alkene reactions in the gas phase. A mass spectrometric study of the reactions of eight linear and branched-chain alkenes. *Journal of the American Chemical Society*, 1981. 103(13): p. 3807-3820.
28. Clay, M.A., Bruce S., Infrared Matrix Isolation and Theoretical Study of the Initial Intermediates in the Reaction of Ozone with *cis*-2-Butene *Journal of Physical Chemistry A*, 2010. 114(8): p. 2799-2805.
29. Martinez Ri, H.J., stopped-flow study of gas-phase reaction of ozone with organic sulfides - dimethyl sulfide. *International journal of chemical kinetics*, 1978. 10(5): p. 433-452.
30. Morris Ed, s.d., Niki H, Mass spectrometric study of reactions of hydroxyl radical with ethylene, propylene, and acetaldehyde in a discharge-flow system. *Journal of the American Chemical Society*. *Journal of the American Chemical Society*, 1971. 93(15): p. 3570.
31. Hinrichs Ta, R.V., Murray Rw., Epoxidation of olefins with carbonyl oxides. *Journal of the American Chemical Society*, 1979. 101(5): p. 1282-1284.
32. Herron, R.I.M.a.J.T., Stopped-Flow Studies of the Mechanisms of Ozone-Alkene Reactions in the Gas Phase: *trans*-2-Butene. *J. Phys. Chem.*, 1988. 92: p. 4644-4648.
33. Hatakeyama, S., et al., Ozone-cyclohexene reaction in air: quantitative analysis of particulate products and the reaction mechanism. *Environ. Sci. Technol.*, 1985. 19(10): p. 935-42.

34. Kalberer, M., et al., Aerosol Formation in the Cyclohexene-Ozone System. Environ. Sci. Technol., 2000. 34(23): p. 4894-4901.
35. Ziemann, P.J., Evidence for Low-Volatility Diacyl Peroxides as a Nucleating Agent and Major Component of Aerosol Formed from Reactions of O<sub>3</sub> with Cyclohexene and Homologous Compounds. J. Phys. Chem. A, 2002. 106(17): p. 4390-4402.
36. Aschmann, S.M.T., Ernesto C.; Arey, Janet; Atkinson, Roger, Products of the Gas-Phase Reaction of O<sub>3</sub> with Cyclohexene. Journal of Physical Chemistry A, 2003. 107(13): p. 2247-2255.

# **Chapter 6 Study of gas Initial steps of phase ozonolysis of isoprene using VUV photoionization time-of-flight mass spectrometry**

## **Abstract**

Isoprene is a significant anthropogenic and biogenic VOC which related to secondary organic aerosol (SOA) abundance. Ozone-isoprene reactions are significant removal processes of isoprene in the troposphere and generation processes of SOA. To detect the transient early reactive intermediates and investigate the mechanisms of initial steps of ozonolysis of isoprene, a series of experiments are carried out in a fast flow reactor under the conditions of low pressure (7-10 Torr) and room temperature. CO is used as an OH scavenger to minimize the reactions between the OH byproduct and isoprene. After a short reaction time of ~25 – 200 ms, the initial products, both free radical intermediates and stable species, are sampled into a supersonic molecular beam and directly detected by 118-nm vacuum ultra-violet (VUV) photoionization time-of-flight mass spectrometry (TOFMS). Mass peaks corresponding to the Criegee intermediates or their isomers are identified. The isoprene-ozone reactions with longer reaction time

(up to 10 s) and 1 atm pressure are also carried out and studied. A general trend in the mass spectra and the reaction mechanisms are discussed.

## 6.1. Introduction

Isoprene (2-methyl-1,3-butadiene, C<sub>5</sub>H<sub>8</sub>) is a significant anthropogenic and biogenic volatile organic compounds (VOC), a flux accounting for about one third of the total anthropogenic and natural emission VOCs [1]. In the atmosphere, It is a short-lived compound ( $\tau_{1/2}=1 - 2$ h) emitted by many deciduous trees during daylight hours, therefore, isoprene plays a crucial role in determining the oxidative chemistry of the troposphere.

A substantial portion of the atmospheric oxidation of all alkenes is due to reaction with ozone; hence, an accurate description of both urban and rural ozone formation requires an understanding of the ozone-alkene reaction. In this case, the study of O<sub>3</sub> with isoprene is critical, however, although the reaction has been studied for decades, there is no available information for the initial several steps for this reaction and no direct observation for demonstrating the possible mechanism.

The ozonolysis reaction of isoprene is the same as the ozonolysis of other alkene reaction which are thought to proceed *via* the formations of 5-membered ring compounds (primary ozonide, POZ) which formed by initial addition of O<sub>3</sub> across

the C=C unsaturated bond to form an energy rich primary ozonide, The highly energized POZs undergo (a) direct decomposition into a carbonyl oxide (Criegee intermediate, CI) and a carbonyl product, or (b) non-concerted decomposition, followed by 1,4-hydrogen shift[2-7]. The detail mechanisms for ozone and alkene reactions have been discussed in Chapter 5, which will be briefly mentioned here. The CI can undergo collisional stabilization [reaction (5-2a)], isomerization to a “hot” hydroperoxide followed by breakage of the O-OH bond to form an OH radical plus a substituted alkyl radical [the “hydroperoxide channel,” reaction (5-2b)] [5, 8, 9], rearrangement to a “hot” ester with subsequent decomposition [the “ester channel,” reaction (5-2c)], or elimination of an O (<sup>3</sup>P) atom [reaction (5-2d)].

We have undertaken to examine the free radicals as well as carbonyl production from the isoprene ozonolysis reactions in an effort to delineate the mechanism. We have carried out a series of experiments under different conditions of ozone isoprene reactions with and without the addition of CO which served as the OH scavenger. We have focused on identifying and quantifying even relatively minor products to understand the reaction pathways of the Criegee biradicals.

## 6.2 Experimental

The experiments were carried out in the same reactor as other alkene and ozone reaction described in Chapter 2 and Chapter 5. The gas phase reactions were studied in a homemade fast flow reactor coupled with a VUV photoionization time-of-flight mass spectrometry (TOFMS) through a 0.26 mm sampling orifice. The configuration of the fast flow reactor and TOFMS has been described in Chapter 2, which consisted of a fast flow reactor, in which radicals and products are generated and reacted, and a linear TOFMS, in which radicals and products are detected.

Isoprene (Aldrich chemical company 99%) was diluted in Helium, without additional purification. This was accomplished by bubbling the Helium noble carrier gas through the liquid at dry ice/acetone bath temperatures. The CO gas passed first through an iodated charcoal filter to remove impurities such as carbonyl complexes in the CO gas cylinder [11]. The flow rate of CO (99.999%, Airgas Inc.) as an OH – scavenger was around 100 mL/min in the ozone-isoprene system. Occasionally, to ensure enough CO was involved in the reaction, larger flow rate of CO (up to 150 mL/min) was used. As shown in Figure 2-2, CO was introduced into the system using the same inlet with isoprene/He gas mixture. Ozone was generated by static electric discharge of oxygen gas from an ozone generator (Welsbach T408, ~ 5% O<sub>3</sub>



in O<sub>2</sub>). The O<sub>3</sub>-O<sub>2</sub> mixture from the ozone generator was passed through a silica gel trap at acetone-dry ice temperature, and O<sub>3</sub> is adsorbed on the silica gel. O<sub>3</sub> is then carried out by passing zero air carrier gas through the silica gel trap. Ozone was then introduced into the system as an encounter flow with alkene and CO flow. All the flowrates were controlled precisely by needle valves and monitored by mass flow meter (Aalborg). The concentration of isoprene was  $1.11 \times 10^{14}$  molecule /cm<sup>3</sup>. The zero air flowrate was 200ml/min for carrying ozone; and the flowrate for He bubbling through isoprene was 4ml/min. Under these conditions, the initial concentration of O<sub>3</sub> was about about  $2 \times 10^{15}$  -  $1 \times 10^{16}$  molecules /cm<sup>3</sup> in order to achieve the consumption of ~20% - 80% of isoprene in the presence of excess ozone. The reaction system pressure (line A) was 10 Torr with CO on and 8 Torr with CO off, and when the CO was on, the concentration of CO was  $7 \times 10^{16}$  molecule /cm<sup>3</sup>, which allowed 630 times of isoprene concentration.

The operation conditions for this experiment were similar to other ozone and alkene reactions (Chapter 5), which allowed us to monitor the products and the intermediates of the initial 25 - 28ms reaction time. The short reaction time before the products passing through the 0.26mm orifice allowed initial steps of ozone-isoprene reactions to be detected by TOFMS.

The longer reaction time (10s) and 1 atm experiments were carried out using a pulse valve for the study of ozone and isoprene reactions as well, and the results are also discussed.

### **6.3 Results**

As all the other alkene-ozone reactions we studied, prior to any experiments, blank experiments and background experiments were run first. These blanks served as reference mass spectra of the pure starting reactants, allowing for the clear identification of product mass peaks when they appeared. By comparing and analyzing the blank and background experiments results, product mass peaks can be identified accurately and clearly.

The mass spectra of this experiment are shown in Figure 6-1 and listed in Table 6-1. We attempt to assign each observed peak in the mass spectra to a reaction product or to a fragment ion arising from a product or parent. The number of possible isomeric species or species of the same nominal mass corresponding to any given mass spectral peak makes identification on the basis of mass spectra alone difficult, but by referring our previous studies on the reactions between ozone and

cis-2-butene, TME and cyclohexene, the identification of products can be supported and general mechanism can be proposed.

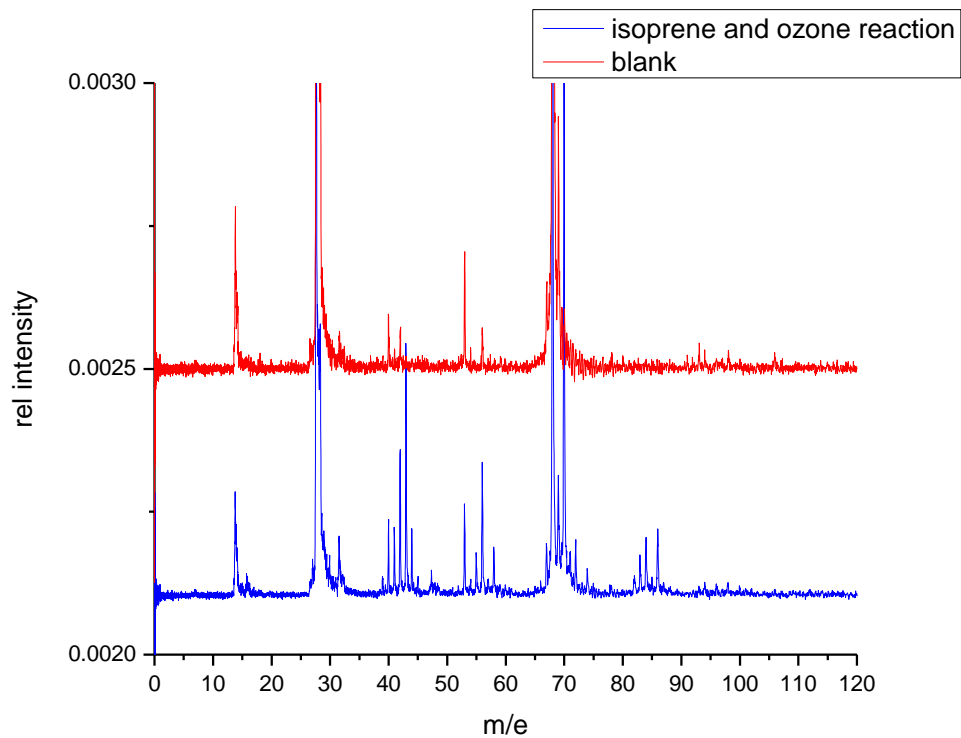
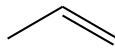
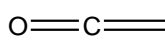
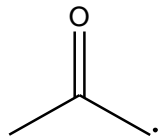
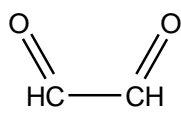
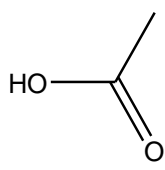
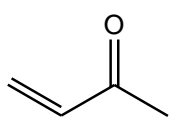
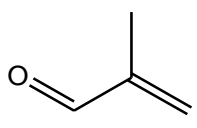
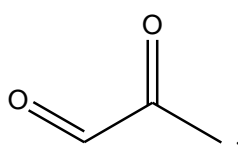
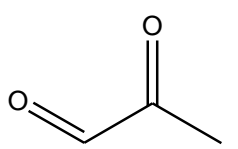
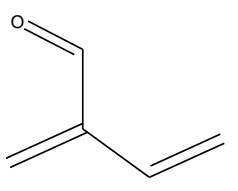
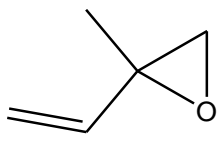
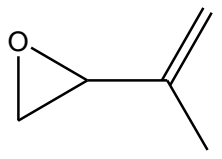
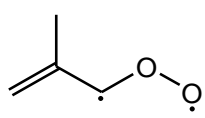


Figure 6- 1 Mass spectrum of ozone isoprene reaction compared with blank spectrum

Table 6- 1. Mass spectrum of ozone plus isoprene

m/e	Intensity: CO off	Compared intensity: CO on	possible assignments	possible structure
14 and 28			N <sup>+</sup> and N <sub>2</sub> <sup>+</sup>	
16 and 32			O <sup>+</sup> and O <sub>2</sub> <sup>+</sup>	
30	w		HCHO	
39	w		parent related	
40	m		parent related	
41	m			CH <sub>3</sub> -C =CH <sub>2</sub>
42	s		propene or ketene	 Or 
43	s		CH <sub>2</sub> CHO	
44	m		CH <sub>3</sub> CHO	
47	w			
53	s		parent related	
54	w		parent related	
55	m	decrease	CH <sub>2</sub> CCHO	
56	s		CH <sub>2</sub> CHCHO	CH <sub>2</sub> =CH-CHO
57	w			
58	m		H <sub>2</sub> C <sub>2</sub> O <sub>2</sub>	
60	w		CI or Acetic Acid	CH <sub>3</sub> CH-O-O or 
67			parent related	
68			parent related	

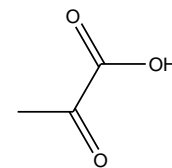
69		parent related	
70	vs	MVK MACR	
71	m		
72	s	methylglyoxal	
74	m	$C_3H_6O_2$	
78	w		
82	m	$CH_2CHC(CH_2)CHO$	
83	m	$CH_2CH_2C(CH_2)CHO$	
84	s	2-ethenyl 2-methyl oxirane or 2-(1-methylethenyl) oxirane	 or 
85	w		
86	s	CI	



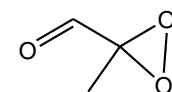
87 w

88 w

pyruvic acid



or



93 w

impurity

94 w

impurity

96 w

impurity?

98 w

decrease

$[R^1C(O)C(O)R^2]$

100 w

decrease

$R^1C(O)CH(OH)R^2$

102 w

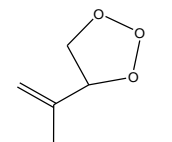
$R^1CH(OH)CH(OH)R^2$

Secondary ozonides

116 vw

of

and



(For peak intensity, w=weak, m=medium, s=strong, v=very )

The first step for the ozone-alkene reaction is the addition of ozone to form 5 member ring on C=C bond, which is primary ozonide. The primary ozonide has high energy and unstable, so it falls apart into CI and carbonyl product. Figure 6-2 illustrates the likely unimolecular reaction pathways of the primary ozonide and carbonyl oxide, respectively.

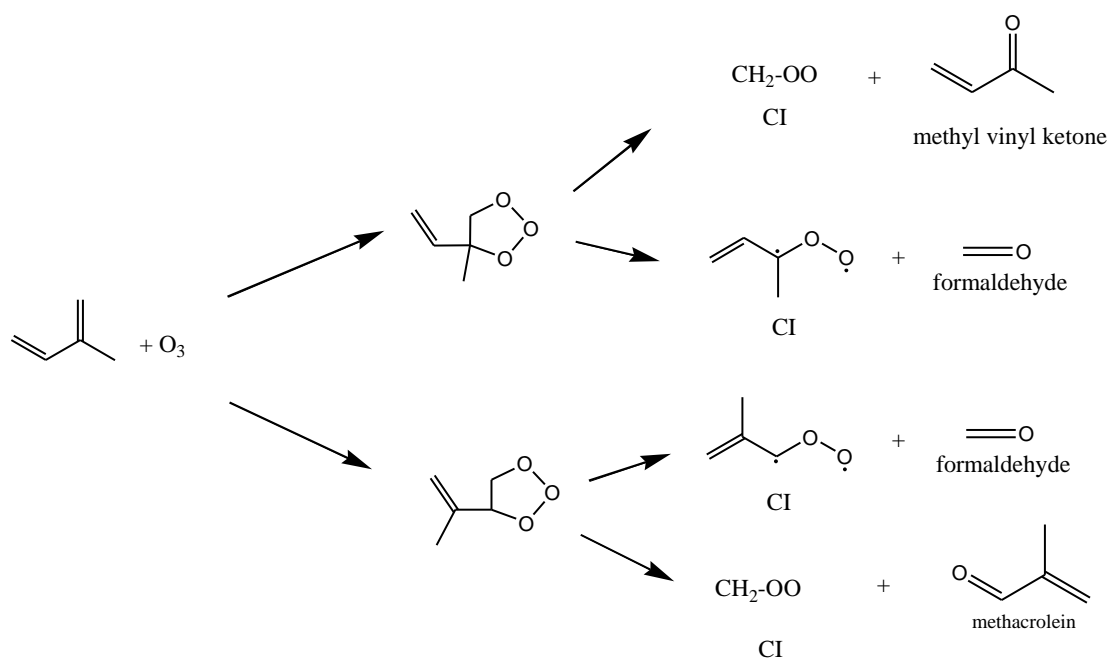
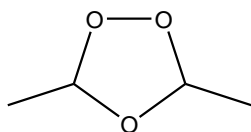


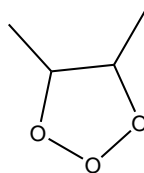
Figure 6-2 . Ozone and isoprene reaction initial path ways [12]

However, the CI and carbonyl product might combine to form secondary ozonide under higher pressure. Since both of the primary and the secondary ozonide compounds have same m/e (116), they can not be distinguished in the mass

spectrum. In this experiment, since POZ has very high energy and easy to fall apart, we assume it is SOZ instead of POZ.



primary ozonide

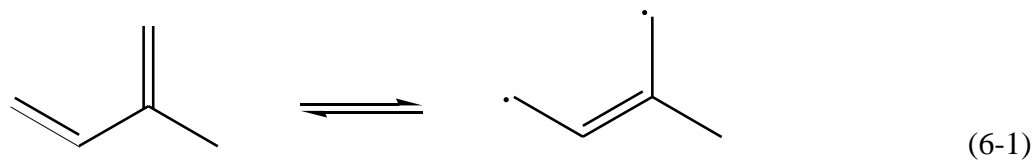


secondary ozonide

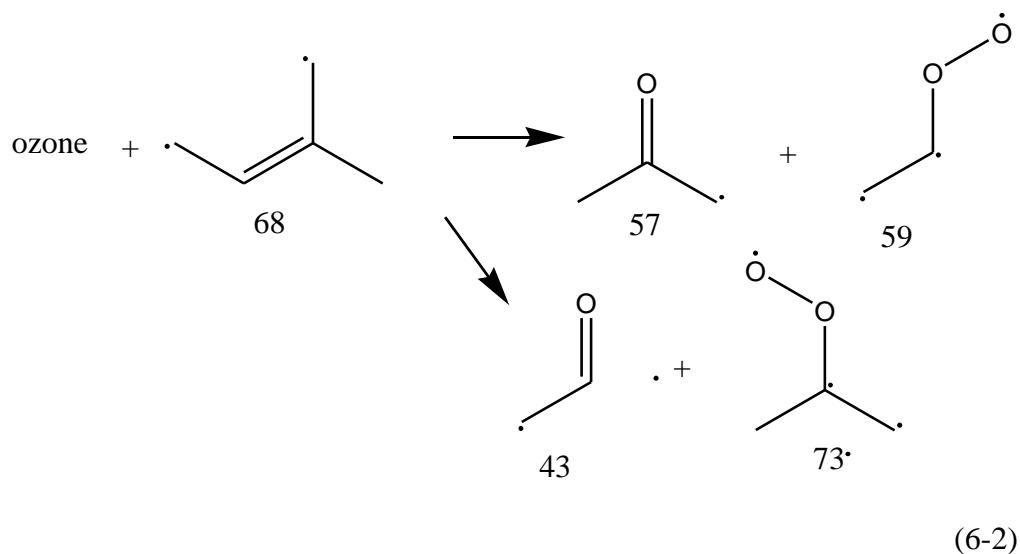
The most important initial step of the ozonation reaction is the decomposition of the primary ozonide, yielding a chemically activated carbonyl oxide (the Criegee intermediate, CI) and an aldehyde/ketone, shown in Figure5-2. In this case, the  $m/e$  30 peak due mainly to formaldehyde and the  $m/e$  70 peak includes methyl vinyl ketone (MVK), or methacrolein (MACR) and is unlikely to possess sufficient energy for further degradation. But they may react with excess ozone through similar reaction channel and form methylglyoxal which has  $m/e$  peak 72. And we believe that peak  $m/e$  71 should be related to this strong 72 peak. Peak  $m/e$  88 contributes to pyruvic acid, which comes from the ozonolysis of MVK [13]

The Criegee intermediate ( $m/e=86$ ) is an energy-rich compound and can easily fall apart. Peak 86 might also be dioxiranes. It has four isomers which are showed in Table 6-1. Since isoprene is conjugated diene, it has resonance isomers:

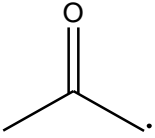




So we assume that another mechanism might be the reaction between  $O_3$  with the resonance of isoprene.



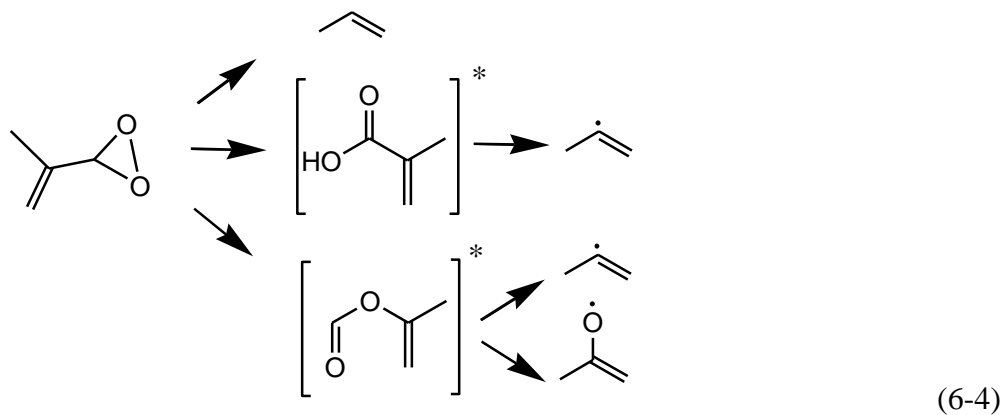
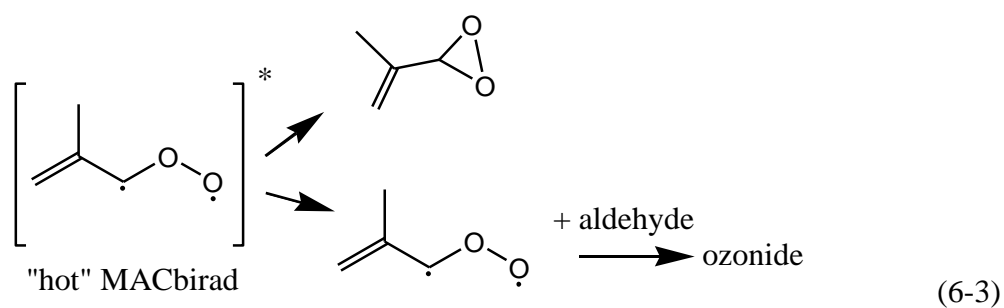
In these reaction paths, there are some unstable radicals and they rearrange and react very fast to form other intermediates. Peak  $m/e$  57 is partially from this reaction (6-2) and peak  $m/e$  56 is  $CH_2=CH-CHO$  which comes from  $CH_3$  shift from

peak 57 product ; or it might be from CI peak  $m/e$  73 (reaction (6-2)) losing an OH group. Peak 55 might be related to this 56 peak, which could be assigned to  $CH_2CCHO$ . And peak 58 might also come partially from H adding to the

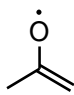
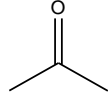
peak 57 product. Similarly, peak m/e 43 contributes to vinyloxy radical ( $\text{CH}_2\text{CHO}$ ) coming from reaction (6-2).

Peaks 39, 40, 53, 54, 67, 68, 69 are parent related and they could serve as a reference for the progress of the reaction.

Rearrangement of the “hot” biradical complement of MACR to form a dioxirane intermediate or a stable biradical, which can further react to form an ozonide is shown in reaction (5) [14]. Dioxirane compound in reaction (5) should rearrange and decompose according to the scheme shown in reaction (6) [14]



Inspection of the final products proposed for reaction (10) indicates that ketene may later evolve through molecular oxygen reactions and fragmentation. So peak m/e 42 contributes to propene and ketene and peak m/e 41 is  $\text{CH}_3\text{-C}=\text{CH}_2$  from

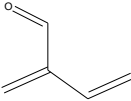
reaction (6). Similarly, peak m/e 57 also comes from  in addition to  mentioned above.

Pervious work [14] demonstrated that approximately 10-20% of the dioxirane compound would have to decompose to satisfy the propylene yields. As a predominated product, propylene continues to react with excess ozone, which is similar to the pathways suggested by us for the cyclohexene-ozone reactions (Chapter 4). In this case, the m/e 44 peak due mainly to ethanal, it also includes a contribution from oxirane. The Criegee intermediate ( $\text{CH}_3\text{CH-O-O}$ , m/e=60) is energy-rich and fall apart. It can lose an OH group to form  $\text{CH}_3\text{CO}$  (m/e=43) radical. Or it could rearrange into the acetic acid.

The glyoxal (m/e 58) is a unique and important indicator for the hydroperoxide channel of CI. For the  $\text{C}_n\text{H}_{2n}$  alkenes, it has been well explained and indicated that  $\text{C}_m$  dioxoalkanes and  $\text{C}_m$  ketenes, where  $m < n$ , originated from the primary, excited dioxymethylene via its isomerization to the hydroperoxide. For example, ketene and glyoxal are  $\text{C}_m$  products of alkenes containing the  $\text{CH}_3\text{C(H)=}$

moiety, while methylketene and methylglyoxal (peak 72) are  $C_m$  products of alkenes containing, respectively, the  $CH_3CH_2C(H)=$  and  $(CH_3)_2C=$  moieties. In this reaction, the glyoxal peak should come from the ozonolysis of propylene.

Peak 82 is the  $R(\text{alkene}) + 14$  peak, which was also discussed in previous work [15].  $R + 14$  peaks corresponds to  $C_n$ - substituted ketenes and/or  $C_n$  conjugated

oxoalkenes. Here, this peak is . And peak  $m/e$  83 is its radical which has one H added on the conjugated  $\pi$  bond.

The peak at  $m/e$  84 is due to 2-ethenyl 2-methyl oxirane and 2-(1-methylethenyl) oxirane. Epoxides and oxoalkanes arising from the parent alkene are known to be the products of solution phase ozonation of alkenes. Based on the discussion of Martinez [15], we conclude that under our experimental conditions, these epoxides and oxoalkanes arise from a primary ozonation reaction which has been discussed in Chapter 5.

Peak  $m/e$  85 is weak and it might be related to the strong peak of 84 or the adduct product of isoprene react with OH.

A particular set of peaks is the triplet at  $m/e$  98, 99, and 102, lying 30, 32, and 34 mass units up from the  $C_nH_{2n}$  alkene, which are found in all ozone-alkene reaction mass spectra, and have been discussed by previous works. It is believed that these are due respectively to  $C_n$ , dioxoalkanes [ $R'C(O)C(O)R''$ ],  $C_n$ , acyloins

[oxoalkanols,  $R'C(O)CH(OH)R''$ ], and  $C_n$ , alkanediols [ $R'CH(OH)CH(OH)R''$ ] which are probably formed via a complex sequence of reactions initiated by reaction of hydroxyl radicals with the alkene[16] (Chapter 4). Those products peaks are suppressed by CO scavenger.

## 6.4 Conclusion

Direct observation of ozonolysis of isoprene is reported. A fast flow reactor coupled with VUV-TOFMS was used to isolate and observe the initial reaction products, both free radical intermediates and stable species. CO has been used as an OH scavenger to eliminate the reaction between OH and alkenes and the difference between the results with and without CO is discussed. Under short reaction time conditions, it is possible to identify Criegee intermediates and all the early products and intermediates. Isoprene-ozone reactions with longer reaction time (up to 10 s) and 1 atm pressure were also carried out and studied. The mechanism of these reactions we proposed is in a good agreement with previous studies, and more products are observed and new mechanism has been proposed and discussed as well.

**Reference:**

1. Guenther, A., et al., Estimates of global terrestrial isoprene emissions using MEGAN (Model of Emissions of Gases and Aerosols from Nature). *Atmos. Chem. Phys.*, 2006. **6**(11): p. 3181-3210.
2. Calvert, J.G., et al., *The Mechanisms of Atmospheric Oxidation of the Alkenes*. 2000, New York: Oxford University Press. 560 pp.
3. Hatakeyama, S. and H. Akimoto, Reactions of Criegee intermediates in the gas phase. *Res. Chem. Intermed.*, 1994. **20**(3-5): p. 503-24.
4. O'Neal, H.E. and C. Blumstein, Nonconcerned Decomposition. *Int. J. Chem. Kinet.*, 1973. **5**: p. 397.
5. Fenske, J.D., et al., Measurement of Absolute Unimolecular and Bimolecular Rate Constants for CH<sub>3</sub>CHOO Generated by the trans-2-Butene Reaction with Ozone in the Gas Phase. *J. Phys. Chem. A*, 2000. **104**(44): p. 9921-9932.
6. Anglada, J.M., R. Crehuet, and J.M. Bofill, The ozonolysis of ethylene: A theoretical study of the gas-phase reaction mechanism. *Chemistry-a European Journal*, 1999. **5**(6): p. 1809-1822.

7. Harding, L.B. and W.A.I. Goddard, Mechanism of gas-phase and liquid-phase ozonolysis. *Journal of the American Chemical Society*, 1978. **100**(23): p. 7180-7188.
8. Kroll, J.H., et al., Mechanism of HO<sub>x</sub> Formation in the Gas-Phase Ozone-Alkene Reaction. 1. Direct, Pressure-Dependent Measurements of Prompt OH Yields. *J. Phys. Chem. A*, 2001. **105**(9): p. 1554-1560.
9. Kroll, J.H., et al., Mechanism of HO<sub>x</sub> formation in the gas-phase ozone-alkene reaction. 2. prompt versus thermal dissociation of carbonyl oxides to form OH. *J. Phys. Chem. A*, 2001. **105**(18): p. 4446-4457.
10. Lubman, D.M. and R.M. Jordan, Design for improved resolution in a time-of-flight mass-spectrometer using a supersonic beam and laser ionization source. *Review of Scientific Instruments*, 1985. **56**(3): p. 373-376.
11. Liu, Y.M.-C., Rodrigo; Hargrove, James; Medina, David; Zhang, Jingsong Measurements of Peroxy Radicals Using Chemical Amplification-Cavity Ringdown Spectroscopy. *Environmental Science & Technology*, 2009. **43**(20): p. 7791-7796.
12. Paulson, S.E., R.C. Flagan, and J.H. Seinfeld, Atmospheric Photooxidation of Isoprene .2. the Ozone-Isoprene Reaction. *International journal of chemical kinetics*, 1992. **24**(1): p. 103-125.

13. Paulot, F., et al., Isoprene photooxidation mechanism: resonance channels and implications for the production of nitrates and acids. *Atmos. Chem. Phys. Discuss.*, 2008. **8**(4): p. 14643-14716.
14. Kamens, R.M., et al., Ozone–isoprene reactions: Product formation and aerosol potential. *International Journal of Chemical Kinetics*, 1982. **14**(9): p. 955-975.
15. Martinez, R.I., J.T. Herron, and R.E. Huie, The mechanism of ozone-alkene reactions in the gas phase. A mass spectrometric study of the reactions of eight linear and branched-chain alkenes. *Journal of the American Chemical Society*, 1981. **103**(13): p. 3807-3820.
16. Martinez Ri, H.R., Herron Jt, Products of the reaction of hydroxyl radicals with trans-2-butene in the presence of oxygen and nitrogen-dioxide. *Chem. Phys. Lett.*, 1980. **72**: p. 443.



# **Chapter 7 Study of gas Initial steps of phase ozonolysis of pinene using VUV photoionization time-of-flight mass spectrometry**

## **Abstract**

$\alpha$ -pinene and  $\beta$ -pinene have the highest global emission among the biogenic VOCs, and ozone and pinene reaction products lead to secondary organic aerosol (SOA) formation. To investigate the mechanism of early steps of ozonolysis of pinenes, a fast flow reactor is used to study the reactions under low pressure (7-10 Torr) and room temperature. CO is used as an OH scavenger to minimize the reactions between the OH byproduct and pinene. After a short reaction time of 20 ms to 200ms, the initial products, both free radical intermediates and stable species, are sampled into a supersonic molecular beam and directly detected by 118-nm vacuum ultra-violet (VUV) photoionization time-of-flight mass spectrometry (TOFMS). Mass peaks corresponding to the Criegee intermediates or their isomers are identified. A general trend in the mass spectra and the reaction mechanisms are discussed.

## 7.1 Introduction

Alkenes are the major class of volatile organic compounds (VOCs) emitted from vegetation [1] [2], and are also emitted from anthropogenic sources. In urban areas, alkenes (primarily from anthropogenic sources) comprise ~10% of nonmethane VOCs [1]. Terpenes account for a major fraction of the biogenic nonmethane VOCs [2, 3].  $\alpha$ -pinene and  $\beta$ -pinene are representative monoterpene among the diversity of emitted terpenes and accounts, together with limonene and sabinene, for the main fraction of the emitted terpenes [4]. Terpenes are oxidized in the troposphere by either OH, O<sub>3</sub>, or NO<sub>3</sub> and they play a crucial role in determining the oxidative chemistry of the troposphere.

A substantial portion of the atmospheric oxidation of pinenes is due to reaction with ozone, hence, an accurate description of both urban and rural ozone formation requires an understanding of the ozone - pinene reactions. Although ozone-alkene reactions have been studied for decades, many questions remain, particularly as to the fate of the Criegee biradicals in the gas phase [5]. Furthermore, although possible mechanisms for the generation of the products have been suggested, the overall understanding of the reaction mechanisms leading to condensable species is still inadequate [6]. In addition, although pinenes are very important VOCs, since their structure is complex, there is no available information for the initial several

steps for their ozonolysis reactions and no direct observation of the initial reactions intermediates for demonstrating the possible mechanisms.

The ozonolysis reactions of pinenes are the same as the ozonolysis of other alkene reactions which are thought to proceed *via* the formations of 5-membered ring compounds (primary ozonide, POZ). The POZs are formed by initial addition of O<sub>3</sub> across the C=C unsaturated bond to form an energy rich primary ozonide. The highly energized POZs undergo (a) direct decomposition into a carbonyl oxide (Criegee intermediate, CI) and a carbonyl product, or (b) non-concerted decomposition, followed by 1,4-hydrogen shift[7-12]. The detailed mechanisms for ozone and alkene reactions have been discussed in Chapter 5, which will be briefly mentioned here. The CI's are undergo collisional stabilization [reaction (5-2a)], isomerization to a "hot" hydroperoxide followed by breakage of the O-OH bond to form an OH radical plus a substituted alkyl radical [the "hydroperoxide channel," reaction (5-2b)] [10, 13, 14], rearrangement to a "hot" ester with subsequent decomposition (the "ester channel," reaction (5-2c)), or elimination of an O (<sup>3</sup>P) atom [reaction (5-2d)].

We have undertaken to examine the free radical as well as carbonyl production from the pinene ozonolysis reactions in an effort to delineate the mechanism for these reactions. We have carried out a series of experiments under

different conditions of the ozone and pinene reactions with and without the addition of CO, which is an OH scavenger. We have focused on identifying and quantifying even relatively minor products to understand the reaction pathways of the Criegee biradicals.

## 7.2. Experimental

The gas phase reactions were studied in a fast flow reactor coupled with a VUV photon ionization time-of-flight mass spectrometry (TOFMS) which has been described in Chapter 2 and Chapter 5. The experimental system was consisted of a fast flow plug flow reactor, in which ozone and pinene were reacted and radicals and products were generated, which were then sampled into the linear TOFMS (Model D-651, the R. M. Jordan Company [15]).

The pinene-ozone reactions have been carried in the experimental setup showed in Figure 2-2.  $\alpha$  or  $\beta$  - pinene (Aldrich chemical company 99%) was diluted in N<sub>2</sub>, without further purification. This was accomplished by bubbling the N<sub>2</sub> carrier gas through the liquid at ice/water bath temperatures (0 °C). The CO gas passed first through an iodated charcoal filter to remove impurities such as carbonyl complexes in the CO gas cylinder. The flow rate of CO (99.999%, Airgas Inc.) as an

OH – scavenger is ~100 mL/min in the ozone –pinene reactions. As showed in Figure 2-2, CO was introduced into the system using the same inlet with pinene/N<sub>2</sub> gas mixture. Ozone was generated by static electric discharge of oxygen gas from an ozone generator (Welsbach T408, ~ 5% O<sub>3</sub> in O<sub>2</sub>). The O<sub>3</sub>-O<sub>2</sub> mixture from the ozone generator was passed through a silica gel trap at acetone - dry ice temperature, and O<sub>3</sub> is adsorbed on the silica gel. O<sub>3</sub> was then carried out by passing air carrier gas through the silica gel trap, and introduced into the system as an encounter flow to the alkene and CO flow. All the flowrates were controlled precisely by needle valves and monitored by mass flow meters (Aalborg). The concentration of  $\alpha$  - pinene was  $3.50 \times 10^{14}$  molecule /cm<sup>3</sup>, while the concentration of  $\beta$  - pinene was  $2.75 \times 10^{14}$  molecule /cm<sup>3</sup>. The air flowrate is ~200 ml/min for carrying ozone, and the flowrate for CO as an OH scavenger was 100 ml/min. The reaction system pressure (line A) is 10 Torr with CO on and 8 Torr with CO off, and when the CO was on, the concentration of CO was  $\sim 7 \times 10^{16}$  molecule /cm<sup>3</sup> which allowed ~250 times of pinene concentration.

The reactor system has been described in Chapter 5 and shown in Chapter 2 (Figure 2 -2). The fast flow reactor was based on the design of Clay and Ault [16] and further modified by us, in which the ozone and pinene encounter in the reactor and were permitted to mix and react during passage through the flow reactor. The

velocity of the sample within the flow reactor was round 3500 cm/s which gave rise an approximate 20-100 ms residence time depending on different experiments. The short reaction time before the products passing through the 0.26 mm orifices allowed initial steps of ozone – isoprene reactions to detected by TOFMS. Upon exiting the orifice, the products and remaining reactants were cooled and isolated by supersonic expansion into a molecular beam where they proceeded to the photoionization region.

The longer reaction time (10s) and 1 atm experiments were carried out using pulse valve for the study of ozone and isoprene reactions as well and the results are also been discussed.

### **7.3. Results**

As all the other alkene – ozone reactions we studied, prior to any experiments, blank experiments and background experiments were run first. The mass spectrum and results of ozonolysis of  $\alpha$  and  $\beta$  – pinene experiments are shown in Figure 7-1 and Figure 7-2. Their mass spectrum peak assignments are listed in Table 7 -1 and Table 7 - 2. We attempt to assign each observed peak in these mass spectrums to a reaction product or to a fragment ion arising from a product or parent. Compared to

other alkene systems we investigated, both  $\alpha$  and  $\beta$  – pinenes have relatively low ionization energy ( $\sim 8$  eV). As a result, their ozonolysis products also have low ionization energy, which generate many fragments in the mass spectra. Besides, the number of possible isomeric species or species of the same nominal mass corresponding to any given mass spectral peak makes identification on the basis of mass spectra alone uncertain. Under this situation, it is relatively hard to identify every peak but by referring to our previous work on the reactions between ozone and cis-2-butene, TME, cyclohexene and isoprene and by comparing between  $\alpha$  and  $\beta$  – pinene, the identification of some of the most important products can be supported and general mechanism can be proposed.

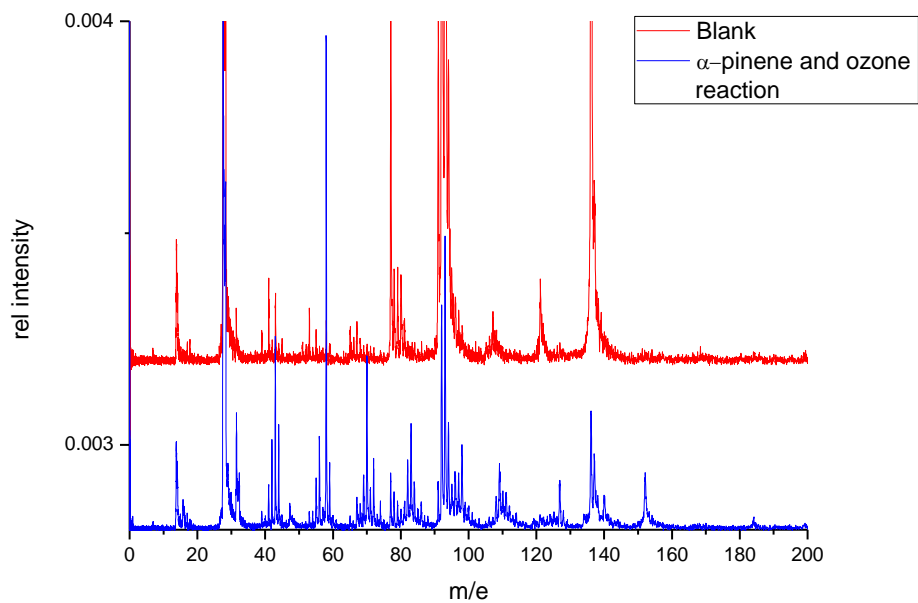


Figure 7- 1 Mass spectrum of ozone and  $\alpha$ -pinene reaction compared with blank spectrum

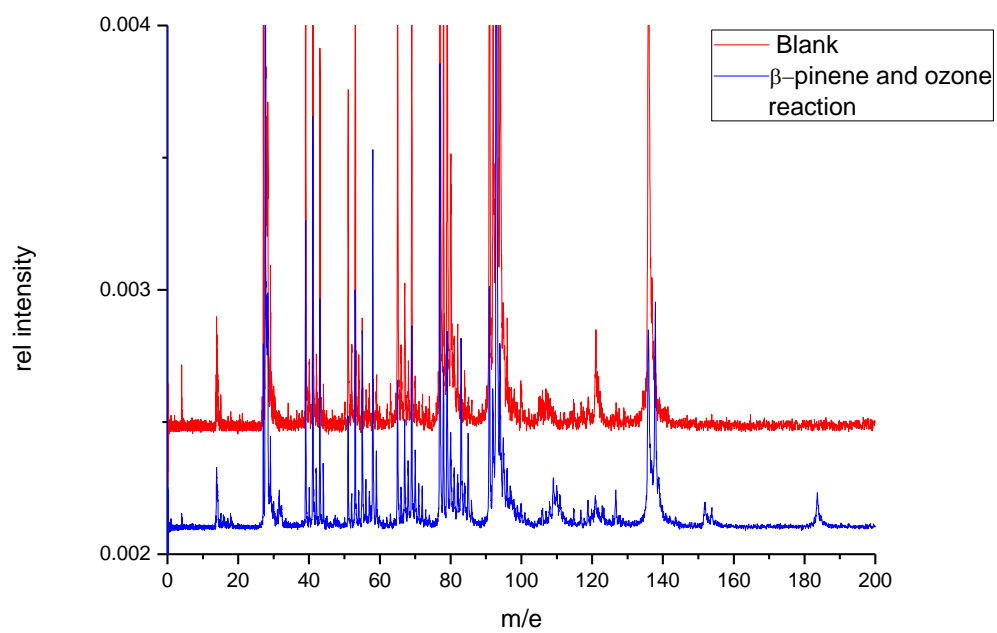




Figure 7- 2 Mass spectrum of ozone and  $\beta$ - pinene reaction compared with blank spectrum

Table 7 -1. Mass spectrum of ozone plus  $\alpha$ - piene peak assignment

m/e	Intensity:	possible assignments
42	s	Propene or Ketene
43	s	CH <sub>2</sub> CHO
44	s	CH <sub>3</sub> CHO
58	vs	Glyoxal
59	m	Glyoxal related
72	s	methylglyoxal
136	s	parent
137	m	Oxirane fragment
140	m	CI lost CO <sub>2</sub>
152	s	oxirane
184	m	POZ or SOZ or CI

(For Peak intensity, w=weak, m=medium, s=strong, v=very )

Table 7 - 2. Mass spectrum of ozone plus  $\beta$  - piene peak assignment

m/e	Intensity:	possible assignments
42	m	Propene or Ketene
43	s	CH <sub>2</sub> CHO
44	s	CH <sub>3</sub> CHO
58	vs	Glyoxal
59	m	Glyoxal related
123	m	138 peak lost CH <sub>3</sub> fragment
136	s	parent related
137	m	Oxirane lost CH <sub>3</sub> fragment
138	m	6,6-dimethylbicyclo[3.1.1]heptan-2-one
152	s	Oxirane
154	m	CI
184	m	POZ or SOZ

(For Peak intensity, w=weak, m=medium, s=strong, v=very )

The first step for the ozone – alkene reaction is the addition of ozone to form 5 number ring on C=C bond, which is the primary ozonide. The primary ozonide has high energy and it is unstable, so it falls apart into CI and carbonyl oxide. For  $\alpha$ -pinene, since the C=C bond is on the ring, when the POZ falls apart, it open the ring so the mass peak does not change. Meanwhile, for  $\beta$  – pinene, in which C=C bond is on the side chain, the POZs falls apart in to two parts. Therefore peak 138 is assigned to 6,6-dimethylbicyclo[3.1.1]heptan-2-one and peak 154 to CI or its isomers in the  $\beta$ -pinene ozonolysis reaction. Since 6,6-dimethylbicyclo[3.1.1]heptan-2-one is a stable compound, several of its ionization fragment can be identified in the  $\beta$ -pinene ozonolysis mass spectrum. In

addition, the CI and carbonyl oxide might recombine to form secondary ozonide and since both of the primary and the secondary ozonide compounds have same m/e (184), they can not be distinguished in the mass spectrum.

The most important product of the ozonation reaction is the decomposition of the primary ozonide yields a chemically activated carbonyl oxide (the Criegee intermediate, CI) and an aldehyde / ketone. The Criegee intermediate is an energy-rich compound and falls apart. It also can isomerize into dioxiranes. Then the dioxirane decomposes a CO<sub>2</sub> (m/e = 44) molecule which is where the 140 peak comes from in the  $\alpha$ -pinene ozonolysis reaction mass spectrum ( $184 - 44 = 140$ ), while there is no 140 peak in the  $\beta$ -pinene ozonolysis reaction mass spectrum. If the same process happens in the  $\beta$ -pinene ozonolysis reaction, the 6 member ring of the pinene will break. Although we also see medium intensity in the 110 peak ( $154 - 44 = 110$ ), the ring opening makes this process much more complicated and more fragments mass peaks might show up in the mass spectrum. In this case, the assignment for the m/e 110 peak is uncertain, and possibly more peaks in this mass spectrum are coming from this process in the  $\beta$ -pinene ozonolysis reaction.

As mentioned in the former chapters, the decomposition of CO<sub>2</sub> from CI makes the CI into smaller alkenes and the smaller alkenes will continue to react with O<sub>3</sub> to generate secondary reaction products. In consequence, the alkene series will get

even smaller when the reaction continues, and eventually relatively intense peaks of propene or ketene ( $m/e$  42),  $\text{CH}_2\text{CHO}$  ( $m/e$  43) and  $\text{CH}_3\text{CHO}$  are produced, which is similar to all the other alkene systems we have investigated and analyzed in previous chapters.

The peaks at  $m/e$  152 for both of the pinenes are due to oxirane. Epoxides and oxoalkanes arising from the parent alkene are known to be the products of the solution phase ozonation of alkenes. Based on the discussion for other alkene ozone reactions in the former chapters, we conclude that under our experimental conditions, these epoxides and oxoalkanes arise from a primary ozonation reaction.

The glyoxal ( $m/e$  58) is a unique and important indicator for the hydroperoxide channel of CI. For the  $\text{C}_n\text{H}_{2n}$  alkenes, it has been well explained and indicated that  $\text{C}_m$  dioxoalkanes and  $\text{C}_m$  ketenes, where  $m < n$ , originated from the primary, excited dioxymethylene via its isomerization to the hydroperoxide. For example, ketene and glyoxal are  $\text{C}_m$  products of alkenes containing the  $\text{CH}_3\text{C}(\text{H})=$  moiety, while methylketene and methylglyoxal (peak 72) are  $\text{C}_m$  products of alkenes containing, respectively, the  $\text{CH}_3\text{CH}_2\text{C}(\text{H})=$  and  $(\text{CH}_3)_2\text{C}=\text{}$  moieties.. This is why in the  $\alpha$  – pinene ozonolysis system, methylglyoxal peak and glyoxal peak are both intense, and in the  $\beta$  – pinene ozonolysis reaction, only the glyoxal peak is intense, while no methylglyoxal peak shows up.

## 7.4 Conclusion

Direct observations of ozonolysis of both  $\alpha$  – pinene and  $\beta$  – pinene are reported in this section. A fast flow reactor coupled with VUV-TOFMS is used to isolate and observe the initial reaction products, both free radical intermediates and stable species. CO has been used as an OH scavenger to eliminate the reaction between OH and alkenes. Under short reaction time conditions, it is possible to identify the Criegee intermediates or their isomers. The pinene ozonolysis mass spectra are much more complicated compare to other alkene ozone systems we have investigated due to their low ionization energy. However, by carefully analyzing the results and referring to general mechanism, some of the most important products can be identified, including the POZ or SOZ and CI or its isomer peaks, etc. The difference between the ozonolysis of  $\alpha$  – pinene and  $\beta$  – pinene is also discussed and the concluded mechanisms we proposed are in a good agreement with other work. This work provides valuable information for the early steps of gas phase products for pinene and ozone reactions and demonstrated the general trend in the mass spectra and the reaction mechanisms.

## Reference

1. Sara M. Aschmann, J.A., and Roger Atkinson, Kinetics and products of the reactions of OH radicals with 4,4-dimethyl-1-pentene and 3,3-dimethylbutanal at 296 +/- 2 K. *J Phys Chem A*, 2010 114(18): p. 5810.
2. Guenther, A., et al., A global model of natural volatile organic compound emissions. *J. Geophys. Res.*, 1995. 100(D5): p. 8873-8892.
3. Müller, J.-F., Geographical Distribution and Seasonal Variation of Surface Emissions and Deposition Velocities of Atmospheric Trace Gases. *J. Geophys. Res.*, 1992. 97(D4): p. 3787-3804.
4. Owen, S., et al., Screening of 18 Mediterranean plant species for volatile organic compound emissions. *Atmospheric Environment*, 1997. 31(Supplement 1): p. 101-117.
5. Atkinson, R., et al., Formation of hydroxyl radicals in the gas phase reactions of ozone with a series of terpenes. *J. Geophys. Res.*, [Atmos.], 1992. 97(D5): p. 6065-73.
6. Paulson, S.E., R.C. Flagan, and J.H. Seinfeld, Atmospheric Photooxidation of Isoprene .2. the Ozone-Isoprene Reaction. *International Journal of Chemical Kinetics* 1992. 24(1): p. 103-125.

7. Calvert, J.G., et al., *The Mechanisms of Atmospheric Oxidation of the Alkenes*. 2000, New York: Oxford University Press. 560 pp.
8. Hatakeyama, S. and H. Akimoto, Reactions of Criegee intermediates in the gas phase. *Res. Chem. Intermed.*, 1994. 20(3-5): p. 503-24.
9. O'Neal, H.E. and C. Blumstein, Nonconcerned Decomposition. *Int. J. Chem. Kinet.*, 1973. 5: p. 397.
10. Fenske, J.D., et al., Measurement of Absolute Unimolecular and Bimolecular Rate Constants for CH<sub>3</sub>CHOO Generated by the trans-2-Butene Reaction with Ozone in the Gas Phase. *J. Phys. Chem. A*, 2000. 104(44): p. 9921-9932.
11. Anglada, J.M., R. Crehuet, and J.M. Bofill, The ozonolysis of ethylene: A theoretical study of the gas-phase reaction mechanism. *Chemistry-a European Journal*, 1999. 5(6): p. 1809-1822.
12. Harding, L.B. and W.A.I. Goddard, Mechanism of gas-phase and liquid-phase ozonolysis. *Journal of the American Chemical Society*, 1978. 100(23): p. 7180-7188.
13. Kroll, J.H., et al., Mechanism of HO<sub>x</sub> Formation in the Gas-Phase Ozone-Alkene Reaction. 1. Direct, Pressure-Dependent Measurements of Prompt OH Yields. *J. Phys. Chem. A*, 2001. 105(9): p. 1554-1560.



14. Kroll, J.H., et al., Mechanism of HO<sub>x</sub> formation in the gas-phase ozone-alkene reaction. 2. prompt versus thermal dissociation of carbonyl oxides to form OH. *J. Phys. Chem. A*, 2001. 105(18): p. 4446-4457.
15. Lubman, D.M. and R.M. Jordan, Design for improved resolution in a time-of-flight mass spectrometer using a supersonic beam and laser ionization source. *Review of Scientific Instruments*, 1985. 56(3): p. 373-376.
16. Clay, M.A., Bruce S., Infrared Matrix Isolation and Theoretical Study of the Initial Intermediates in the Reaction of Ozone with cis-2-Butene *Journal of Physical Chemistry A*, 2010. 114(8): p. 2799-2805.

# Chapter 8 Measurement of aerosol optical extinction using diode laser cavity ringdown spectroscopy

## Abstract

Accurate measurement of the optical extinction of atmospheric aerosols is important for quantifying the direct climate effects of aerosols. A portable cavity ringdown spectrometer utilizing a modulated multimode blue diode laser (linewidth  $\sim 0.2$  nm) is developed to measure the aerosol optical extinction. Laboratory generated ammonia sulfate particles ( $< 1$   $\mu\text{m}$  in diameter) are characterized, with good agreements between the experimental measurements and Mie theory calculations. An optical extinction detection sensitivity of  $0.24$   $\text{Mm}^{-1}$  ( $1\sigma$ ) is achieved. Measurement of the ambient aerosols is also carried out. This study demonstrates the feasibility of compact, multimode diode laser cavity ringdown spectrometer for sensitive measurement of the optical extinction of atmospheric aerosols.

## 8.1. Introduction

Atmospheric aerosols interact with solar radiation by extinction of light, which includes both scattering and absorption. In general, the atmospheric aerosols absorb weakly that their extinction is mainly due to scattering. The atmospheric aerosols can directly influence the climate by heating up the atmosphere aloft on one hand, and by reducing surface irradiance on the other hand. They can also alter the properties of clouds and thus indirectly influence the climate in the atmosphere [1].

When a light beam illuminates on aerosol particles, a portion of the light beam is scattered and absorbed by the particles; thereby the intensity of the light beam is attenuated along the optical axis. The intensity of light that traverses the aerosols,  $I$ , is given by the Beer's law,

$$I = I_0 \exp(-\sigma_e l) \quad (8-1)$$

where  $I_0$  is the intensity of incident light,  $\sigma_e$  is the aerosol extinction coefficient, and  $l$  is the optical path length of the light through the aerosols. For mono-dispersed aerosols of a number density of  $N$  particles per unit volume, the aerosol extinction coefficient  $\sigma_e$  is given by [2]

$$\sigma_e = \epsilon Q_e N \quad (8-2)$$

where  $\varepsilon$  is the geometrical cross section of the aerosol ( $\pi d^2/4$  for a spherical particle with a diameter  $d$ ), and  $Q_e$  is the particle extinction efficiency. The product of  $\varepsilon$  and  $Q_e$  is the extinction cross section of the aerosol particle. For poly-dispersed aerosols, the optical extinction  $\sigma_e$  is the sum of the extinction cross section of individual aerosol particle,  $\varepsilon Q_e$ .

$Q_e$  is of theoretical and analytical importance. It is the ratio of the radiation power scattered and absorbed by a particle to the radiation power geometrically incident on the particle. The  $Q_e$  value depends on the particle refractive index, and shape and size relative to the wavelength of light. The dependence on the particle size is expressed in a dimensionless size parameter  $x$ , which is the ratio of the particle diameter to the wavelength,  $\lambda$ , of the radiation light,

$$x = \pi d / \lambda \quad (8-3)$$

As the optical extinction includes both scattering and absorption, the extinction efficiency of a particle is the sum of its scattering efficiency  $Q_s$  and absorption efficiency  $Q_a$ ,

$$Q_e = Q_s + Q_a \quad (8-4)$$

Correspondingly, for mono-dispersed particles,

$$\sigma_e = \sigma_s + \sigma_a \quad (8-5)$$

where  $\sigma_s$  and  $\sigma_a$  are the aerosol scattering coefficient and absorption coefficient, respectively.

While all aerosol particles scatter light, only those composed of absorbing material would absorb, and this absorption is described by the imaginary part of the refractive index. For non-absorbing particles,  $Q_e = Q_s$ . For small spherical particles with  $d < 50$  nm,  $Q_s$  can be calculated using the Rayleigh scattering theory. For larger spherical particles ( $d > 50$  nm),  $Q_s$  can be obtained by the Mie theory calculations.

Although the optical extinction of atmospheric aerosols has been measured for decades, a better understanding of the aerosol optical properties is still needed. In particular, in situ measurements of the extinction and other optical parameters of atmospheric aerosols are crucial, and these require real-time, accurate, and sensitive techniques that can detect the ambient aerosols and their rapid temporal and spatial changes. Recent years have seen a rapid rise in the use of cavity ringdown spectroscopy (CRDS), a sensitive and direct optical extinction technique, to determine the optical properties of both laboratory generated and atmospheric ambient aerosols [3-17].

CRDS was first developed by O'Keefe and Deacon in 1988 [18] and utilized for spectroscopic measurements of gas species absorption [19]. The CRDS technique measures the rate, rather than the magnitude, of extinction of light in a highly reflective optical cavity that contains the trace sample [20]. The rate of decay of the trapped light is determined by the total cavity loss and sample absorption. The net decay rate as a function of laser wavelength yields the absorption spectrum of the sample. With  $\sim 10^4$  round trips of the trapped light, a long effective path ( $\sim 10$  km in a 1-m cavity) and thus high sensitivity are achieved. The CRDS technique is absolute, quantitative, and sensitive, and it is ideal for spectroscopic detection of atmospheric trace species. Many atmospheric species, such as  $\text{NO}_2$  [21] [22, 23],  $\text{NO}_3$  [24, 25],  $\text{SO}_2$  [26] and peroxy radicals [27], have been measured by CRDS.

Sappey et al. [3] and Smith and Atkinson [4] were among the first research groups to apply CRDS in aerosol extinction measurements and quantify the extinction of the ambient atmospheric particles. Many more studies have been subsequently carried out to measure the optical extinction of aerosol particles using CRDS [6-10]. Most of these previous works were based on using either a pulsed YAG laser, which is relatively bulky and limited to only 355, 532 or 1064 nm laser radiation [12-14], or a pulsed tunable dye laser, which is cumbersome and not suitable for field study [15]. The cw-CRDS using narrow linewidth diode laser in

visible (690 nm) [16] and near-IR (1550 and 1650 nm) [16, 17] was also utilized for the aerosol extinction measurements. However, these setups required complex electronics to control the optical cavity length and to modulate the diode laser output in order to couple the cw diode laser radiation into the cavity.

In this paper, a multimode diode laser CRDS system is reported for measurements of aerosol optical extinction. The utilization of the multimode, broadband diode laser (linewidth  $\sim 0.2$  nm) allows for a simple on-axis injection of the laser radiation into the cavity, while it still has a high spectral resolution for studying the aerosol optical properties. The multimode diode laser is inexpensive and compact, suitable for portable instruments. Furthermore, the increasing availability of the diode lasers at various wavelengths will allow simultaneous multiple wavelength measurements of the optical properties of aerosols, which can help determine the dispersion in the refractive index with high accuracy. This proof-of-principle work demonstrates the utilization of the multimode diode laser in the simple, inexpensive, and portable CRDS instrument for the laboratory and field studies of aerosols.

## 8.2. Experimental

### 8.2.1 The CRDS system

In a typical CRDS setup, laser pulses are injected and trapped in an optical cavity composed of two high-quality mirrors (with typical reflectivity  $R > 99.9\%$ ). In an empty cavity, the intensity of the trapped laser pulses decreases by a small percentage in each round trip due to mirror loss, decaying as an exponential function of time (with a decay time constant or ringdown time  $\tau_0$ ). When an extinction aerosol sample is present in the cavity, its scattering and absorption increase the loss, which can be determined from comparing the empty cavity ringdown time ( $\tau_0$ ) and the one with the analyte ( $\tau$ ) [18, 20]:

$$\sigma_e = \frac{L}{cl_s} \left( \frac{1}{\tau} - \frac{1}{\tau_0} \right) = \epsilon Q_e N \quad (8-6)$$

where  $L$  is the cavity length,  $l_s$  is the sample path length, and  $c$  is the speed of light. CRDS has the advantage of being insensitive to the fluctuation in laser intensity. It is a rapid, real-time technique, with individual ringdown events on the millisecond time scale. Another advantage is that the extinction aerosols can be removed from the air sample stream using a filter, and it is possible to obtain the optical extinction measurements without any calibration.



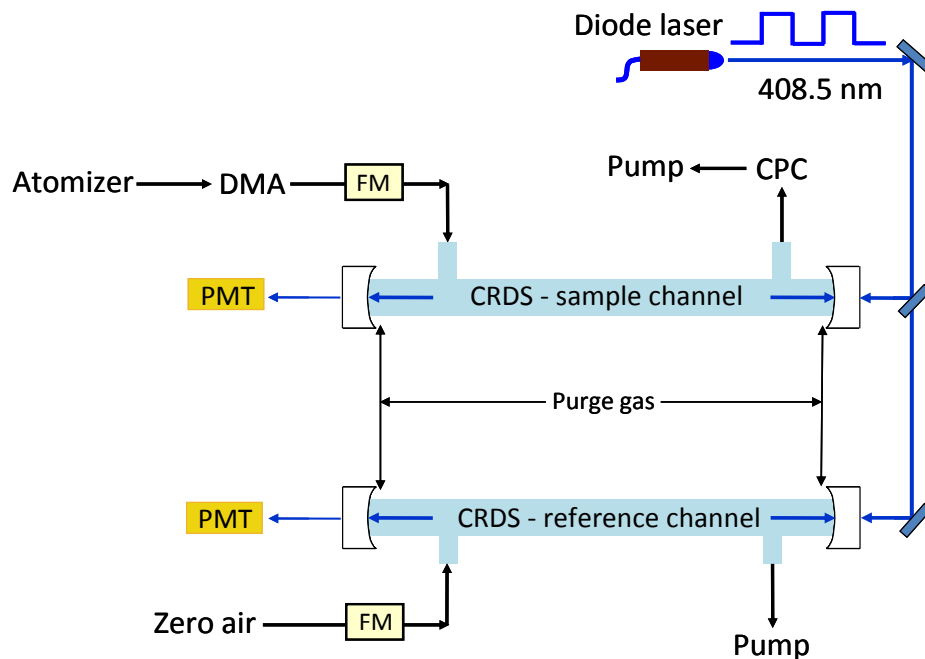


Figure 8- 1 Schematic diagram of the dual channel diode CRDS instrument for laboratory aerosol optical extinction measurements. FM = flow meter. DMA= deferential mobility analyzer. CPC = condensation particle counter.

In this work, a small blue diode laser was incorporated as the light source in a portable dual-channel CRDS spectrometer (Figure 8-1). The optical output from the diode laser (Sharp, 20 mW, multimode, 408.5 nm, ~0.2 nm FWHM linewidth) was amplitude modulated on and off with a square-wave voltage signal at a repetition rate of 2 kHz and a duty cycle of 50 %. With a beamsplitter and two turning mirrors,

the laser beams were injected into two ringdown cavities. Since the diode laser was multimode and broadband, the laser radiation can be directly coupled into and built up in the cavity, without any requirements for active matching of the laser modes to the resonant frequencies of the cavity or a scheme to increase the cavity mode density [23]. When the laser output was modulated off, the light intensity in the cavity decayed exponentially, providing the ringdown time measurements. The aerosol optical extinction can be obtained from the time constants with ( $\tau$ ) and without ( $\tau_0$ ) the aerosols present in the cavity using eqn (8-6). Two CRDS channels were used in the spectrometer. A reference channel monitored the gas-phase background (with the aerosols removed by a filter), and a sample channel measured the background plus the optical extinction of the particles. The difference between these two channels gave the aerosol optical extinction. This approach is particularly useful for the ambient measurements, in which the gas-phase background can be monitored and removed in real time, providing enhanced sensitivity and time resolution. To demonstrate this approach, the diode laser was chosen at the near-UV wavelength 408.5 nm where the ambient  $\text{NO}_2$  absorbs. For multiple wavelength measurements, diode lasers can also be selected to avoid or minimize the gas phase background.

Both cavity ringdown cells consisted of a pair of high-reflectivity mirrors (Los Gatos,  $R \approx 99.98\%$ , 2.54 cm diameter, 1.0 m radius of curvature) separated at 86 cm. The ringdown time constant was measured as  $\sim 18 \mu\text{s}$  at 408.5 nm. The mirrors were mounted on the home-made mirror mounts with purge volumes at both ends of the cell; the mirror mounts were connected to a 66 cm long glass tube (2.54 cm O.D.) through which the sample air flowed. Small purge flows (25 mL/min zero air for each mirror) were introduced directly to the purge volumes in front of the mirrors for maintaining the mirror cleanliness. Pressure and temperature were monitored independently for each cell. The light transmitted through the end mirror of each cavity was projected onto a photomultiplier tube module (Hamamatsu, H5783). Ringdown transients at a repetition rate of 2 kHz were acquired with a PCI-based transient digitizer (Adlink, PCI-9846H/512, 16 bits, 40 Mhz). 2000 ring-down traces were co-added and fit to a single exponential in every second. The data were collected and analyzed with a program written in house using the Adlink software development kit and the National Instruments Labview program.

### **8.2.2 Laboratory aerosol generation and monitoring**

The laboratory aerosols used in this work were well characterized  $(\text{NH}_4)_2\text{SO}_4$  particles, which have no absorption in the visible region. The  $(\text{NH}_4)_2\text{SO}_4$  particles

were generated by atomization of the  $(\text{NH}_4)_2\text{SO}_4$  solution in distilled water using a homemade atomizer. The aerosol size distribution was varied by changing the concentration of the  $(\text{NH}_4)_2\text{SO}_4$  solution.

Figure 1 shows the schematic diagram of the aerosol optical extinction measurements. The atomized aerosols were first dried by passing through a silicone gel dryer (10 cm dia., 75 cm long) in the atomizer. The dried particles then flowed through a commercial differential mobility analyzer (DMA) (TSI, Model 3080) for selection in a nearly mono-dispersed size distribution. The size-selected aerosols had diameters ranging from 50 to 500 nm controlled by choosing the different voltages of DMA.

The zero air sample containing the size-selected aerosols was drawn into the sample CRDS channel at a flow rate of 0.5 L/min for the aerosol optical extinction measurements, while the reference CRDS cell was under zero air gas flow (0.5 L/min) for background reference. A condensation particle counter (CPC) (TSI, Model 3772) was used to measure the particle concentration exiting the sample CRDS cell. The CPC detected particles from 10 to 1000 nm diameter. After the CPC, a pump was used to draw the sample at a flow rate of 0.5 L/min.

### **8.2.3 Ambient measurements**

Ambient measurements were carried out for proof of principle in this work. A sampling inlet was positioned outside of the laboratory window. The ambient air sample from the common inlet was divided into the two CRDS cells. The sampling flow rate was maintained at 1.0 L/min for each cell.

A 0.45  $\mu\text{m}$  Teflon particle filter was installed in front of the reference channel to remove the particles in the ambient air stream, and the background level (mainly from ambient  $\text{NO}_2$ ) [21] was obtained from the reference cell. Meanwhile, the sample channel measured the background level plus the optical extinction of the particles. The difference between these two channels was the aerosol optical extinction. The aerosol sample exiting from the sample channel was also analyzed for its size distribution using the commercial scanning mobility particle sizer (SMPS), which is a built-in application combining the DMA and CPC.

### **8.2.4 Extinction efficiency calculations**

The aerosol extinction efficiencies ( $Q_e$ ) were calculated using the program MiePlot v4.1 ([www.philiplaven.com](http://www.philiplaven.com)) in this paper. This program is based on calculations and simulations using the Mie theory and Debye series. The program

can compute the scattering intensity as a function of the scattering angle, wavelength, and radius and refractive index of the aerosols. It can produce the extinction cross sections and extinction efficiencies as functions of radius of the scattering sphere, size parameter or wavelength.

## **8.3. Results and discussion**

### **8.3.1 Comparison between the Mie theory calculations and the CRDS measurements**

The optical extinctions of the  $(\text{NH}_4)_2\text{SO}_4$  particles were measured at 408.5 nm using CRDS and are compared with the predictions by the Mie theory. Figure 2 shows sample data of experimentally measured extinction coefficients as a function of aerosol number density for the  $(\text{NH}_4)_2\text{SO}_4$  aerosols of sizes between 50 to 500 nm. The experimental data points are fitted with linear least-squares fitting. The slope represents the optical extinction cross sections (the product of  $\epsilon$  and  $Q_e$ , Eqn. 2). The Mie extinction cross sections are calculated using the refractory index of  $(\text{NH}_4)_2\text{SO}_4$ , which is  $1.53 + 0.00i$  near 400 nm at room temperature [28]. The extinction cross sections from the Mie theory and the CRDS measurements are compared for different aerosol sizes in Figure 3, and they are in good agreement within 5% for aerosols ranging from 50 to 500 nm in diameter.

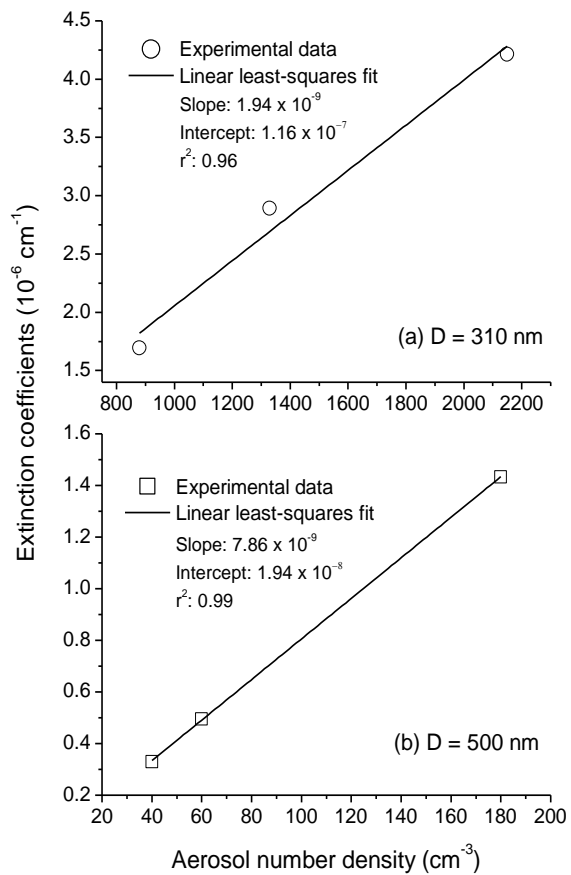


Figure 8- 2 Measurements of extinction coefficient at 408.5 nm as a function of particle number density for particles with diameter of (a) 310 nm and (b) 500 nm.

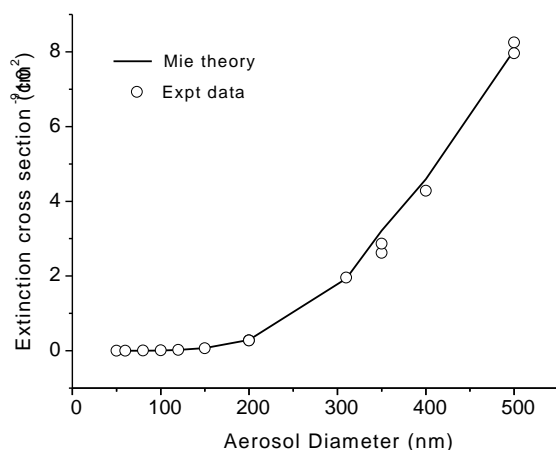


Figure 8- 3 Comparison of extinction cross sections at 408.5 nm from the Mie theory and the CRDS measurements for aerosols of sizes from 50 to 500 nm.

The  $Q_e$  value of mono-dispersed spherical aerosols can be derived from the measured extinction cross sections using the results in Figure 8-3 (Eqn 8-2). For a spherical aerosol of diameter between 50 and 500 nm, the  $Q_e$  value is calculated numerically using the Mie theory. Figure 8-4 compares the experimentally measured extinction efficiency and the calculated efficiency as a function of the aerosol size for non-absorbing spherical aerosols with  $n = 1.53$ . Figure 8-5 shows the extinction efficiency versus the size parameter  $x$  measured at 408.5 nm. The extinction efficiency initially increases with the size parameter and reaches a maximum value of  $\sim 4$  near  $x = 4$ . There is a good correlation between the calculated and measured



extinction efficiency values. The small difference between the calculations and measurements could be attributed to the actual shapes of the aerosol particles in the sample stream, which may not be completely spherical as assumed in the Mie theory calculations, or loss of the aerosols along the gas line before entering the CPC [15].

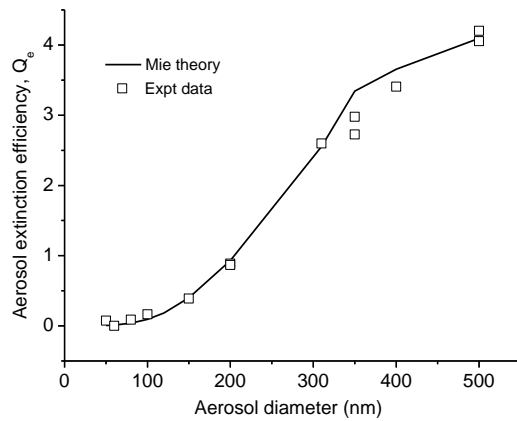


Figure 8- 4 Extinction efficiency  $Q_e$  vs. the aerosol size (diameter) at 408.5 nm.

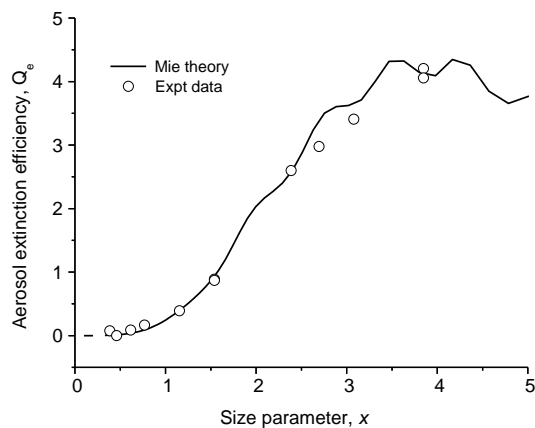


Figure 8- 5 The extinction efficiency  $Q_e$  vs. the size parameter  $x$  at 408.5 nm

### 8.3.2 Ambient measurements

As a test of the CRDS system, ambient measurements of optical extinction of aerosols were carried out in the winter of 2011. The sample point was located outside of our laboratory building at the University of California, Riverside. The ambient air samples were drawn into a copper tubing through a hole in the windowsill of the laboratory and were then introduced into the CRDS cells. The copper tubing may cause some wall loss of the aerosol particles when sampling from ambient air. The CRDS measurements were taken every 2 sec in which 4000 ring-down traces were co-added.  $\tau_0$  was obtained using zero air in both channels. In the reference channel, a 0.45  $\mu\text{m}$  Teflon particle filter was used to remove the particles. Another filter was also used in the sample channel when comparing the

response of CRDS with and without the optical extinction of aerosols. It was assumed that the filter did not affect the composition of the air. The pressure drop over the filter was negligible and no corrections were made for changes in the Rayleigh scattering. The sensitivity of the CRDS system was  $0.24 \text{ Mm}^{-1}$  ( $1\sigma$ ) based on the zero air baseline noise. The ambient measurement signals, however, were noisier due to the fluctuations from wind, pressure, temperature, etc.

The size distribution of the aerosol sample monitored in the CRDS system was obtained by SMPS after CRDS (shown in Figure 8-6). The sampled ambient air had no aerosols larger than 300 nm, either because of the clean ambient air in the winter and/or the loss of aerosols along the sampling line. Since under the current condition it is not possible to obtain all the parameters of the ambient aerosols, such as their refractive index and shapes, it is difficult to accurately calculate the aerosol optical extinction from the Mie theory. If the ambient aerosols are assumed to be spherical and are mainly composed of secondary organic aerosols (whose refractive index is in the range of 1.37-1.53 [29, 30]), the total optical extinction can be estimated from the Mie theory by integrating all the aerosol optical extinction. The optical extinction coefficient for the aerosols shown in Figure 6 is estimated to be in the range of  $1.6$  to  $2.8 \times 10^{-7} \text{ cm}^{-1}$ .

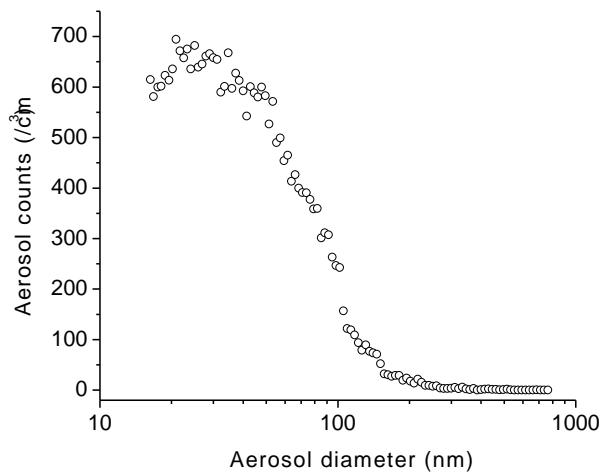


Figure 8- 6 Ambient aerosol distribution obtained by SMPS through the sample system. There might be some wall loss.

Figure 8-7 describes the CRDS measurement for ambient aerosol optical extinction coefficient from both the sample and reference channels. The reference channel sampled the ambient air with the particle filter removing all the aerosols, while the sample channel was tested with and without the particle filter. The gas phase species that absorbs significantly at 408.5 nm is NO<sub>2</sub>. The ambient NO<sub>2</sub> was partially removed by the copper tubing, which was about 3 ppb leftover when reaching the CRDS cells, and was treated as the background (shown in the reference channel). The total extinction from NO<sub>2</sub> and aerosols was measured in the sample channel, and when the particle filter was in place there was a drop of the extinction

coefficient of  $\sim 1.3 \times 10^{-7} \text{ cm}^{-1}$  from the ambient level, indicating removal of the contribution from the aerosol optical extinction. Furthermore, when the filter was in place in the sample channel, the signals from the sample channel and the reference channel were in agreement, indicating proper background measurements in the reference channel. The dual-channel approach allows for continuous monitoring of the background and background plus aerosol extinction and thus real time removal of the background interference. Although the CRDS measurement and the calculated optical extinction coefficient differ by a factor of up to 2, this discrepancy could be due to the unknown properties of the ambient aerosols discussed before.

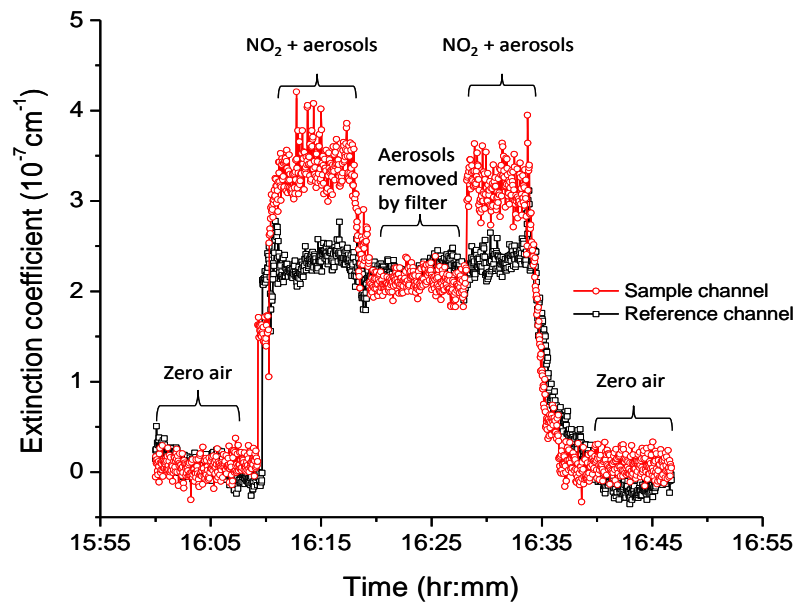


Figure 8- 7 CRDS measurement for ambient aerosol optical extinction coefficient in both the sample and reference channels. The system started with zero air for the baseline. At 16:10, the system

drew in the ambient air; the sum of NO<sub>2</sub> signal and aerosol optical extinction was obtained in the sample channel, while the reference channel monitored the NO<sub>2</sub> background. At 16:17, a particle filter was installed in the sample channel to remove the aerosols, and the background NO<sub>2</sub> level was measured in both channels. At 16:29, the total signal was recovered by removing the filter in the sample channel. At 16:35, the sampling was stopped and the zero air baseline level was obtained again.

## 8.4. Conclusion

In this study, a broadband blue diode laser is used as the light source for direct coupling into the CRDS cells. The instrument is simple, inexpensive, and portable. The well-characterized laboratory generated (NH<sub>4</sub>)<sub>2</sub>SO<sub>4</sub> aerosols with different sizes in 50-500 nm are tested using the CRDS system, and the results are compared with the Mie theory calculations. Good agreement in  $Q_e$  within 5% is found. A dual-channel approach is applied for continuous monitoring of the background and background plus aerosol extinction signals, which allows for real time removal of background interferences. The sensitivity of the instrument can reach as low as 0.24 Mm<sup>-1</sup>(1 $\sigma$ ), which is suitable for the field study and ambient measurement.

Although only one diode laser wavelength is demonstrated in this proof-of-principle work, multiple wavelengths can be readily incorporated by simply replacing or adding other diode light sources. With the development of different types of diode lasers, using multiple wavelength light sources for aerosol optical extinction is possible. Measurements at multiple wavelengths can further provide information of the refractive index using the fitting of the extinction data. It can also provide an estimation of the single scattering albedo, which provides information on the extinction of light, including both scattering and absorption [31].

## References

1. J. H. Seinfeld and S. N. Pandis, *Atmospheric Chemistry and Physics: from Air Pollution to Climate Change* (John Wiley, New York, 1998).
2. W. C. Hinds, *Aerosol Technology: Properties, Behavior, and Measurement of Airborne Particles*, 2nd ed. (John Wiley, New York, 1999).
3. A. D. Sappey, E. S. Hill, T. Settersten, and M. A. Linne, "Fixed-frequency cavity ringdown diagnostic for atmospheric particulate matter," *Opt. Lett.* **23**, 954-956 (1998).

4. J. D. Smith and D. B. Atkinson, "A portable pulsed cavity ring-down transmissometer for measurement of the optical extinction of the atmospheric aerosol," *Analyst* **126**, 1216-1220 (2001).
5. V. Bulatov, M. Fisher, and I. Schechter, "Aerosol analysis by cavity-ring-down laser spectroscopy," *Anal. Chim. Acta* **466**, 1-9 (2002).
6. V. Bulatov, A. Khalmanov, and I. Schechter, "Study of the morphology of a laser-produced aerosol plume by cavity ringdown laser absorption spectroscopy," *Anal. Bioanal. Chem.* **375**, 1282-1286 (2003).
7. A. Pettersson, E. R. Lovejoy, C. A. Brock, S. S. Brown, and A. R. Ravishankara, "Measurement of aerosol optical extinction at 532 nm with pulsed cavity ring down spectroscopy," *J. Aerosol Sci.* **35**, 995-1011 (2004).
8. C. Spindler, A. A. Riziq, and Y. Rudich, "Retrieval of Aerosol Complex Refractive Index by Combining Cavity Ring Down Aerosol Spectrometer Measurements with Full Size Distribution Information," *Aerosol Sci. Technol.* **41**, 1011-1017 (2007).
9. T. Baynard, E. R. Lovejoy, A. Pettersson, S. S. Brown, D. Lack, H. Osthoff, P. Massoli, S. Ciciora, W. P. Dube, and A. R. Ravishankara, "Design and application of a pulsed cavity ring-down aerosol extinction spectrometer for field measurements," *Aerosol Sci. Technol.* **41**, 447-462 (2007).



10. E. Dinar, A. A. Riziq, C. Spindler, C. Erlick, G. Kiss, and Y. Rudich, "The complex refractive index of atmospheric and model humic-like substances (HULIS) retrieved by a cavity ring down aerosol spectrometer (CRD-AS)," *Faraday Discuss.* **137**, 279-295 (2008).
11. K. D. Dial, S. Hiemstra, and J. E. Thompson, "Simultaneous measurement of optical scattering and extinction on dispersed aerosol samples," *Anal. Chem.* **82**, 7885-7896 (2010).
12. N. Lang-Yona, Y. Rudich, E. Segre, E. Dinar, and A. Abo-Riziq, "Complex Refractive Indices of Aerosols Retrieved by Continuous Wave-Cavity Ring Down Aerosol Spectrometer," *Anal. Chem.* **81**, 1762-1769 (2009).
13. M. A. Freedman, C. A. Hasenkopf, M. R. Beaver, and M. A. Tolbert, "Optical Properties of Internally Mixed Aerosol Particles Composed of Dicarboxylic Acids and Ammonium Sulfate," *J. Phys. Chem. A* **113**, 13584-13592 (2009).
14. N. Lang-Yona, A. Abo-Riziq, C. Erlick, E. Segre, M. Trainic, and Y. Rudich, "Interaction of internally mixed aerosols with light," *Phys. Chem. Chem. Phys.* **12**, 21-31 (2010).
15. R. E. H. Miles, S. Rudic, A. J. Orr-Ewing, and J. P. Reid, "Measurements of the wavelength dependent extinction of aerosols by cavity ring down spectroscopy," *Phys. Chem. Chem. Phys.* **12**, 3914-3920 (2010).

16. A. W. Strawa, R. Castaneda, T. Owano, D. S. Baer, and B. A. Paldus, "The measurement of aerosol optical properties using continuous wave cavity ring-down techniques," *Anglais* **20**, 454 (2003).
17. T. J. A. Butler, J. L. Miller, and A. J. Orr-Ewing, "Cavity ring-down spectroscopy measurements of single aerosol particle extinction. I. The effect of position of a particle within the laser beam on extinction," *The Journal of Chemical Physics* **126**, 174302-174307 (2007).
18. A. O'keefe and D. A. G. Deacon, "Cavity ring-down optical spectrometer for absorption measurements using pulsed laser sources," *Review of Scientific Instruments* **59**, 2544-2551 (1988).
19. J. J. Scherer, J. B. Paul, A. Okeefe, and R. J. Saykally, "Cavity ringdown laser absorption spectroscopy: History, development, and application to pulsed molecular beams," *Chem. Rev.* **97**, 25-51 (1997).
20. M. D. Wheeler, S. M. Newman, A. J. OrrEwing, and M. N. R. Ashfold, "Cavity ring-down spectroscopy," *J Chem Soc Faraday Trans* **94**, 337-351 (1998).
21. J. Hargrove, L. Wang, K. Muyskens, M. Muyskens, D. Medina, S. Zaide, and J. Zhang, "Cavity Ring-Down Spectroscopy of Ambient NO<sub>2</sub> with Quantification and Elimination of Interferences," *Environ. Sci. Technol.* **40**, 7868-7873 (2006).

22. H. D. Osthoff, S. S. Brown, T. B. Ryerson, T. J. Fortin, B. M. Lerner, E. J. Williams, A. Pettersson, T. Baynard, W. P. Dubé, S. J. Ciciora, and A. R. Ravishankara, "Measurement of atmospheric NO<sub>2</sub> by pulsed cavity ring-down spectroscopy," *J. Geophys. Res.* **111**, D12305 (2006).
23. H. Fuchs, W. P. Dubé, B. M. Lerner, N. L. Wagner, E. J. Williams, and S. S. Brown, "A Sensitive and Versatile Detector for Atmospheric NO<sub>2</sub> and NO<sub>x</sub> Based on Blue Diode Laser Cavity Ring-Down Spectroscopy," *Environ. Sci. Technol.* **43**, 7831-7836 (2009).
24. S. S. Brown, H. Stark, S. J. Ciciora, R. J. McLaughlin, and A. R. Ravishankara, "Simultaneous in situ detection of atmospheric NO<sub>3</sub> and N<sub>2</sub>O<sub>5</sub> via cavity ring-down spectroscopy," *Review of Scientific Instruments* **73**, 3291-3301 (2002).
25. J. D. Ayers, R. L. Apodaca, W. R. Simpson, and D. S. Baer, "Off-axis cavity ringdown spectroscopy: application to atmospheric nitrate radical detection," *Appl. Opt.* **44**, 7239-7242 (2005).
26. D. S. Medina, Y. Liu, L. Wang, and J. Zhang, "Detection of sulfur dioxide by cavity ring-down spectroscopy," *Environ. Sci. Technol.*, null-null (2011).

27. Y. Liu, R. Morales-Cueto, J. Hargrove, D. Medina, and J. Zhang, "Measurements of Peroxy Radicals Using Chemical Amplification-Cavity Ringdown Spectroscopy," *Environ. Sci. Technol* **43** 7791–7796 (2009).
28. O. B. Toon, J. B. Pollack, and B. N. Khare, "The Optical Constants of Several Atmospheric Aerosol Species: Ammonium Sulfate, Aluminum Oxide, and Sodium Chloride," *J. Geophys. Res.* **81**, 5733-5748 (1976).
29. T. Nakayama, Y. Matsumi, K. Sato, T. Imamura, A. Yamazaki, and A. Uchiyama, "Laboratory studies on optical properties of secondary organic aerosols generated during the photooxidation of toluene and the ozonolysis of alpha-pinene," *Journal of Geophysical Research-Atmospheres* **115**(2010).
30. H. Redmond and J. E. Thompson, "Evaluation of a quantitative structure-property relationship (QSPR) for predicting mid-visible refractive index of secondary organic aerosol (SOA)," *Physical Chemistry Chemical Physics* **13**, 6872-6882 (2011).
31. R. E. H. Miles, S. Rudic, A. J. Orr-Ewing, and J. P. Reid, "Influence of Uncertainties in the Diameter and Refractive Index of Calibration Polystyrene Beads on the Retrieval of Aerosol Optical Properties Using Cavity Ring Down Spectroscopy," *J. Phys. Chem. A* **114**, 7077-7084 (2010).

# **Chapter 9 A new method of measuring the index of refraction and thickness of transparent thin-films using cavity – ring down spectroscopy.**

## **Abstract**

In this paper, we present a novel method for determining the thickness of a non absorbing thin film on a transparent substrate through the analysis of the transmittance signal measured at various incident angles using CRDS. A model is developed and demonstrated for a polymer thin film. Thicknesses of a few tens of nanometers can be measured. This method is simple and capable of in situ studies of nanoscale thin films.

## **9.1 Introduction**

In recent years there has been a growing interest in techniques for depositing of various thin films for applications in many fields of microelectronics, such as optoelectronic devices, surface acoustic wave electroacoustic and acousto-optic

devices, integrated optics, etc. As a result, a large number of techniques have been developed for characterizing the properties of these films. Therefore, the information on thickness and optical constants of thin films is essential. Among the various techniques for thin film measurement, optical methods can provide important information on the structure of the films, as well as useful insights into the optimization of the deposition procedures. These technologies are widely used in the semiconductor or flat panel display industry as they are capable of fast and non-destructive measurements. Specifically, the optical refractive indices of thin films can be measured [1] using techniques such as photometry [2, 3], ellipsometry[4-6], and polarimetry [5, 6]. Ellipsometry [7, 8] or reflectometry [9] have been the standard procedure in the measurement of thin film thickness. Phase-shifting interferometry has emerged in the last few decades as a tool for optical testing. It offers high accuracy but it is inconvenient in everyday operation.

In addition, the measurement of thickness of transparent plates and films made of various materials is important for quality control in industry. In particular, the need for a long data acquisition time becomes a critical problem for distribution measurements. However, making simultaneous measurements is not a trivial undertaking[10, 11]. For the thickness and optical constants measurements, the prism coupling method, ellipsometry, and photometry have been widely used. The

first method permits the simultaneous determination of refractive index and thickness by measuring only the angle of incidence, but it can not measure the extinction coefficient [12] and the films should be thick enough to allow more than two modes to be guided for accurate measurement [13]. Fukano and Yamaguchi [14] decided the optical path difference directly by measuring the resultant interferometric phase shift, but the measurement can be carried out instantaneously only with a micrometer-order resolution. With respect to ellipsometry, although an accurate refractive index can be extracted for a single atomic or molecular layer such as a Langmuir–Blodgett film [10] a special substrate that is especially thick or strongly absorbing is required [15]. thus in situ measurement of optical constants of a thin film deposited upon a glass substrate of a plane-parallel plate is not possible. Photometry requires relatively lengthy analysis and complex experimental apparatus including a monochromator because white light is used to avoid a possible interference effect in the substrate [15-18]. Real-time profilometry based on heterodyne interferometry or the Moire ´ method has been reported. However, this profilometry cannot measure a discontinuous height step caused by the phase ambiguity. Kuwamura and Yamaguchi used a wavelength scanning profilometry for real-time surface shape measurement but their accuracy was only as high as 1  $\mu\text{m}$ .

Moreover, during the past two decades much attention has been paid to surface-mapping by use of white-light scanning interferometry; as a result, quite a few techniques for such mapping are now available. Although the former surface-mapping techniques differ from one another in the way in which they accomplish fringe data processing, most of them are well capable of providing nanometer resolutions in precision profile measurement of opaque surfaces. Nevertheless, this becomes challenging for transparent materials. Jung and Bum Ku Rhee presented a method for determining both the thickness and the optical constants of a weakly absorbing thin film on a nearly transparent substrate through analysis of transmittance measured at various incident angles with coherent light [4]. It was found that a thickness of a few hundred nanometers can be measured, which does not have very high sensitivity. Maruyama used low-coherence interferometer system for the simultaneous measurement of refractive index and thickness, but their best accuracy can be achieved only when the sample is as thick as 20  $\mu\text{m}$  [7].

Recently, higher spatial resolution is expected as the feature size under inspection decreases [13]. A smaller feature size also demands higher sensitivity. The available and common instruments used for such measurements, such as AFM, scanning electron microscopes (SEMs) and mechanical stylus profilometers, have



been destructive to thin films. Although such destructive approaches can produce accurate measurements, they are undesirable because they destroy samples. A

So a high sensitivity, cheap, easy to use, in situ measurement method for measuring the thickness of thin transparent film is highly needed in nowadays. In this paper, we present a new promising method of thin film measurement with the application of cavity ring-down spectroscopy. With this method, we have demonstrated that a few tens of nanometer thickness could be measured and the method is simple and it is potential to be used in in situ measurement of the growth of nanoparticle film.

In addition to the use of this technique in industrial applications, the potential for this novel technique extends over to biological systems. Currently surface Plasmon resonance (SPR) is able to provide information on the surface of biological systems such as DNA and RNA hybridization studies, antibody-antigen binding, and protein interactions without the need for labels such as detection schemes based on fluorescence. These interactions on the surface are quantified by measuring the changes in the index of refraction as molecules are adsorbed onto the surface, allowing for the potential of routine kinetic studies on binding. However, there is a need for the sample to be modified on a gold or noble metal thin film, which when irradiated with plane polarized light will generate an exponentially decaying

evanescent wave penetrating through the sample up to thicknesses of around 200 nm. In addition, having to functionalize the gold surface with alkanethiol self adsorbed monolayer (SAMs) limits the studies that can be done with SPR compared to a glass surface without having to further modify the gold surface with calcinated silicate films. The CRDS approach presented here allows for the potential of surface studies without the need to modify the surface with noble metal substrates, and not being limited by the depth an evanescent wave can penetrate through the sample, while still having the sensitivity and a fast enough response time for kinetic studies.

## **9.2 Experimental**

### **9.2.1. CRDS instrument setup**

Normally, CRDS is used as an absorption technique based on measurement of light decay rate rather than light attenuation. CRDS has a very long effective length (>km) that leads to high sensitivity [19-23]. In a typical CRDS setup, laser pulses are trapped in an optical cavity that is composed of two high-quality mirrors (with typical reflectivity  $R > 99.9\%$ ). The intensity of the trapped laser pulses decreases by a very small percentage in each round trip within an empty cavity due to mirror loss and light scattering; the intensity of the light decays as an exponential

function of time (with a decay constant, ring-down time  $\tau_0$ ). When there is some absorbing sample inside the cavity, its absorbance will increase the loss, which can be determined from comparing the empty cavity ring-down time ( $\tau_0$ ) and the one with the analyte ( $\tau$ ) [19-23]:

$$\alpha = \frac{L}{c l_s} \left( \frac{1}{\tau} - \frac{1}{\tau_0} \right) = \sigma N$$

where  $\alpha$  is the absorption coefficient,  $c$  is the speed of light,  $L$  is the cavity length, and  $l_s$  is the sample path length;  $\sigma$  and  $N$  are the absorption cross sections and number density of the analyte, respectively. CRDS has the advantage of being insensitive to variations in laser intensity due to the measurement of a rate constant. It is a rapid, real time technique, with individual ring-down events on the millisecond time scale. The detail description of CRDS can be found in Chapter 1 of this thesis.

CRDS is a technique typically used for gas phase samples. However, in this work, we used non- absorbance materials and instead of gas samples. We used standard glass pieces with PMMA (polymethyl methacrylate) films, which will cause light loss because of scattering and interferences. Under these conditions, we have developed a new technique to measure the thickness of the thin films. The detailed principle and calculation of the modeling related to this CRDS work are discussed later in this paper.

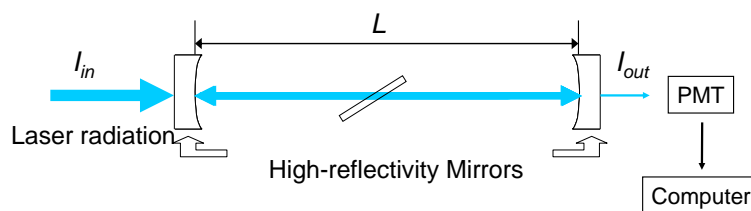


Figure 9- 1 CRDS experimental setup for measurement of transparent thin film thickness

The setup of our CRDS is shown in Figure 9-1. A 532-nm output laser from a Nd:YAG laser pumps a tunable dye laser to produce radiation. In this work, we used the dye laser output in two different wavelength ranges to demonstrate the technique and our optical model. One region is ranging from 650 to 670 nm wavelength, the other one is from 350 to 355 nm.. The laser radiation enters the CRDS cell (0.9 m in length) and passes through the glass slide with many round trips..The output light is detected by a photomultiplier (PMT). The ring-down signal is collected on a 14-bit 200 MS/s oscilloscope card (Gage); each ring-down curve is fitted using a fast algorithm developed by Halmer et al [24]. and used in combination with the data collection software on National Instruments Labview.

### 9.2.2 Experimental procedures

In this work, we used two steps to demonstrate our model and method. First, we used plain standard microscope cover slides with different materials, thickness,

incident angles and number of slides to test our model. In the second step, we made 6 different thickness of PMMA film on 0.0075 inch thick BK7 cover glasses and carried out experiments using the same incident angles (59 degree). To demonstrate our model of measuring the thickness of the film we used surface profilometer (Dektek 8) to get a reference thickness of the films and compared with the thickness we measured using CRDS.

Table 9- 1 Different conditions of the experiments in the first step.

Materials	Thickness (mm)	Incident angles (degree)	Numbers of slides	Wavelength range of laser irradiation
BK7 cover glass	0.150	53 54 55 56  57  58 59 60 62	1, 2 and 3	350nm -  355nm  650nm -  670nm
	0.190	57 58 59  60	1	650nm -  670nm
Quartz cover slides	0.150	57 58 59  60	1	650nm -  670nm

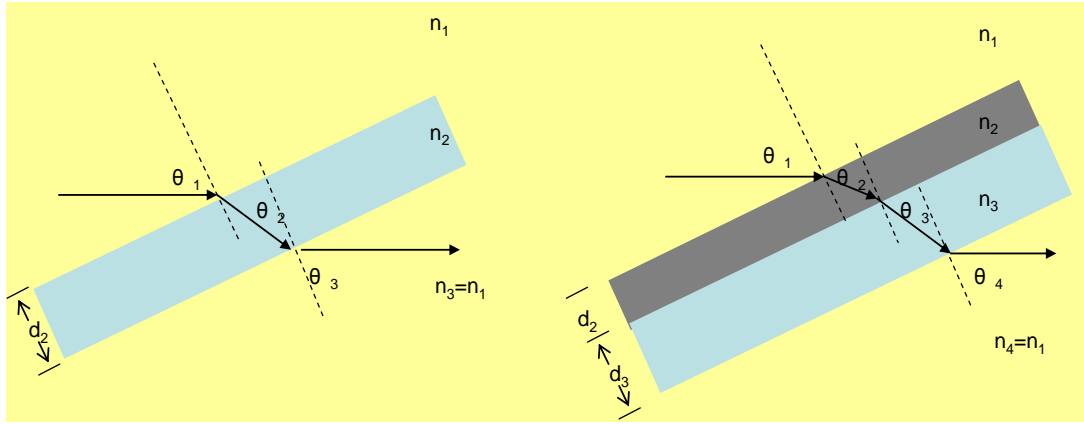
Table 9-1 shows all the conditions we used in the experiments of step 1. The cover slides are standard No. 1 and No. 1.5 thickness cover slides from Fisher scientific. The PMMA films made in step 2 is produced by spinning coating with standard PMMA solution (MicroChem 495 A2, 495 C2, 950 C4). Different thickness of films is obtained by controlling the spin speed. Figure 9-2 shows a particular experiment data we got from one 0.150mm BK7 cover glass with 650nm-670nm wavelength laser radiation. The solid line on the bottom is the open path data without any cover slides inside the CRDS cell, which is the background data for this system. Other lines in this figure stand for different incident angles on the glass slide. The flat line among those has 57 degree incident angle, which shows the data from the irradiation incident angle at Brewster angle. The further the incident angles away from Brewster angle, the bigger amplitude of the oscillations, which is shown in this figure. The oscillation period is coming from the interference of the laser radiation and it depends on the cover slide thickness and the index of refraction of the materials of the slides. As we used the same glass slide for all of these experiment, all the oscillations have the same length of periods. All the data under different conditions are recorded similarly and they will be analyzed and compared with model in discussion section in this paper.



Figure 9- 2 A 0.0150mm BK7 cover glass with 650nm-670nm wavelength laser irradiation at different incident angles. (BA = Brewster Angle)

### 9.3 Theory and Modeling

The modeling is presented here using a non-absorbing thin film of index of refraction  $n_2$  and thickness  $d_2$  coated on a non- absorbing substrate (assumed semi-infinite) and the reflection of a beam at the interfaces between semi-infinite media labeled 1, 2, 3 and 4 (or 1, when media 4 and media are the same) (Figure 9-3, b). All media are assumed to be isotropic, so the dielectric functions are scalars. The radiation is from coherent light source and it has a p-polarizaion (in plane).



(a).

(b).

Figure 9- 3 Illustration of (a) three- and (b) four- media systems encountered in reflection experiments.  $d$  is thickness,  $\theta$  is incident angle,  $n$  is index of refraction and the footnotes 1,2,3,4 are represented for semi-infinite media.

The angles of incident between different media can be calculated by Snell's law and the index of refraction ( $n$ ) is complex number. As shown in Figure 9-3, by using the Fresnel relation equations, for p-polarization radiation incident on the interface of 1 and 2, the reflection and transmission coefficients are

$$r = \tan(\theta_1 - \theta_2) / \tan(\theta_1 + \theta_2) \tag{9-1}$$

$$t = 2 \sin \theta_2 \cos \theta_1 / \sin(\theta_1 + \theta_2) \cos(\theta_1 - \theta_2) \tag{9-2}$$

When applied to an arbitrary interface, say between media  $j$  and  $k$ , the reflection coefficient will be expressed as  $r_{jk}$  and the reflectance  $R = |r|^2$  will be expressed as  $R_{jk}$ . Consequently, equation 1 is  $r_{12}$  for the respective polarizations.



In the 3-layer model, let a quasi-monochromatic plane wave of amplitude  $E_0$  and wavelength  $\lambda$  be incident on the medium from a semi-infinite medium of index of refraction  $n_1$ . The wave undergoes multiple reflections in the slide, shown as 2 in the figure. The reflection and transmission coefficients are real. The resultant amplitude of the reflected wave is given by the geometric series:

$$E_r = E_0 [r_{12} + t t' r_{23} e^{i\beta} + t t' r'_{12} r_{23}^2 e^{i2\beta} + \dots] = E_0 [r_{12} + r_{23} (1 - r_{12}^2) e^{i\beta} / (1 - r_{12}' r_{23} e^{i\beta})] \quad (9-3)$$

Where  $t$  is transition and “ ’ ” is the reflection of its contra one without “ ’ ”. In this equation, the phase shift:

$$\beta = 4\pi(n_2 d_2 \cos\theta_2) / \lambda \quad (9-4)$$

In addition, we have

$$r_{12}' = -r_{12} \quad (9-5)$$

$$t t' = 1 - r_{12}^2 \quad (9-6)$$

$$\text{So, } E_r / E_0 = (r_{12} + r_{23} e^{i\beta}) / (1 - r_{12}' r_{23} e^{i\beta}) = r_{123} \quad (9-7)$$

Consider a given multilayer system, called the “old” system and a “new” system, consisting of an overlayer of thickness  $d$  and refractive index  $n$  grown on top of old system. A probe beam propagates at an angle  $\theta'$  is in this new layer. The reflection coefficient for a two medium system consisting of ambient and overlayer material media is  $r_{ao}$ . The old system’s reflection coefficient for a beam beginning in the overlayer is called  $r_{old}$ , then the reflection coefficient of the new system is  $r_{new}$

$$r_{\text{new}} = (r_{\text{ao}} + r_{\text{old}} Z) / (1 + r_{\text{ao}} r_{\text{old}} Z) \quad (9-8)$$

$$Z = e^{i\beta}, \text{ where } \beta = 4\pi(nd \cos\theta')/\lambda$$

The recursion expression is equivalent to eqn 9-7 with  $r_{123} \rightarrow r_{\text{new}}$ ,  $r_{12} \rightarrow r_{\text{ao}}$ ,  $r_{23} \rightarrow r_{\text{old}}$

Using this recursion equation 8, along with eqn 9-7, for the 4- layer model (Figure 9-3 (b)), the reflection coefficient is

$$r_{1234} = \frac{r_{12} + r_{23} e^{i\beta_2} + r_{34} e^{i(\beta_2 + \beta_3)} + r_{12} r_{23} r_{34} e^{i\beta_3}}{1 + r_{12} r_{23} e^{i\beta_2} + r_{12} r_{34} e^{i(\beta_2 + \beta_3)} + r_{23} r_{34} e^{i\beta_3}} \quad (9-9)$$

For the 4 - layer model, consider the film (medium 2) with the substrate (medium 3) are placed in air (medium 1), so medium 1 and medium 4 are the same material (air), which showed as Figure 9-3, (b). In this situation,  $n_1 = n_4$ , and based on Snell's law,  $\theta_1 = \theta_4$ . So we can replace 4 with 1 in equation 9 and get the reflection coefficient for this 4 - layer model. Here, the reflectance  $R = |r_{1231}|^2$ .

For non- absorbing materials,  $T + R = 1$ , where T is the transmission, so

$$R = |r_{1231}|^2 \text{ and } T = 1 - R = 1 - |r_{1231}|^2 \quad (9-10)$$

In CRDS, as we mentioned before, a laser pulse is trapped in a highly reflective (typically  $R > 99.9\%$ ) detection cavity. The intensity of the trapped pulse will decrease by a fixed percentage during each round trip within the cell due to both absorption and scattering by the medium within the cell and reflectivity losses. The

intensity of light within the cavity is then determined as an exponential function of time.

$$I = I_0 \exp(-t/\tau) \quad (9-11)$$

The principle of operation is based on the measurement of a decay rate rather than an absolute absorbance. This is one reason for the increased sensitivity over traditional absorption spectroscopy. The decay constant,  $\tau$ , is called the ring-down time and is dependent on the loss mechanism(s) within the cavity. For a slide in the cavity, the decay constant is dependent on mirror and slide loss and various optical phenomena like scattering and refraction:

$$\tau = \frac{n}{c} \cdot \frac{l}{1 - R_m + R + X} \quad (9-12)$$

$$1/\tau = (c/l)(1 - R_m + R + X) \quad (9-13)$$

where  $n$  is the index of refraction within the cavity, which is 1.0008 for air;  $c$  is the speed of light in vacuum,  $l$  is the cavity length,  $R_m$  is the mirror reflectivity,  $R$  is reflectance of the slides and thin films placed inside the cavity and  $X$  takes into account other miscellaneous optical losses. This equation uses the approximation  $\ln(1+x) \approx x$  for  $x$  close to zero, which is the case under cavity ring-down conditions. Under a particular condition, we assume  $X$  is a constant, which can be measured in experiment.

From the combination of equation 9-9, 10, 13, we can get a relationship of thickness (d) and index of refraction (n ) of the media and the cavity – ring down decay rate ( $\tau$ ).

$$1/\tau = (c/l)(1 - R_m + |r_{1231}|^2 + X) \quad (9-14)$$

By using this equation,  $|r_{1231}|^2$  can be obtained, which related to the thickness (d) and index of refraction (n ) of each media, which can be calculated by using the equation through (1) to (9). An example of simulation a water film growing on a BK7 cover glass is carried out and by analyzing the period of the oscillation, less than 10nm thickness difference can be distinguished with the known index of refraction.

To use this method in potential areas, we also involved more variables in this 4- layer modeling.

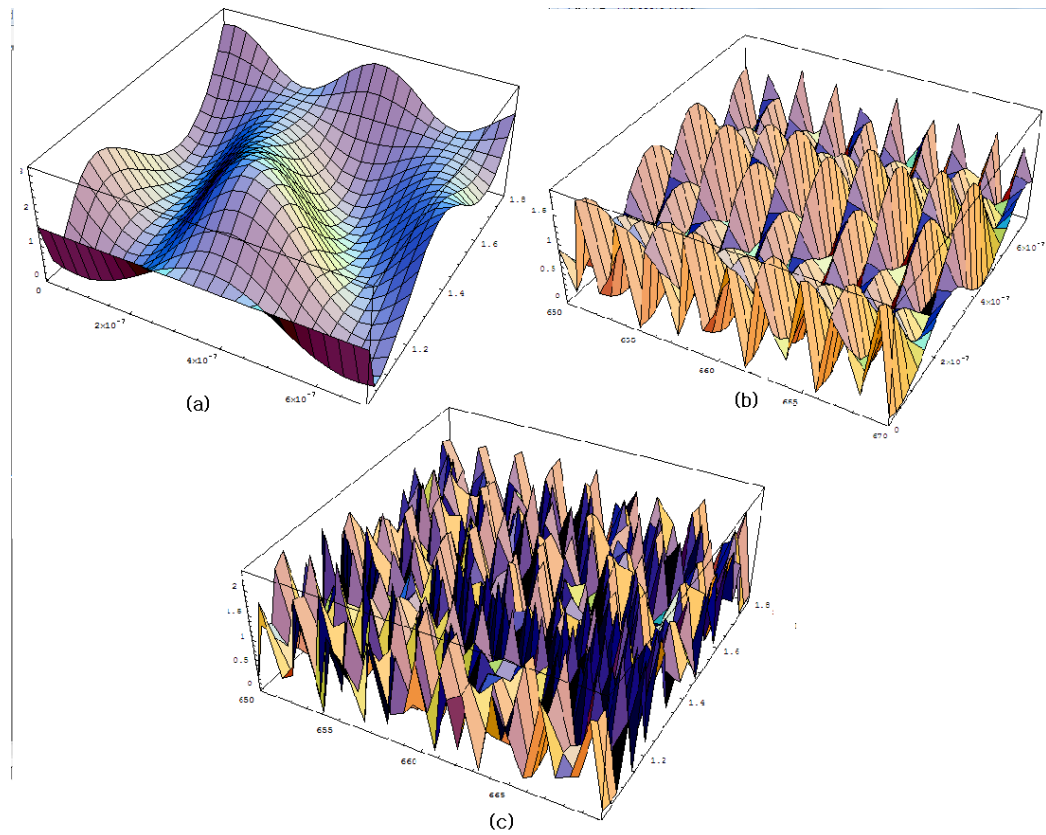


Figure 9- 4 3D surface modeling for decay rate with changing wavelength, index of refraction and film thickness. In all figures, Z axis is ring-down decay rate. (a) is the surface curve for 650nm laser wavelength with film thickness ranging from 0-700nm, index of refraction ranging from 1 to 1.8; (b) is the surface curve for index of refraction equal to 1.6, with film thickness ranging from 0-700nm, and laser wavelength from 650nm to 670nm; and (C) is the surface curve for film thickness equal to 200 nm, with laser wavelength from 650nm to 670nm, index of refraction ranging from 1 to 1.8.

Figure 9-4 shows the 3D curves of modeling for decay rate with changing wavelength, index of refraction and film thickness. In all the three figures in Figure 9-4, Z axis is ring-down decay rate. Therefore those figures tell us the relationship between those variables. From Figure 9-4 (a) (b) (c), the phase shift plus the period of the oscillatory changes dramatically in the variables ranges, which indicates that high sensitivity of measuring film thickness by this technique could be approachable.

On the other hand, by getting the accurate thickness of layers with other method, profilometer or AFM for instance, we could get the index of refraction by using this CRDS method.

## **9.4 Discussion**

### **9.4.1 Discussion of 3-layer model experiment**

As shown in Figure 9-3, (b), the 3- layer model is simply considering one medium. Here, in our experiment to simulate this 3-layer model, we put one piece of cover slide in the middle of the ring-down cavity. In this case,  $d_2=0$  in equation 9-4. And Figure 9- 5 shows the comparison of 0.150mm BK 7 cover glass and its model under different incident angles with 650nm-670nm laser radiation.

Normally, they are 4 parameters to define one oscillatory wave: period, amplitude, phase and intercept. The period is very sensitive to thickness. And it is also responses to light source wavelength. Larger thickness and shorter wavelength will reduce the period. In addition, the difference of thickness also shifts its phase and it makes it more sensitive to the thickness of the slide.

When the incidence angle is Brewster angle, the oscillatory wave amplitude is 0. Because at Brewster's angle, no light loss comes from reflection and the difference between Brewster angle data and empty cell data comes from X in equation 14, where X is assumed to be constant. Due to reflection loss, the amplitude is bigger when the incident angle is further away from Brewster angle. For BK 7, the Brewster angle is 57 degree and both model and experiment data demonstrate this conclusion. However, the model and experimental data matches less when the incident angle is further away from Brewster angle, which is shown in Figure 9-5, the amplitude in the model is much bigger than its corresponding data in experiment. This error is basically because once the CRDS window is settled, it only be counted a particular number of points to analyze the decay rate. When there is a big amount of light loss in the system, the fit will count more flat tail in the window, which will cause artificial error in the experiment data. As the result, further away from Brewster angle would cause more light loss and it would not be good for

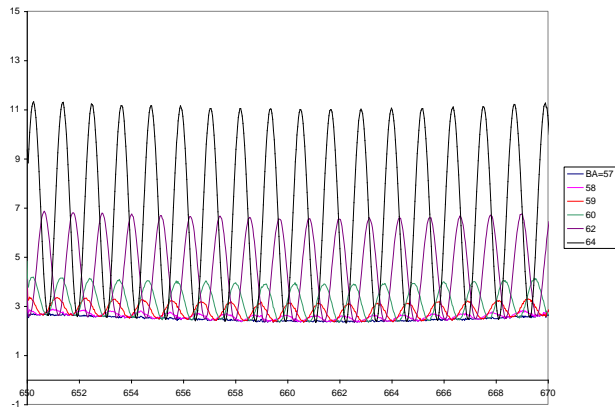
CRDS measurement to fit the modeling. Therefore, when the incident angle is close to Brewster angle (within 3 degree difference), the experiment data matches the amplitude of the model.

For the y-axis intercept of the oscillatory waves in Figure 9-5, bigger intercept mostly because of more other miscellaneous optical losses, including absorbance and scattering ( $X$  in the equation 14). Although we assume the media are no-absorbance (semi-infinite), it is not that ideal in reality. As we mentioned above,  $\ln(1+x) \approx x$  for  $x$  close to zero, but if more light are lost,  $X$  is not close to zero, which will cause error when we use the model for the incident angle is further from Brewster's angle (more than 4 degree). So in these situations,  $X$  is no longer constant and it will cause intercept difference between model and experimental data. However, since we only concern the index of refractory and thickness, we can accurate get the period and the phase shift of the oscillation spectrum and get the information from that.

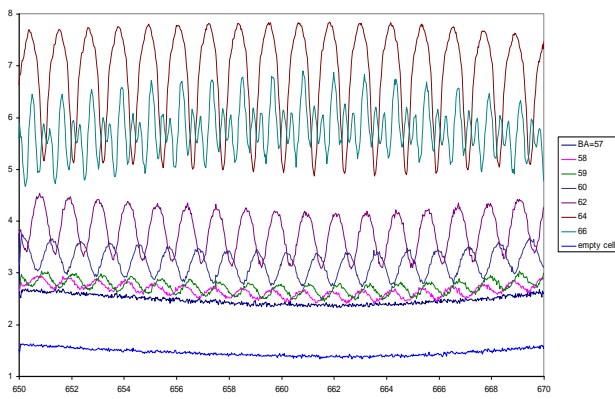
Figure 9-6 shows experimental data under different conditions. Figure 6 (a) shows using the laser wavelength range into 350 nm - 355nm. The bottom curve is the data from empty cell and the curve without oscillation is the data from the incidence angle at Brewster angle while the curve with oscillation is the data from the incidence angle at 58 degree, which is about 1 degree away from Brewster angle.



And Figure 9-6 (b) is a similar experiment with using 0.190 mm glass slide which is about 0.040mm thicker than other experiments. We also did the experiments using 0.150mm quartz cover and multiple pieces of BK7 cover glasses. All of the different conditions of experiments are described and listed in experimental part of this paper and from carrying out experiments under different conditions, it proved that the parameters of oscillatory waves including periods and phase shift are related to thickness, materials (index of refractory) and laser wavelength and demonstrated the model we deduced above.

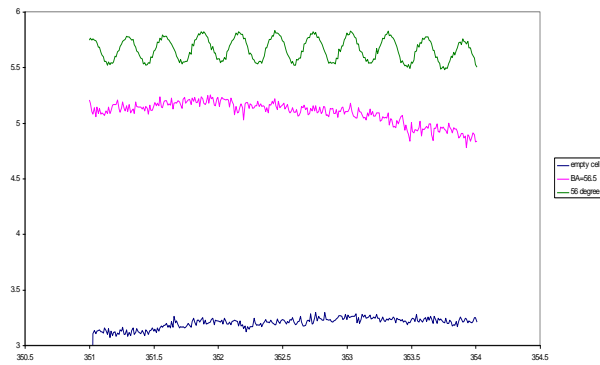


(a). Model

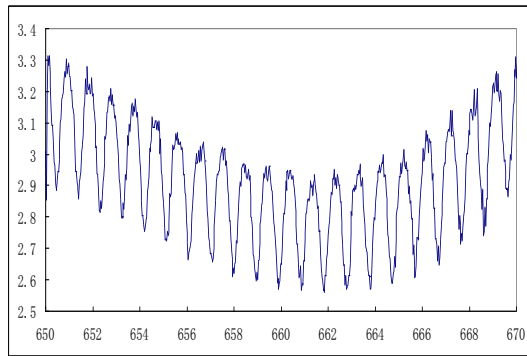


(b). Data

Figure 9- 5 Comparison of (a) model and (b) data for one 0.150mm BK7 cover glass irradiated with 650nm-670nm wavelength laser under different incident angles.



(a). 350-355nm experimental data



(b). 0.0075inch thickness cover glass

Figure 9- 6 Experimental data under different conditions. (a) used the laser wavelength range into 350 nm-355nm. The bottom curve is the data from empty cell and the curve without oscillation is the data from the incidence angle at Brewster angle while the curve with oscillation is the data from the incidence angle at 58 degree. (b) is a similar experiment using 0.190 mm glass slide

#### **9.4.2 Discussion of 4-layer model experiment**

The 3-layer experiments apply only to the glass slide. To get the information of thin film, the 4-layer modeling and experiments are necessary although it is more complicated. Not only the proprieties of the substrate we need to consider, but also the propriety of film is important. It includes its thickness, index of refractory and its surface profile. In this work, by using a proficient spin coating method, a relative flat surface of thin film can be obtained and the surface profile of it can be neglected. Moreover, it is unrealistic to detect the film surface profile under this current setup because when the CRDS is aligned, it is impossible to move the laser detection probe, which will cause the misalignment of the system. Also, it is hard to move the slide without impact its incident angle under the present experimental setup. Secondly, a method to orientate the coordinate of each point on the film and record its thickness for a 3-D profile measurement is not available. But theoretically it could be done by this method which needs future work. Meanwhile, for a very thin film, the property of thickness is much more important than the surface profile while the its thickness is relatively constant. Therefore, in this work, a particular condition for the substrate is chosen to simplify the experiment and only it only fous on the thickness and index of refractory of the film. Here, spin coating method is applied to make several thin and smooth films on the 0.190 mm BK7 cover glasses,

and the thickness of those films are supposed to be 80 nm, 100nm, 190nm, 200nm, 280nm, and 500nm based on the PMMA spin coating diagram. Those films are also measured by profilometer (Dektek 8) and compared the results with the CRDS results. In the experiments, each glass cover is presented in the CRDS cell at 59 degree incident angle and 650nm-670nm laser radiation is used as the light source. Under these conditions, we used the glass substrate as a control blank data and get the experimental data for different thickness of films. By interoperating the data with modeling the thickness of the films is calculated. Neglecting the interception and amplitude difference between model and data, by overlapping the data with model to match their phase and period, the film thickness  $d_2$  can be obtained.

Table 9-2 lists the comparison of the results getting by reading from PMMA diagram, CRDS and profilometer. It shows that the difference between these two methods are only below 20 nm and both of them are closed to the theoretical thickness from spin coating, which supports that the method by CRDS is reasonably accurate.

Table 9- 2 Comparison of the film thickness (nm) getting by CRDS and Profilemeter

No.	Thickness reading from PMMA diagram /nm	Thickness calculated from CRDS/nm	Thickness data from Dektek 8 Profilemeter/nm
1	80	80	92
2	100	130	125
3	190	200	188.
4	200	200	189
5	280	280	298
6	500	540	522

## 9.5 Conclusion

In this paper, we presented a new technique for measuring the thickness of transparent thin films using cavity – ring down spectroscopy. This technique is not only capable of accurate probing thickness but also good for real time measurement. With the model we developed, the method has high sensitivity. At present this measurement technique provides 10 nanometer limit detection which is better than most of other technique. The experimental results for PMMA thin film demonstrated

that the thickness can be measured within ~ 4% to 10% error range. Since CRDS is an optical method, it is not destructive and the index of refractory could be reasonably measured with assistance of other techniques. Overall, it is a promising and convenient method. It could be used in nano film or protein film growing real time quality control and also could become an alternate method of SPR.

**Reference:**

1. Ward In, E.R.P.a.W.T.W., *Adam Hilger Series on Optics and Optoelectronics*. Adam Hilger New York, 1988.
2. Casset, J., *Optical constants of absorbing materials by transmission interferometry on medium-thickness films*. J. Opt. Soc. Am., 1979. **69**(5): p. 725-730.
3. Joensen, P., et al., *Transmission method for determining the optical constants of metals*. J. Opt. Soc. Am., 1973. **63**(12): p. 1556-1562.
4. Burge, D.K. and H.E. Bennett, *Effect of a Thin Surface Film on the Ellipsometric Determination of Optical Constants*. J. Opt. Soc. Am., 1964. **54**(12): p. 1428-1433.
5. Bennett, J.M., *Precise Method for Measuring the Absolute Phase Change on Reflection*. J. Opt. Soc. Am., 1964. **54**(5): p. 612-622.

6. Shaalan, M.S. and S. Muawad, *The optimisation of the phase thickness in the determination of the optical constants of thin dielectric and slightly absorbing films.* Journal of Physics D: Applied Physics, 1983. **16**(3): p. 419.
7. Burke, J., et al., *Simultaneous measurement of several near-parallel surfaces with wavelength-shifting interferometry and a tunable phase-shifting method.* Optics and Lasers in Engineering, 2007. **45**(2): p. 326-341.
8. Bruning, J.H., et al., *Digital Wavefront Measuring Interferometer for Testing Optical Surfaces and Lenses.* Appl. Opt., 1974. **13**(11): p. 2693-2703.
9. Schwider, J., et al., *Digital wave-front measuring interferometry: some systematic error sources.* Appl. Opt., 1983. **22**(21): p. 3421-3432.
10. Kim, S.Y., *Simultaneous determination of refractive index, extinction coefficient, and void distribution of titanium dioxide thin film by optical methods.* Appl. Opt., 1996. **35**(34): p. 6703-6707.
11. Kim, S.Y., *Determination of the complex refractive index and thickness of MNA/PMMA thin film.* Journal of the Optical Society of Korea, 1996. **7**(357-362).
12. C. Caliendo, E.V., and G. Saggio, *An integrated optical method for measuring the thickness and refractive index of birefringent thin films.* Thin Solid Films, 1997. **292**: p. 255-259



13. Wang, H., *Determination of optical constants of absorbing crystalline thin films from reflectance and transmittance measurements with oblique incidence.* J. Opt. Soc. Am. A, 1994. **11**(8): p. 2331-2337.
14. Fukano, T. and I. Yamaguchi, *Separation of Measurement of the Refractive Index and the Geometrical Thickness by Use Of A Wavelength-Scanning Interferometer with A Confocal Microscope.* Appl. Opt., 1999. **38**(19): p. 4065-4073.
15. Bader, G., et al., *Reflection transmission photoellipsometry: theory and experiments.* Appl. Opt., 1995. **34**(10): p. 1684-1691.
16. Rusli and G.A.J. Amaratunga, *Determination of the optical constants and thickness of thin films on slightly absorbing substrates.* Appl. Opt., 1995. **34**(34): p. 7914-7924.
17. Dobrowolski, J.A., F.C. Ho, and A. Waldorf, *Determination of optical constants of thin film coating materials based on inverse synthesis.* Appl. Opt., 1983. **22**(20): p. 3191-3200.
18. Wang, Y. and M. Miyagi, *Simultaneous measurement of optical constants of dispersive material at visible and infrared wavelengths.* Appl. Opt., 1997. **36**(4): p. 877-884.

19. O'keefe, A. and D.A.G. Deacon, *Cavity ring-down optical spectrometer for absorption measurements using pulsed laser sources*. Review of Scientific Instruments, 1988. **59**(12): p. 2544-2551.
20. Scherer, J.J., et al., *Cavity ringdown laser absorption spectroscopy: History, development, and application to pulsed molecular beams*. Chemical Reviews, 1997. **97**(1): p. 25-51.
21. Wheeler, M.D., et al., *Cavity ring-down spectroscopy*. Journal of the Chemical Society-Faraday Transactions, 1998. **94**(3): p. 337-351.
22. Wang, L.M. and J.S. Zhang, *Detection of nitrous acid by cavity ring down spectroscopy*. Environmental Science & Technology, 2000. **34**(19): p. 4221-4227.
23. Yingdi Liu, R.M.-C., James Hargrove, David Medina and Jingsong Zhang, *Measurements of Peroxy Radicals Using Chemical Amplification-Cavity Ringdown Spectroscopy*. Environ. Sci. Technol, 2009. **43** (20): p. 7791–7796.
24. Halmer, D., et al., *Fast Exponential Fitting Algorithm for Real-time Instrumental Use*. Review of Scientific Instruments, 2004. **75**(6): p. 2187-2191.

# Chapter 10 Conclusion

Air pollution and global climate change are important environmental issues that affect our society. To understand these problems and to develop control strategies requires deeper understanding of atmospheric chemistry, which seeks to reveal the causes of these problems and to evaluate possible solutions and government policies.

This thesis mainly focuses on various aspects of atmospheric chemistry. With the applications of cavity ring-down spectroscopy (CRDS), atmospheric chemistry studies involving elementary chemical processes and reaction mechanisms ranging from atmospheric free radicals to aerosols have been carried out. Specifically, optical CRDS instrumentation is developed to measure and characterize the key species in tropospheric oxidation processes, i.e., peroxy radicals, as well as their photochemistry and reactions.

The peroxy radicals (hydroperoxy  $\text{HO}_2$  and organic peroxy  $\text{RO}_2$ ) play significant roles in the photochemistry of the troposphere. It is important and challenging to accurately measure the trace and reactive tropospheric peroxy radicals, especially in situ and in real time. To monitor the  $\text{HO}_2$  and  $\text{RO}_2$  radicals, two CRDS-based methods are developed. The first approach combines chemical amplification detection of peroxy radicals (PERCA) with CRDS. In this method,  $\text{HO}_2$  and  $\text{RO}_2$  are first converted to  $\text{NO}_2$  via reactions with  $\text{NO}$ , and the  $\text{OH}$  and  $\text{RO}$  co-products are

recycled back to HO<sub>2</sub> in subsequent reactions with CO and O<sub>2</sub>; these chain reactions are repeated and amplify the level of NO<sub>2</sub>, with an amplification factor of ~150. The amplified NO<sub>2</sub> is then monitored by CRDS. The peroxy radical detection sensitivity is shown to be ~10pptv/60s, fast and sufficiently sensitive for ambient detection. Ambient measurements of the peroxy radicals were carried out at Riverside in 2007.

To improve this successful method, a dual-inlet PERCA-CRDS system is developed. This instrument employs two identical inlet reactor-NO<sub>2</sub> detector combinations: one of which is operated in the background, while the other operates in the radical measurement mode. This instrument is improved over the single-channel version, as it continuously monitors the background and minimizes the effects of fluctuations in background NO<sub>2</sub> and O<sub>3</sub>. In addition, it improves the time response and allows detection of changes in peroxy radical concentrations that are related to the rapid changes in NO concentrations and O<sub>3</sub> photolysis frequency. Furthermore, a small blue diode laser is used as the light source. The instrument is portable for field measurements (including aircraft) and environmental chamber studies. With this improved instrument, higher detection sensitivity of 4ppt/10s is obtained. Ambient measurements of the peroxy radicals using dual – inlet PERCA – CRDS were carried out to demonstrate the improvement instrument.

This same dual – inlet PERCA – CRDS is also used for detecting the optical extinction of aerosol for laboratory study and ambient measurement. Accurate measurement of the optical extinction of atmospheric aerosol is important to estimate the direct climate effects of aerosols. Using this blue diode laser based dual-channel CRDS instrument, the background and background plus aerosol extinction signals is continuously detected. This approach is less sensitive to fluctuations of other interferences. Laboratory generated ammonia sulfate aerosols of different sizes ( $<1\ \mu\text{m}$  in diameter) are tested and characterized with this technique, and good agreements between the experiment results and the Mie theory calculation are obtained. Measurements of ambient aerosol are also carried out to demonstrate this technique

In addition, photoionization time-of-flight mass spectrometry is utilized to study reactive intermediates and reaction mechanism of the ozonolysis of alkene reactions. Ozone-alkene reactions are significant removal processes of alkenes in the troposphere and generation processes of secondary organic aerosol (SOA), and they are also important sources of OH radicals. To detect the early transient reactive intermediates and investigate the mechanisms of initial steps of ozonolysis of alkenes, these gas-phase reactions are carried out in a fast flow reactor under the conditions of low pressure (7-10 Torr) and room temperature. The alkenes

investigated include *cis*-2-butene, tetramethylethylene, cyclohexene, isoprene and  $\alpha$ - and  $\beta$ -pinenes. CO is used as an OH scavenger to minimize the reactions between the OH byproduct and alkenes. After a short reaction time of  $\sim$ 25 ms, the initial products, both free radical intermediates and stable species, are sampled into a supersonic molecular beam and directly detected by 118-nm vacuum ultra-violet (VUV) photoionization time-of-flight mass spectrometry (TOFMS). Mass peaks corresponding to the Criegee intermediates or their isomers are identified. The alkene-ozone reactions with longer reaction time (up to 10 s) and 1 atm pressure are also carried out and studied. A general trend in the mass spectra and the reaction mechanisms is observed.

In addition to the studies of atmospheric chemistry, for developing new applications for CRDS technique, a novel method for transparent nanoscale thin film detection has been developed and demonstrated. This method aimed at determining the thickness of a non-absorbing thin film upon a nearly transparent substrate using CRDS. Through the analysis of the transmittance signal measured at various incident angles, the CRDS data have the information of the refractory index and the film thickness. A model was developed and demonstrated for a polymer thin film (PMMA). Thicknesses of a few tens of nanometers can be measured. This method is simple and capable of in situ study of transparent thin films.

Overall, in this thesis work, various environmental studies using CRDS instrument and VUV–TOFMS methods for important atmospheric species are characterized and new information of atmospheric chemistry is obtained from these projects, which can provide insightful data in atmospheric processes and lead to a better understanding of the atmospheric system, and eventually extend to environmental policy. Meanwhile, efforts have been made for developing new sensitive technique for not only gas phase studies but also surface and condense phase studies.